Molecular Modifications of Flexible Porous Substrates Through Depositions

A thesis submitted
in the partial fulfillment of the requirement
for the degree of
Doctor of Philosophy

by

Prerona Gogoi
(Roll No: 166107107)

Under the supervision of

Dr. Partho Sarathi Gooh Pattader
&
Prof. Arun Chattopadhyay

DEPARTMENT OF CHEMICAL ENGINEERING
INDIAN INSTITUTE OF TECHNOLOGY GUWAHATI
GUWAHATI-781039 (INDIA)
MARCH 2023

Declaration

I, **Prerona Gogoi**, hereby declare that the content embedded in this thesis is the outcome of the experiments and analysis carried out by me at the Department of Chemical Engineering, Center for Nanotechnology and Central Instrument Facility, Indian Institute of Technology Guwahati, Assam, India, under the supervision of **Dr. Partho Sarathi Gooh Pattader,** Associate Professor, Department of Chemical Engineering, Indian Institute of Technology Guwahati, India and **Prof. Arun Chattopadhyay,** Professor, Department of Chemistry, Indian Institute of Technology Guwahati, India. In keeping with the general practice of reporting scientific observations, due acknowledgment has been made where the work described is a contribution of another investigator.

Date: 09/03/2023

Place: IIT Guwahati

Prerona Gogoi
Roll No: 166107107
Department of Chemical Engineering
Indian Institute of Technology Guwahati
Guwahati-781039, Assam, India

CERTIFICATE

This is to certify that the work contained in this thesis entitled " **Molecular Modifications of Flexible Porous Substrates Through Depositions**" by **Prerona Gogoi**, has been carried out under our supervision and has not been submitted elsewhere for a degree.

Date:

Place: IIT Guwahati

Thesis Supervisor

Dr. Partho Sarathi Gooh Pattader
Associate Professor
Department of Chemical Engineering
Indian Institute of Technology Guwahati
Guwahati-781039, Assam, India

Thesis Co-Supervisor

Prof. Arun Chattopadhyay
Professor
Department of Chemistry
Indian Institute of Technology Guwahati
Guwahati-781039, Assam, India

Acknowledgments

Looking back to January 2017, when I joined as a research scholar here at IIT Guwahati, little did I know how this journey would turn up. After spending five and a half years, I can say with contentment that these years have helped me learn a lot in my research field and gave me an overall exposure to many other life skills that will help me further in my future. It is my pleasure to remind and offer my sincere gratitude to many people for their kind support and help throughout the completion of my thesis.

At the very onset, I would like to thank my thesis supervisors, Dr. Partho Sarathi Gooh Pattader and Prof. Arun Chattopadhyay, for accepting me into their research group for an exciting project. Partho Sir has always supervised every minute detail while I carried out my experiments and helped review the results obtained. Arun Sir has always motivated me with his wise, thoughtful, intelligent advice and hints in every section of the research work. With the vision and planning of both my guides, this work turned out to be quite fascinating than I could ever imagine.

I express my sincere gratitude to all the doctoral committee members, Prof. Siddhartha Sankar Ghosh, Professor from the Department of Biosciences and Bioengineering, Prof. Pallab Ghosh, Professor and Prof. Tapas K. Mandal, Professor from the Department of Chemical Engineering, for their valuable suggestions in improving my research work. I also thank Prof. Tamal Banerjee and Dr. Rajiv Kar for accepting to be part of my viva-voce examination committee and evaluating my performance.

I would also like to thank both my PhD thesis examiners Prof. Basavaraj Madivala Gurappa, Professor, Department of Chemical Engineering, Indian Institute of Technology Madras, India and Prof. Dr. Ganpati Ramanath, John Tod Horton Professor, Material Science and Engineering Department, Rensselaer Polytechnic Institute, Troy, NY for giving their valuable time to check my thesis and provide with important comments that helped in further improvement of the quality of the thesis.

I would like to thank Prof. Dipankar Bandopadhyay for being kind enough to provide us with all the research facilities in his laboratory during my initial days of research work when our new laboratory was under construction. I will also be always grateful to Prof. G. Pugazhenthi, Head of the Central Instrument Facility, and the entire team of FESEM, for arranging numerous slots in a short time and helping me submit my manuscript revision on time.

I also thank the Analytical Laboratory, Department of Chemical Engineering, for providing a range of instruments to carry out my characterizations. Also, I would like to thank the staff members and the Department of Chemical Engineering for helping me with all the official work and providing fully-furnished labs. Besides, I will always be grateful to the Centre for Nanotechnology for providing world-class cleanroom laboratories for the fabrication and characterization of samples.

My sincere gratitude and appreciation goes to all my PSDL research group members Dr. Pritam Roy, Dr. Ankur Pandey, Dr. Sunil Kumar Singh, Dr. Kaniska Murma, Aniruddha Deb, Gobinda Chetry, Khalid Jamal Ansari, Krishna Pradeep, Himanshu Raturi, Aishwarya Srinivasan, Tesfey Gebrimikael Teklehaimanot, Rupam Kumari, Tejas Rai and Aritra Mukherjee.

I want to thank individually Mrigankajit Dutta, Dr. Awadh Kumar Kishor, Dr. Rupam Sinha, Dr. Nirmal Roy, Dr. Surjendu Maity, Deepak Kumar Misra for all the help I took at some point or the other in my PhD journey.

Without my seniors and friends, Dr. Dharmalingan K, Dr. Gaurangi Gogoi, Dr. Nimisha Bania, Dr. Joy Prakash Das, Pankaj Boruah, Alice Boruah, Monalisha Sarma, Rimjhim Moral and Bibari Boro my stay in IITG would not have been memorable.

Lastly, I will be eternally grateful to my parents, Swarnali Borgohain and Juga Jiban Gogoi, and my younger brother Bhabartha Prakash Gogoi for their encouragement and inspiration throughout this journey.

PRERONA GOGOI

To the countless creativity in science

and

letting me perceive a handful of its essence

Bhagavad Gita: Chapter 5, Verse 10

ब्रह्मण्याधाय कर्माणि सङ्गं त्यक्त्वा करोति यः |
लिप्यते न स पापेन पद्मपत्रमिवाम्भसा ||10||

brahmaṇyādhāya karmāṇi saṅgaṁ tyaktvā karoti yaḥ

lipyate na sa pāpena padma-patram ivāmbhasā

Translation: Those who dedicate their actions to God, abandoning all attachment, remain untouched by sin, just as a lotus leaf is untouched by water.

SYNOPSIS

Molecular Modifications of Flexible Porous Substrates Through Depositions

1. Introduction

The maneuver of engineering is a wonder, as it aims to generate extensive technology in the form of products and services by implementing scientific knowledge. The extensive development in the field of micro-nano technology is supremely worthy of note. Although modern micro-nano technology is relatively new, nanoscale materials have been used for centuries. Adding gold chloride and silver nitrate nanoparticles created red and yellow colored glass windows which were seen in medieval churches hundreds of years ago.[1] Nanotechnology is the science, engineering, and technology conducted at the nanoscale, which is about 1 to 100 nm.[2] Thus, nanotechnology assisted in miniaturizing science and technology to analyze, fabricate and characterize products with micron to nanoscale feature sizes.[3,4] Some captivating successes in this field are manufacturing miniaturized electronic chips on a silicon substrate,[5] MEMS-accelerometers[6] for automobile airbags, micro-diaphragms for pressure sensors,[7] micromirrors for fibre optics,[8] etc. to name a few.

Based on the science, engineering, and technology alongside nanotechnology, numerous structures or patterns can be developed on any substrate by the method of the Coffee Stain Effect. The coffee stain effect got its name based on the phenomenon where drying spilled a coffee drop or a raindrop on a windowpane leaves a dense, ring-like deposit along the perimeter of the droplet on a solid surface.[9] Thus, numerous parameters like the type of substrate (hydrophilic and hydrophobic), solute (hydrophilic and hydrophobic) and solvent (polar and non-polar) and the various combinational interactions amongst the solute, solvent and substrate can give us the desired pattern after evaporation of the droplet. These micropatterns thus created by this technique are mainly utilized in printing miniaturized material used in electronics and

electrical industry, chemical, mechanical industries, etc. They find potential applications in medicine, low cost technology for disease diagnostics,[10,11] inkjet printing for conventional printing,[12,13] or high throughput sensing node for different types of sensors,[14] patterning technique,[14,15] paint technology, [16] etc.

There are various techniques involved in molecular modification of substrate, broadly classified as chemical deposition and physical vapour deposition which are discussed in details in **Chapter 1**. Chemical deposition processes include plating, spin coating, dip coating, atomic layer deposition, etc. Whereas physical vapor deposition processes are sputtering, thermal evaporation, etc.

Dip coating any substrate into a solution of Octadecyltrichlorosilane (OTS) and toluene can form a self-assembled monolayer[17] on the substrate, and thus the substrate becomes hydrophobic.[18] Following a similar technique, any hydrophilic flexible fabric can be made hydrophobic by coating a nanometer-thick layer of OTS which can be used to make a breathable mask. Due to its hydrophobicity, it can repel the incoming virus-laden droplets, as in the case of COVID-19. Similarly, the fabrication of hydrophobic bandages with nanometer thick coating of OTS will prevent the wounds from getting wet, thus speeding up the wound healing process. Furthermore, both the OTS-coated fabric and the pristine fabric used in making a mask will show different sieving efficiency due to the vibration caused by talking, breathing, sneezing, etc. So illustrating how the droplets containing pollutants or viruses behave on the outer surface of the mask when we are wearing it is also an interesting study.

Considering the above context, the present thesis explores the usage of nanotechnology in creating micro-nano structures on any substrate either by evaporation of colloidal droplets or by modifying various kinds of substrate by depositing nanometer thick coating. These modified surfaces have efficient usage in blocking water droplets or particle-laden droplets that can be a boon in electronics, biomedical, fabric manufacturing, etc. Hence, the objectives of this thesis are as follows,

- Towards Controlling Evaporative Deposition: Effects of Substrate, Solvent, and Solute
- Nanometer Thick Extremely Hydrophobic Coating Renders Cloth Mask Potentially Effective Against Aerosol-driven Infections
- Chemically Coated Robust Reusable Highly Hydrophobic Bandages
- Microparticle Penetration through a Vibrating Porous Substrate

The detailed objective, procedures, and experimental findings of the four topics mentioned above are further elaborated in this thesis, along with the future scopes.

2. Towards Controlling Evaporative Deposition: Effects of Substrate, Solvent and Solute

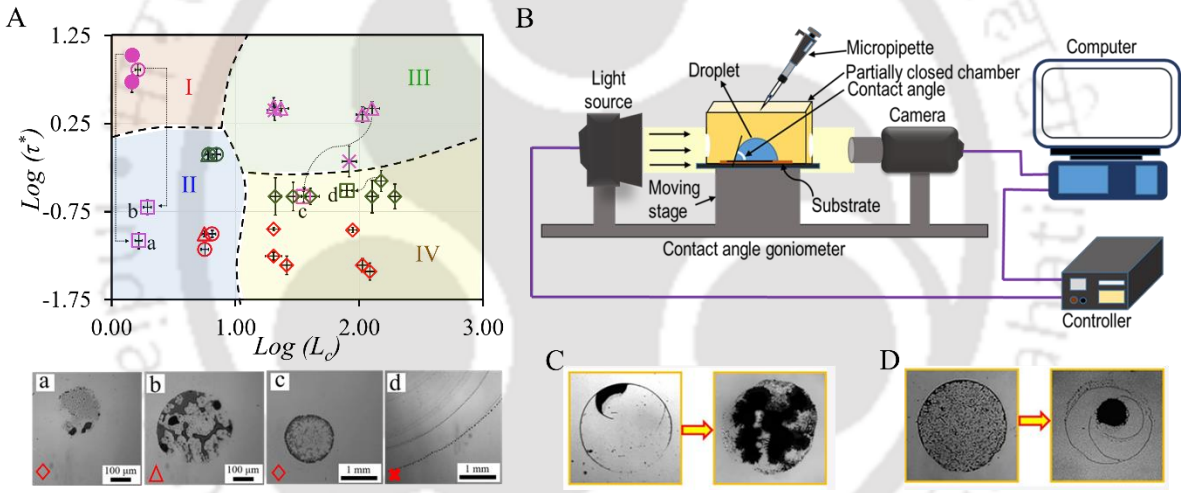

Figure 1. (A) Top panel shows the deposition zone diagram in terms of the dimensionless deposition time τ^* and characteristic length scale L_c. The symbol colors pink, green and red depict water, toluene and chloroform respectively. Filled circle (●) depicts uniform disk, open circle (○) indicates prominent coffee ring, open triangle (Δ) and cross (×) represent irregular and faint coffee rings, respectively, and open diamond (◊) depicts irregular disk-like deposition from 2 µL droplets. Zone-I depicts uniform disk and coffee ring deposition, in Zone-II the patterns becomes irregular, Zone-III is for irregular coffee ring and faint coffee ring and Zone-IV indicates irregular disk-like deposition. The square (□) symbols (a,b,c,d) in the top panel indicate depositions from droplets other than 2 µL volume. Corresponding optical micrographs (a,b,c,d) for square symbols are shown in the bottom panel, (B) Schematic of the experimental setup, (C) Effects of contact line pinning and (D) Controlling droplet pattern by regulating the droplet ambiance.

Drying of a spilled coffee drop leaves a dense, ring-like deposit along the perimeter on a solid surface.[9,19] During evaporation from the droplet, the contact line gets pinned, and the

liquid evaporating from the periphery is replenished by the liquid from the interior by capillary flow.[9,16] Thus, the coffee stain effect is an interesting phenomenon that can generate various patterns on different chemically modified smooth surfaces based on the interactions among the solute, solvent and substrate. The main objective of **Chapter 2** is to demonstrate the formation of different distinct patterns on these chemically modified smooth surfaces, such as coffee ring, multiple coffee ring, uniform disk-like deposition, faint coffee rings, etc., and also qualitatively explain the deposition mechanism for the formation of different patterns. The evaporation process of a sessile droplet on different types of Si wafer (substrate) was performed under normal diffusion conditions by enclosing a 2 μL droplet in a partially enclosed chamber of approximately 2.5 cm x 2.5 cm x 2.5 cm which is opened at the top. To substantiate a deposition zone diagram with basically four zones was plotted which maps the deposition patterns based on the deposition time scale and a characteristic geometric length scale that accounts for the "space" available for the distribution of solute particles on the substrate. Novelty here was in identifying a specific zone where the solute-solvent-substrate interactions play a crucial role and other deposition zones where it is governed solely by the geometry of the droplets or by the solvent-substrate interaction. Moreover, these experiments will give a better insight into the phenomenon occurring inside a microdroplet when it undergoes evaporation in a particular appointed condition. After performing experiments on silicone oil coated Polydimethylsiloxane (PDMS) slippery surfaces we concluded that slippery surfaces inhibit the contact line pinning leading to aggregation of the particles forming disk-like deposition. Finally, by using lower boiling point solvents the surrounding environment of the droplet was regulated, which further regulated the Marangoni flow at the surface. This phenomenon changed the internal inertial flow field of the particles inside the droplet, thus manipulating the deposition pattern. This study is expected to be useful for fundamental scientific research and industrial applications that require specific micro-nano deposition patterns of particles from colloids or suspensions.

3. Nanometer Thick Extremely Hydrophobic Coating Renders Cloth Mask Potentially Effective Against Aerosol-driven Infections

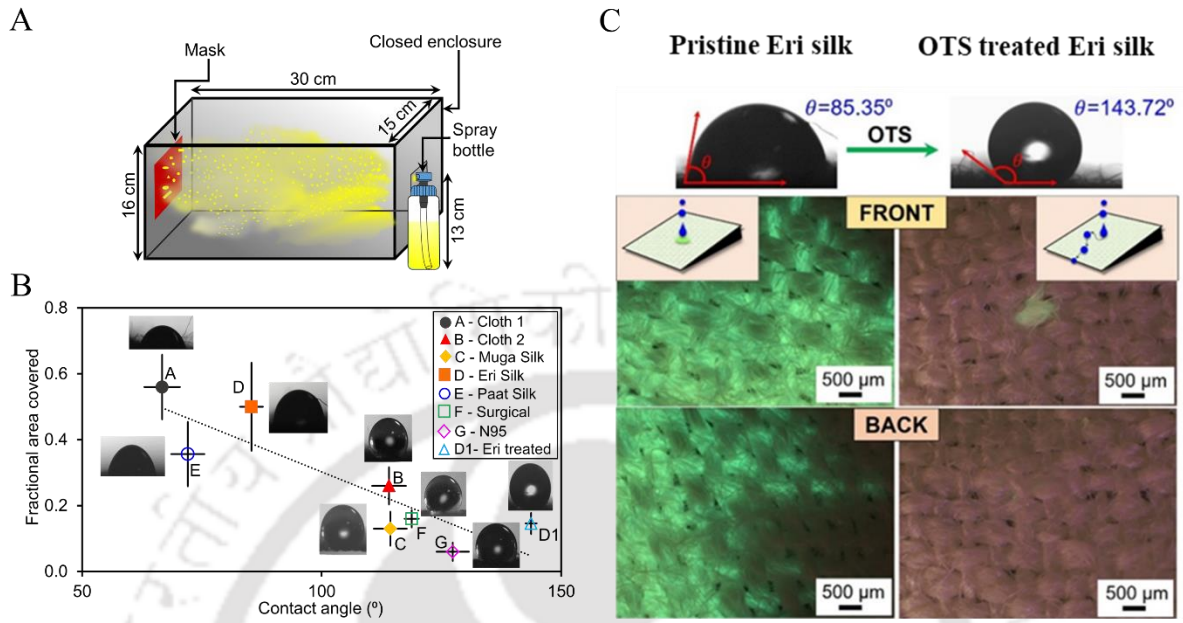

Figure 2. (A)Schematic showing the experimental setup of a cuboidal enclosure of length ~30 cm that had a mask on one end and an opening for spraying from the other end, (B) Graph depicting the fractional area coverage of the absorbed dye after drying of the deposited droplets as a function of the contact angle of water on the mask materials. The black dotted line is the linearly-fitted curve. The inset shows the figures of the droplet placed on the mask fabric and (C) The characteristic difference between the pristine Eri silk and OTS-treated Eri silk.

Recently the world faced a grievous pandemic i.e., Coronavirus Disease-2019 (COVID-19), which has not yet ended completely. As a result, wearing a mask is still necessary for every individual to curb the spread of the disease and prevent a healthy person from being infected. Different types of mask were launched during the pandemic, such as N95, KN95, surgical masks, cloth masks, etc. The N95 mask with an efficiency of 95% or more to block 0.3 μm particles[20] and surgical masks with a filtration efficiency of >80% with respect to 50-500 nm particles[21] are considered better protectors against the aerosol-driven virus. Although the N95 is the best mask available in the market, but due to its multi-layered sealed design, it is difficult for any person to wear it for a longer duration of time as breathing becomes uncomfortable. Amongst all the masks available in the market, the cloth masks are highly breathable but can easily absorb the virus-laden droplets increasing the plausible risk of getting infected.[22] Hence, the question remains whether

the chemical modification of these hydrophilic cotton or silk masks to hydrophobic masks would retain the comfortability of breathing and, at the same time, provide better protection against viral infection. In **chapter 3**, our first finding says that the efficiency of a mask predominantly depends on the surface properties of the fabric used in making a mask. Hence, we modified the locally available hydrophilic Eri silk fabric into hydrophobic Eri silk fabric by depositing a nanometer thick coating of OTS (octadecyltrichlorosilane) without compromising the breathability of the mask. The modified hydrophobic Eri silk showed an excellent hydrophobic property with contact angle of water 143.7^{0} which could repel back the incoming droplets without wetting the fabric and also allowed the easy flow of air through the three-layered treated Eri silk mask (breathability reduced by only 22% with respect to the pristine Eri silk). Hence, this makes the modified silk mask a better alternative to the N95 mask and can be made easily available to the common masses.

4. Chemically Coated Robust Reusable Highly Hydrophobic Bandages

With more than 3000 different types of bandages available in the market for wound care, people can choose from a wide range of collections according to the suitability for a specific type of wound. However, the conventionally available bandages such as 12-ply gauze, crepe bandage, cotton, and bandaids are generally hydrophilic in nature. So any exposure to water makes it wet and thus requires frequent and repeated wound dressing for faster healing of the wounds. It is also noticed that the patients have to go through a lot of pain to remove the bandage during wound dressing as it gets stuck to the wound with contamination. Generally, in common households, it is seen that people cover their bandages with plastic sheets while bathing or doing any work that requires exposure to water. The most interesting concept we see nowadays is that the market gives us options to buy custom-made plastic bags to cover the bandaged parts. In **Chapter 4**, our objective was to demonstrate a process to modify the conventionally available non-occlusive bandages that will repel the incoming water and keep the wounds dry for faster

healing. Various types of hydrophilic bandages are chemically treated with Octadecyltricholorosilane (OTS), which contributes to the hydrophobic nature of the bandage. These modified bandages showed a water contact angle greater than 130°, making them extremely hydrophobic, whereas for the as-purchased bandages, water gets immediately absorbed by the surface. Moreover, these treated bandages do not stick to the wounds nor get wet in moist conditions. Although the bandages are chemically treated, they are safe to be used on human skin. Sometimes the commercially available bandaids appear to be hydrophobic but the hydrophobic property deteriorates after three washings, but OTS treated bandaid retain their hydrophobicity upto around eight washings. The serous liquid produced by the wound in the normal healing process would remain intact on the wound bed due to the hydrophobic environment rather than being absorbed by the bandage, which will make the wound healing process much faster.

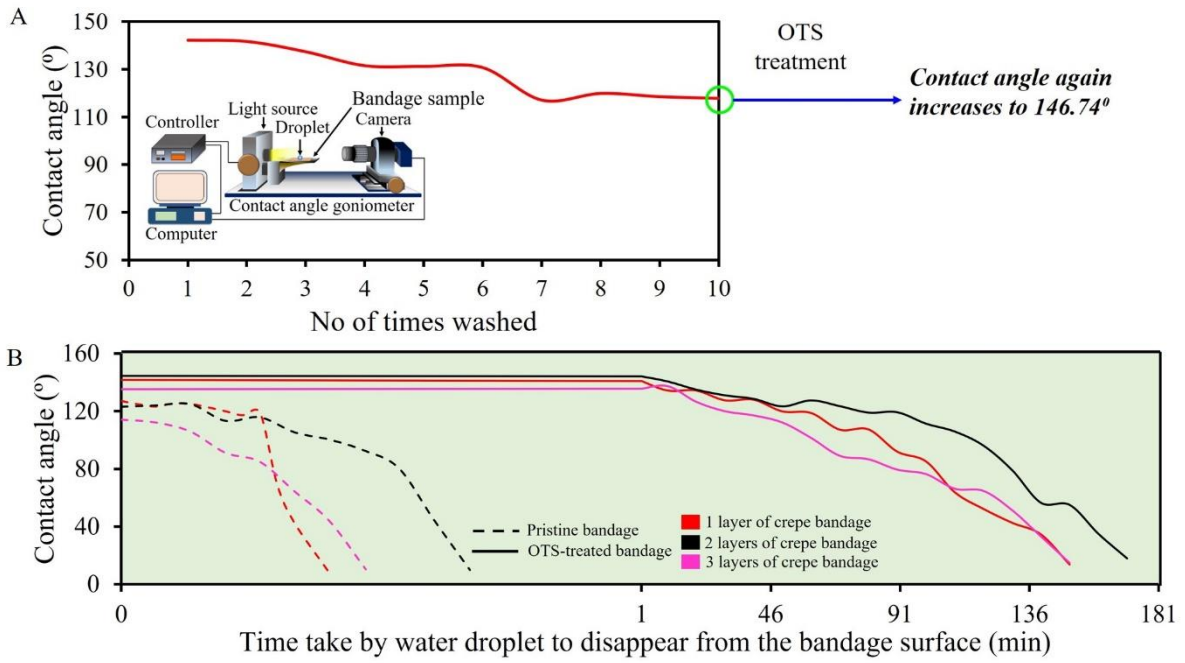

Figure 3. (A) The graph shows the decrease in contact angle of the treated crepe bandage after each washing. The inset shows the experimental setup where a droplet is placed on the bandage sample and investigated with the help of the contact angle goniometer, and (B) The graph shows the change in contact angle wrt to time of a 5 μL droplet placed on both pristine and OTS-treated crepe bandage.

5. Microparticle Penetration through a Vibrating Porous Flexible Substrate

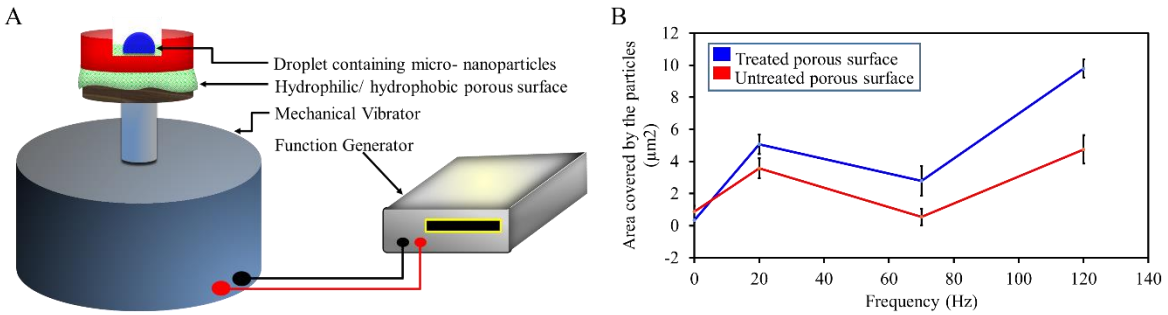

Figure 4. (A) The experimental setup showing how a droplet is placed on top of the flexible porous fabric attached to a stage above the mechanical vibrator and (B) The graph showing the area covered by the particles present in the droplet after being percolated through the porous substrate and deposited on the glass substrate present at the bottom of the stage.

When a droplet containing pollutants or disease-causing microorganisms sits on the mask fabric, these micro-nano particles will either be repelled off or penetrate through the fabric. This depends entirely on the nature of the fabric material and the vibration the fabric is experiencing due to talking, breathing, or sneezing. Keeping in mind the above perspectives, we studied the percolation of a droplet containing varied-sized micro-nano particles through a vibrating porous flexible fabric. A circular stage was fabricated where a porous flexible substrate was fixed. We performed the experiments using both as-purchased Eri silk and OTS-treated Eri silk which acted as the porous flexible surface for the experiment. This stage was placed above the mechanical vibrator, which can vibrate based on the frequency and amplitude given to the function generator. A 4 μL droplet was placed above the porous surface while performing the experiments. The droplet contained lab synthesized silica particles (20-30 nm) and as-purchased UV Flourescent microsphere (10-20 μm) in it. After complete evaporation of the droplet, both the porous surface and the glass substrate present at the bottom of the stage were seen either under the optical microscope or FESEM. In **Chapter 5**, we examined how most of the micro-nano particles present inside the droplet percolate through the porous surface, while some are repelled off, and some get absorbed by the fabric due to capillary action. In the case of hydrophilic fabric, most particles are absorbed by the fabric which would be a potential threat to

the person as these particles will slowly percolate inside to the inner side of the mask, thus getting infected. Whereas in a hydrophobic fabric, we see that most particles repelled off, while some deposited on the fabric surface and a few percolated through the fabric.

6. Conclusion and future scope

Chapter 6 gives a detailed conclusion from each chapter. This chapter also mentions various other future scopes related to the work done in this thesis. After a thorough review of the previous literature works done by many researchers, we could apprehend that systematic and lucid studies relating to the type of substrate, solvent, and solute particles; and the potential parameters needed for the phenomenon of coffee stain effect to be effective are yet to be studied. By virtue of coffee stain effect and following the technique of 3D printing, fabrication of various micronized industrial, electronics and biomedical 3D structures can be made possible. The coffee ring effect phenomenon could be used as an analytical tool to detect many vector-borne and microbial diseases at a lower cost. So finding some simple and economical materials and methods to manifest this technique would be a wonder to the medical community.

References

[1] A. V Zayats, *Nature* **2013**, *495*, S7.

[2] M. Rangasamy, *J. Appl. Pharm. Sci.* **2011**, *1*, 8–16.

[3] A. M. Dimiev, J. M. Tour, *ACS Nano* **2014**, *8*, 3060–3068.

[4] R. Rao, C. L. Pint, A. E. Islam, R. S. Weatherup, S. Hofmann, E. R. Meshot, F. Wu, C. Zhou, N. Dee, P. B. Amama, J. Carpena-Nuñez, W. Shi, D. L. Plata, E. S. Penev, B. I. Yakobson, P. B. Balbuena, C. Bichara, D. N. Futaba, S. Noda, H. Shin, K. S. Kim, B. Simard, F. Mirri, M. Pasquali, F. Fornasiero, E. I. Kauppinen, M. Arnold, B. A. Cola, P. Nikolaev, S. Arepalli, H.-M. Cheng, D. N. Zakharov, E. A. Stach, J. Zhang, F. Wei, M. Terrones, D. B. Geohegan, B. Maruyama, S. Maruyama, Y. Li, W. W. Adams, A. J. Hart, *ACS Nano* **2018**, *12*, 11756–11784.

[5] S. Gupta, W. T. Navaraj, L. Lorenzelli, R. Dahiya, *npj Flex. Electron.* **2018**, *2*, 8.

[6] P. Vinay, C. Satya, S. Vamsi, M. Hemanth, A. Saiteja, .abid Ali, P. Kumar, V. Satya, *Int. J. Mech. Eng. Technol.* **2017**, *8*, 424–434.

[7] S. Sugiyama, K. Shimaoka, O. Tabata, in *TRANSDUCERS '91 1991 Int. Conf. Solid-State Sensors Actuators. Dig. Tech. Pap.*, **1991**, pp. 188–191.

[8] M. Hu, H. Du, S. Ling, B. Liu, G. K. Lau, *Microsyst. Technol.* **2005**, *11*, 987–990.

[9] R. D. Deegan, O. Bakajin, T. F. Dupont, G. Huber, S. R. Nagel, T. A. Witten, *Nature* **1997**, *389*, 827–829.

[10] B. Sobac, D. Brutin, *Phys. Rev. E* **2011**, *84*, 011603.

[11] Y. Deng, X. Y. Zhu, T. Kienlen, A. Guo, *J. Am. Chem. Soc.* **2006**, *128*, 2768–2769.

[12] T. Breinlinger, T. Kraft, *Powder Technol.* **2014**, *256*, 279–284.

[13] J. Park, J. Moon, **2006**, *22*, 3506–3513.

[14] J. Wang, L. Wang, Y. Song, L. Jiang, *J. Mater. Chem. C* **2013**, *1*, 6048–6058.

[15] S. Magdassi, M. Grouchko, D. Toker, A. Kamyshny, I. Balberg, O. Millo, *Langmuir* **2005**, *21*, 10264–10267.

[16] R. D. Deegan, O. Bakajin, T. F. Dupont, G. Huber, S. R. Nagel, T. A. Witten, *Phys. Rev. E* **2000**, *62*, 756–765.

[17] E. Ruckenstein, Z. F. Li, *Adv. Colloid Interface Sci.* **2005**, *113*, 43–63.

[18] Y. Wang, M. Lieberman, *Langmuir* **2003**, *19*, 1159–1167.

[19] R. D. Deegan, *Phys. Rev. E* **2000**, *61*, 475–485.

[20] W. R. Dugdale CM, *JAMA Intern. Med.* **2020**, *180*, 1612–1613.

[21] Y. Yue, J. Wang, W. He, Y. Guo, H. Gao, J. Liu, *ACS Nano* **2020**, *14*, 13161–13171.

[22] S. Rengasamy, B. Eimer, R. E. Shaffer, *Ann. Occup. Hyg.* **2010**, *54*, 789–798.

Publications and Conferences

List of Journal Publications

From Thesis

1. **Gogoi, P.**; Chattopadhyay, A.; Pattader, P. S. G. Toward Controlling Evaporative Deposition: Effects of Substrate, Solvent, and Solute. *J. Phys. Chem. B* **2020**, 124, 11530–11539

2. **Gogoi, P.**; Singh, S. K.; Pandey, A.; Chattopadhyay, A.; Pattader, P. S. G. Nanometer-Thick Superhydrophobic Coating Renders Cloth Mask Potentially Effective against Aerosol-Driven Infections. *ACS Appl. Bio Mater.* **2021**, 4, 7921–7931

Outside thesis

1. Singh, S.K.; **Gogoi, P.**; Deb, A.; Pattader, P. S. G. Chiral Resolution of Racemic Amines in μ-Reactor-Crystallizer. *Chem. Eng. Sci.* **2022**, 256, 117686

2. Deb, A.; **Gogoi, P.**; Singh, S.K.; Pattader, P. S. G. Noise Activated DNA Translocation in Gel Electrophoresis for Faster Resolution. . *Langmuir* **2022**, 38, 11764-11769

List of Conferences

1. **Prerona Gogoi**, Arun Chattopadhyay, Partho Sarathi Gooh Pattader, The interesting phenomena of " Coffee Stain Effect", 5th National Workshop on NEMS/MEMS & Theranostic Devices, IIT Guwahati, 2019 -Poster presentation.

2. **Prerona Gogoi**, Arun Chattopadhyay, Partho Sarathi Gooh Pattader, The " Stick-Slip Motion" of the conatct line of a drying droplet, 1st National Conference on " Advances in Chemical Engineering", Assam Engineering College Guwahati, 2019- Oral presentation.

3. **Prerona Gogoi,** Arun Chattopadhyay, Partho Sarathi Gooh Pattader, The coffee stain effect, International Conference on Advances in Chemical Engineering, UPES Dehradun, 2020- Poster presentation.

4. **Prerona Gogoi,** Arun Chattopadhyay, Partho Sarathi Gooh Pattader, Chemically Modified Cloth Mask with Potential Efficiency Against COVID-19 Infections, 7th International Conference on Advanced Nanomaterials and Nanotechnology (ICANN2021), IIT Guwahati,

2021- Flash Talk.

5. **Prerona Gogoi,** Arun Chattopadhyay, Partho Sarathi Gooh Pattader, Chemically modified cloth mask with potential efficiency against COVID-19 infections, Research and Industrial conclave, IIT Guwahati, 2022- Poster presentation.

NOMENCLATURE

C_R	Nondimensional time scale
D	Diffusivity
D_F	Diameter of footprint
H	Height of the sessile droplet
f	Fractional area of solid and air under liquid on the substrate
F_{pin}	Pinning force per unit length of the contact line
I_{ls}	Interaction between solvent and the substrate
I_{pl}	Interaction between particle and liquid solvent
I_{ps}	Interaction between particle and the substrate
k	Extinction coefficient
k_B	Boltzmann constant
L_c	Nondimensional length scale
n	Refractive index
r	Radius of droplet
R_H	Hydrodynamic radius
rr	Roughness ratio
T	Absolute Temperature
t_d	Total time for complete deposition
t_D	Diffusion time scale
x	Distance between the spray nozzle and the laser sheet
X	Thickness of the liquid layer from the substrate

Greek letters

θ	Contact angle
θ_{Adv}	Advancing contact angle
θ_c	Contact angle (Cassie equation)
θ_{CA}	Static water contact angle
θ_{cb}	Contact angle (Cassie-Baxter equation)
θ_{Eq}	Equilibrium contact angle
θ_{Rec}	Receding contact angle
θ_w	Contact angle (Wenzel equation)

θ_y	Contact angle (Young's equation)
θ_i	Angle of incidence
γ_{lg}	Surface tension of the liquid
γ_{sg}	Surface free energy of the solid/substrate
γ_{sl}	Interfacial tension between solid and liquid
σ	Fractional surface area in contact
ζ	Zeta potential
τ^*	Dimensionless time scale
τ_{evap}	Evaporative time scale
$\tau_{particle}$	Time scale of meeting of two adjacent particles near the contact line
μ	Mobility of the particle obtained from Stokes equation
η	Viscosity
λ_c	Capillary length scale
Ψ	Reflective amplitude ratio angle of s and p polarization
ρ	Complex reflectance ratio

Swedish letter

Å	Angstrom

Basic Math

Δ	Phase difference of s and p polarization

Acronyms

ACF	Autocorrelation Functions
ALD	Atomic Layer Deposition
AOI	Angle of Incidence
ASTM	American Society for Testing and Materials
BCE	Before Common Era
CA	Contact Angle
CAH	Contact Angle hysteresis
CBD	Chemical Bath Deposition
CCD	Charged-Coupled Device

CL	Contact Line
CMOS	Complementary Metal-Oxide-Semiconductor
COVID-19	Coronavirus Disease-2019
CR	Coffee Ring
CSD	Chemical Solution Bath
D	Disk
Dex	Dextran
DI	Distilled Water
DLS	Dynamic Light Scattering
DMODCS	Dimethyloctadecylchlorosilane
EBL	Electron Beam Lithography
E:I	Exhale-to-Inhale
FEM	Finite Element Method
FESEM	Field Emission Scanning Electron Microscopy
fps	Frames Per Second
FTIR	Fourier Transform Infrared
FTO	Fluorine-doped Tin Oxide
HPUV	High-Power Ultrasonic Vibration
IR	Infrared Radiation
LPUV	Low-Power Ultrasonic Vibration
MHA	16-Mercaptohexadecanoic acid
MLD	Molecular Layer Deposition
Na	Sodium
OTS	Octodecyltrichlorosilane
PCL	Polycaprolactone
PDMS	Poly(dimethylsiloxane)
PEDOT: PSS	Poly(3,4-ethylenedioxythiophene): Poly(styrene sulfonic acid)
PEG	Poly(ethylene glycol)
PM	Particulate Matter
P(NIPAM-co-AAc)	Poly(N-isopropylacrylamide-co-acrylic acid)
PP	Polypropylene
PVC	Polyvinyl Chloride
P(VDF-TrFE)	Polyvinylidene Fluoride-Trifluoroethylene

RMSE	Root Mean Square Error
RGO	Reduced Graphene Oxide
ROI	Region of Interest
SAM	Self-Assembled Monolayer
SDS	Sodium Dodecyl Sulfate
Si	Silicon
SARS-CoV-2	Severe Acute Respiratory Syndrome Coronavirus - 2
SVASC	Substrate Vibration-Assisted Spray Coating
TENG	Triboelectric Nanogenerator
TEOS	Tetraethyl Orthosilicate
UV	Ultraviolet
Vpp	Peak-to-Peak Volatge
WC	Water Column
WCA	Water Contact Angle
WHO	World Health Organization

LIST OF FIGURES

Figure No.	Description	Page No.
1.1	Schematic representation of different wetting behavior of a droplet placed on a substrate: (a) Young's model, (b) Wenzel's model, (c) Cassie Baxter's model, and (d) Cassie's model.	3
1.2	The picture shows the Superhydrophobic property of a Lotus (*Nelumbo nucifera*) leaf and the inset shows the SEM images[35] of a lotus leaf with hierarchical roughness.	4
1.3	The figure shows the wetting behavior found in different objects in nature, such as: (a) Lotus leaf (Lotus effect, i.e., Special case of Cassie state), (b) Rose Petal (Petal effect, i.e., Cassie impregnating Wenzel state), (c) Butterfly wing (Cassie state), (d) Leg of strider (Coexistence of Wenzel-Cassie state) and (e) Gecko toe pad (Cassie Baxter state).	6
1.4	The techniques used to measure dynamic contact angle are (a), (b) Needle method and (c) Tilting method.	8
1.5	Illustration of various solution-based chemical deposition processes (a) Spin coating (b) Dip coating, and (c) Spray pyrolysis.	10
1.6	Various vapor-based chemical deposition processes (a) Chemical Vapor deposition (CVD) and (b) Combination of Atomic Layer Deposition (ALD) and Molecular Layer Deposition (MLD).	12
1.7	Schematic representation for physical vapor deposition (PVD) processes (a) Sputtering and (b) Thermal evaporation.	14
1.8	Schematic showing an ideal assemblage of Self Assembled Monolayer (SAM).	15
2.1	Schematic of the experimental set-up. Here, 2 µL droplets were dispensed by a micropipette on the chosen substrate fixed on a contact angle goniometer (HO-IAD-CAM-01B). The videos and images were captured using a 5MP CMOS camera and recorded on a PC for subsequent analysis.	32
2.2	(A) Optical images of the deposited patterns of Nile red after complete evaporation. Brown dotted line indicates initial footprint (B) Overview of time of deposition against contact angle for the liquid droplet containing Nile red. The dye concentration was 1 mg/mL for all the solutions. All scale bars represent 1mm.	34
2.3	(A) Optical images of the deposited patterns of fluorescein after complete	38

evaporation. Brown dotted line indicates initial footprint (B) Overview of time of deposition against contact angle for the fluorescein dye. The dye concentration was 1 mg/mL for all the solutions. All scale bars represent 1 mm.

2.4 Optical images of the typical coffee ring (a), disk-like (b) and irregular (c) deposition from the fluorescein dye (similar to figure 2.3A (c), 2.3A (i) and 2.3A (d)) and the corresponding FESEM images (a1), (b1) and (c1) respectively. a2, a3, b2, b3, c2 and c3 are the magnified FESEM images as indicated. 39

2.5 (A) Optical images of the deposited patterns of fluorescein Na salt formed after complete evaporation. Brown dotted line indicates initial footprint (B) Overview of time of deposition against contact angle for the fluorescein Na salt. The dye concentration was 1 mg/mL for all the solutions. All scale bars represent 1 mm. 40

2.6 Top panel shows deposition zone diagram in terms of the dimensionless deposition time τ^*and characteristic length scale L_c(see text). The symbol colors pink, green and red depict water, toluene and chloroform respectively. Filled circle (●) depicts uniform disk, open circle (○) indicates prominent coffee ring, open triangle (Δ) and cross (×) represent irregular and faint coffee rings, respectively, and open diamond (◊) depicts irregular disk-like deposition from 2 μL droplets. Zone-I depicts uniform disk and coffee ring deposition dictated by interactions among solute-solvent-substrate. Similar interactions are still valid in Zone-II but due to less deposition time, the pattern becomes irregular. Zone-III is for irregular coffee ring and faint coffee ring deposition due to low available space (high L_c). Zone-IV indicates irregular disk like deposition due to low available space (high L_c) and time (low τ^*). The square (□) symbols (a-d) in the top panel indicate depositions from droplets other than 2 μL volume. Corresponding optical micrographs (a-d) for square symbols are shown in the bottom panel (see text for details). 43

2.7 Optical images of the deposition from aqueous solution of hydrophilic dye, fluorescein Na salt, at a higher concentration (A) and at a lower 46

concentration (B) on silicone oil layer. (C) The optical image of sessile droplet, forming the wetting ridge on the silicone oil layer. (D) Schematic showing the sessile droplet on the substrate.

2.8 Optical images of final deposited patterns formed with hydrophilic iron oxide particles in water due to lower surface tension zone created at the (A) top and (B) the side. The substrate is OTS treated Si wafer, i.e., hydrophobic in nature. To create the low surface tension zone, mixture of methanol and diethyl ether in the ratio of 1:1 was used. The schematic shows the flow pattern inside the droplet. The yellow arrow indicates the position of the microtip containing solvent soaked cotton. Low density hydrophobic dye (Nile red) deposition from aqueous solution on OTS-treated surface with (C) and without (D) solvent vapour (methanol and diethyl ether in the ratio of 1:1) exposure are shown in the optical images. 48

3.1 Schematic showing the experimental setup of a cuboidal enclosure of length ~30 cm that had a mask on one end and an opening for spraying from the other end. 60

3.2 The figure shows the plusible chemical reaction undergoing during modification of hydrophilic to hydrophobic Eri Silk fabric using octadecyltrichlorosilane (OTS). 61

3.3 FTIR-ATR spectra of as-purchased and treated Eri silk fabrics. 63

3.4 FESEM-EDS graphs showing distribution of different elements for, A: as-purchased Eri silk, B: OTS treated Eri silk. Inset shows the elemental mapping and the atomic % and weight % of different elements present on the fabric. 63

3.5 Fractional area covered on masks. (a) Graph depicting the fractional area coverage of the absorbed dye after drying of the deposited droplets as a function of the contact angle of water on the mask materials. The black dotted line is the linearly-fitted curve. Insets close to each point show the optical images of the water droplet on the mask surface (b) Typical fluorescence micrograph of the mask sample after spraying of two puffs from a spray bottle kept at 30 cm away in an enclosure shown in the experimental setup, A: Cloth 1, B: Cloth 2, C: Muga Silk, D: Eri Silk, E: Paat Silk, F: Surgical, G: N95, D1: Treated Eri silk. (c) Graph showing the 66

fractional area covered for different types of masks at different distances ranging from 0.3m to 1.8m. Inset shows the experimental set-up of a long cylindrical closed space of length 1.8 m with a diameter of 0.1 m. and (d) Comparative graphs showing the sharp decline in fractional area coverage at distances 0.3 m and 1.8 m, respectively. Corresponding data are provided in Table 3.4.

3.6 The figure on the left shows the contact angle made by water on as-purchased cotton cloth 1 fabric (Sample A) which is 66.7°. After OTS treatment the fabric turned hydrophobic (right) having contact angle made by water as 140.4°. 67

3.7 (a) Experimental set-up showing the method used for measuring the droplet size spread after spraying from a bottle. A laser sheet is used to illuminate the droplets and the image was recorded with a high-speed camera (Phantom VEO 640L) at 300 fps. Here, "x" is the distance between the spray nozzle and the laser sheet. The values of x were 5, 10, and 15 cm. (b) Transmission optical micrograph of the pore sizes of the first layer of the mask materials: the sample names indicated in the images correspond to those mentioned in Table 3.1. Corresponding FESEM images are provided in Figure 3.7. (c) Graph showing the pore size distribution of all types of masks. The black dotted line is the droplet size distribution plot for the value of x = 10 cm. Similar data with droplet size distribution for the value of x = 5 cm and 15 cm are presented in the Appendix A.3.1. 70

3.8 FESEM images showing the pores of mask surface. A: Cloth 1, B: Cloth 2, C: Muga Silk, D: Eri Silk, E: Paat Silk, F: Surgical Mask, G: N95, D1: Treated Eri silk. The scale bars (shown on right side of the images) for all the images represent 100 μm. The scale bar of the inset images (shown on left side of the images) represent 10 μm. F1 and G1 shows the zoomed in images for the fibres. F2 and G2 shows the zoomed in images for the solid patches present in between the fibres. 71

3.9 Droplet behavior on treated and untreated Eri silk mask. (a) The behavior of a 10 μL droplet when it was dropped on a slanted silk surface from a height of 33 cm (high impact). The angle of the slope was 15^{0} to the horizontal axis. The inset shows the experimental setup for the same. The plot shows the droplet apex height trail with time on as-purchased (blue 73

line) and OTS-treated (pink line) Eri silk fabric surfaces, respectively. (b) Results from the experiment similar to that in (a), but the droplet fell from a relatively shorter height of 5 cm (low impact) on as-purchased (blue line) and OTS-treated (pink line) Eri silk fabric surfaces, respectively. The inset graph shows the behavior when the droplet had transformed from Cassie-impregnated Wenzel state to Wenzel state on the as-purchased Eri silk fabric surface (see text for details). (c) Experimental setup to capture the droplets bouncing back from vertically placed treated (top) and as-purchased (bottom) Eri silk upon spraying from 5 cm distance. The droplets bouncing back from treated Eri silk initially traveled faster in a straighter path, whereas the as-purchased Eri silk followed a curved downward path due to the lower velocity experienced by the droplets. (d) Plot showing the trajectories of typical droplets bouncing back from the vertically placed as-purchased (blue) and OTS-treated (pink) Eri silk fabric as shown in (c) after hitting the surface. (e) Optical and fluorescence microscopic images of both as-purchased and OTS-treated Eri silk cloth pieces (front surface and back surface) after spraying with the liquid dye as depicted in (c).

3.10 (a) Fluorescence images showing the front side of the fabric where a trace of dye was left behind after complete evaporation of the droplet, due to high impact of the falling droplet on treated Eri silk fabric, (b) The clean back side of the same fabric verifies that the droplet was not soaked by the fabric. 75

3.11 The breathability of N95, as-purchased and treated Eri silk masks. Graphs showing the gas chromatography (GC) peak of oxygen after passing through the three layers of mask materials: for a) As-purchased Eri silk, b) OTS-treated Eri silk, and c) N95 mask fabrics. Dashed and solid lines show the oxygen peaks immediately after the opening of the oxygen-containing balloon and after 2 min of opening, respectively. The time on the x-axis is the residence time for the detection of oxygen by the GC machine. d) Experimental setup showing how oxygen was collected from a cylindrical enclosure for gas chromatographic detection. e) Table shows the area under the curve for the plots in (a-c) depicting the permeability (breathability) of oxygen through the three-layered masks and percentage reduction of the 76

breathability with respect to the as-purchased Eri silk mask fabric.

3.12 (a) Schematic showing the arrangement of placing two masks in proximity. (b) Cumulative fractional area covered on the same mask placed 1 cm apart from another mask of the same type for each spray count (1-10) while checking the penetration and soaking capacity of the mask. (c) Fluorescence microscopic images of the mask, which was placed 1 cm apart from another mask of the same type for the 10th spray while checking the penetration and soaking capacity of the mask. A: Cloth 1, B: Cloth 2, C: Muga Silk, D: Eri Silk, E: Paat Silk, F: Surgical Mask, G: N95. 77

4.1 The experimental setup shows the bandage with a water droplet placed on it, on the goniometer stage. 90

4.2 Graph showing the hydrophilic nature of different bandages used in the experiment. The graphs for cotton and 12 ply gauge bandages cannot be shown as the water gets immediately absorbed by them. 92

4.3 Graph showing the hydrophilic nature of different bandages after washing with water followed by drying. The graphs for cotton and 12 ply gauge bandages cannot be shown as the water gets immediately absorbed by them. 93

4.4 Graph showing the hydrophilic nature of different bandages after washing with detergent followed by drying. The graphs for cotton and 12 ply gauge bandages cannot be shown as the water gets immediately absorbed by them. 93

4.5 Graph showing the behavior of conventional bandages after OTS treatment. 94

4.6 Graph showing the behavior of modified bandages (OTS-treated) after washing with water followed by drying. 94

4.7 Graph showing the behavior of modified bandages (OTS-treated) after washing with detergent followed by drying. 95

4.8 The behavior of both untreated and treated bandaid after rubbing the bandaid surface with a finger in a circular motion with water. 95

4.9 The graph shows the decreased contact angle of the treated crepe bandage after each washing. 96

5.1 Experimental setup showing the placement of flexible porous surface to a function generator operated mechanical vibrator. The black arrow depicts the vibration direction of the stage. 107

5.2 FESEM image of the lab synthesized silica particles at the (a) Periphery and 107

(b) Centre of the deposition (c) Optical image of the as-purchased UV fluorescent particles.

5.3 DLS graph showing the realtime diameter (nm) of lab synthesized silica particles at different accumulation time. 109

5.4 The sinusoidal waveform for 70 Hz and 10 Vpp. The high-speed video was taken at 1000 fps and 1024x768 resolution. Here 70 Hz means 70 vibrations were produced in 1 second. 110

5.5 The graphs show the area (μm^2) covered by the lab synthesized silica particles (10-20 nm in diameter) on the glass substrate vs. frequency (Hz) for four different frequencies, namely, 0 Hz, 20 Hz, 70 Hz, and 120 Hz, all at 10 Vpp. The blue line represents OTS-treated Eri silk flexible porous fabric, and the red line indicates as-purchased Eri silk flexible porous fabric. 111

5.6 FESEM images of particles on glass substrates in case of lab synthesized silica particles (10-20 nm in diameter). The first row depicts the images for as-purchased Eri silk flexible porous fabric and the second row shows the images for OTS-treated Eri silk flexible porous fabric for frequencies: (a), (e) 0 Hz and 0 Vpp; (b), (f) 20 Hz and 10 Vpp; (c), (g) 70 Hz and 10 Vpp; (d), (h) 120 Hz and 10 Vpp. 112

5.7 High resolution FESEM images of particles on glass substrate in case of lab synthesized silica particles (10-20 nm in diameter) (a), (b) depicts the images for as purchased Eri silk fabric and (c), (d) depicts the images for treates Eri silk fabric. 112

5.8 The graphs show the area (μm^2) covered by the UV fluorescent particles (10-20 µm in diameter) on the flexible porous substrate vs. frequency (Hz) for four different frequencies, namely, 0 Hz, 20 Hz, 70 Hz, and 120 Hz, all at 10 Vpp. The blue line represents OTS-treated Eri silk flexible porous fabric, and the red line indicates as-purchased Eri silk flexible porous fabric. 113

5.9 Optical images of particles on the flexible porous substrate in case of UV fluorescent particles (10-20 µm in diameter). The first row depicts the images for as-purchased Eri silk flexible porous fabric and the second row shows the images for OTS-treated Eri silk flexible porous fabric for frequencies: (a), (e) 0 Hz and 0 Vpp; (b), (f) 20 Hz and 10 Vpp; (c), (g) 70 Hz and 10 Vpp; (d), (h) 120 Hz and 10 Vpp. 114

A.2.1 Optical images of the deposited patterns of Nile red after complete 123

evaporation. The dye concentration was 1 mg/mL for all the solutions. All scale bars represent 1mm.

A.2.2 Optical images of the deposited patterns of fluorescein after complete evaporation. The dye concentration was 1 mg/mL for all the solutions. All scale bars represent 1mm. 123

A.2.3 Optical images of the deposited patterns of fluorescein Na salt after complete evaporation. The dye concentration was 1 mg/mL for all solutions. All scale bars represent 1 mm. 124

A.3.1 Graphs showing the pore size distribution of all types of masks used herein. The Black dashed line is the droplet size distribution plot for the value of x : a, 5 cm b, 15 cm. The experimental set-up is shown and x is denoted in Figure 3.6a (Chapter 3). 124

A.4.1 FESEM images of different types of bandages: (A) Bandaid, (B) Crepe bandage, (C) 12-ply gauge bandage and (D) Cotton. 125

B.2.1 The schematic shows a droplet on a solid substrate with the three interfacial tension forces at the phase boundary described by Young's equation. 127

B.4.1 Working principle of Ellipsometer 128

B.10.1 Working principle of optical microscope 131

LIST OF TABLES

Tabel No.	Description	Page No.
2.1	Solubility data of different dyes	31
2.2	Initial footprint, contact angle, and time of complete evaporation for Nile Red dye	37
2.3	Initial footprint, contact angle, and time of complete evaporation for fluorescein dye	39
2.4	Initial footprint, contact angle, and time of complete evaporation for fluorescein Na salt	41
3.1	Types of masks used in the current study	59
3.2	This table shows the fractional area coverage of the absorbed dye after drying of the deposited droplets as a function of the contact angle of water on the mask materials	67
3.3	This table shows the fractional area coverage of the absorbed dye after drying of the deposited droplets at distances 0.3 m, 0.6 m, 0.9 m, 1.2 m, 1.5 m and 1.8 m	67
3.4	This table shows the percentage decrease in area covered by droplets on a mask when sprayed from a distance of 1.8 m with reference to that from 0.3 m	68
4.1	Different type of bandages used in the current study	90
5.1	Different types of porous substrates used in the current study	106
5.2	The experiments were performed in the following vibration range	107

LIST OF CONTENTS

		Page No.
	Nomenclature	**XXVIII**
	List of figures	**XXXII**
	List of tables	**XL**
1	**Introduction**	
	1.1. Chronological evolution of concepts of different contact angle	2
	1.2. Breakthrough in surface engineering	3
	1.3. Variations in surface found in nature	4
	1.4. Characterization of various surfaces	7
	1.4.1 Static contact angle	7
	1.4.2 Contact Angle Hysteresis	7
	1.4.3 Sliding Angle	8
	1.4.4 Adhesive force	9
	1.5. Surface deposition techniques	9
	1.5.1 Chemical Deposition Processes	10
	1.5.2 Physical Vapour Deposition (PVD) Processes	13
	1.6 Self-Assembled Monolayer (SAM) on a substrate for surface modification	14
	References	16
2	**Toward Controlling Evaporative Deposition: Effects of Substrate, Solvent and Solute**	
	Abstract	26
	2.1. Introduction	27
	2.2. Experimental Section	30
	2.2.1. Preparation of substrate	30
	2.2.2. Preparation of solution	31
	2.2.3. Experimental setup	31
	2.2.4. Contact angle measurement and quantitative analysis	32
	2.3. Results and Discussion	33
	2.3.1 Evaporative Deposition of Nile Red	33
	2.3.2 Evaporative Deposition of Fluorescein	37
	2.3.3 Evaporative Deposition of Fluorescein Na salt	40

2.3.4. Effect of contact line pinning 44
2.3.5. Controlling the deposition patterns 46
2.4. Conclusions 48
References 50
3 Nanometer-Thick Extremely Hydrophobic Coating Renders Cloth Mask Potentially Effective Against Aerosol-Driven Infections
Abstract 55
3.1. Introduction 56
3.2. Materials And Methods 59
3.2.1. Type of Masks 59
3.2.2. Materials 60
3.2.3. Experimental setup 60
3.2.4. Preparation of octadecyltrichlorosilane (OTS) solution 60
3.2.5. Preparation of hydrophobic Eri silk 61
3.2.6. Characterization of hydrophobic Eri silk 62
3.2.7. Quantitative analysis 64
3.3. Results and Discussion 64
3.3.1. Hydrophobicity and Liquid Absorption Capacity of Mask Fabrics 64
3.3.2. Droplet size and porosity of mask 69
3.3.3 Droplet impact on a treated mask 72
3.3.4. The breathability of the treated mask 75
3.4 Conclusion 78
References 80
4 Chemically Coated Robust Reusable Highly Hydrophobic Bandages
Abstract 86
4.1. Introduction 87
4.2 Experimental Methods 89
4.2.1. Types of bandages 89
4.2.2. Experimental setup 90
4.2.3. Preparation of octadecyltrichlorosilane (OTS) solution 90
4.2.4. Preparation of hydrophobic bandage 91
4.2.5. Contact angle measurement and quantitative analysis 91
4.3 Results and Discussion 91

4.3.1. Hydrophilicity of bandages 91
4.3.2. Functionality of modified OTS treated bandages 94
4.3.3. The distinction between as-purchased bandaid and OTS-treated bandaid 95
4.3.4. Reusability of the OTS treated crepe bandage 96
4.4. Conclusion 97
References 98

5 Microparticle Penetration Through Vibrating Porous Flexible Substrate

Abstract 102
5.1. Introduction 103
5.2. Experimental Methods 106
5.2.1. Materials 106
5.2.2. Experimental setup 106
5.2.3. Preparation of silica particles 107
5.2.4. Preparation of octadecyltrichlorosilane (OTS) solution 109
5.2.5. Preparation of hydrophobic Eri silk 109
5.2.6. Quantitative and quantitative analysis 110
5.3 Results and Discussion 110
5.3.1. Generation of sine waves 110
5.3.2. Area covered by the penetrated particles on glass substrate 110
5.3.3. Area covered by particles on flexible porous substrate 113
5.4. Conclusion 114
References 115

6 Conclusion and scope for future work

6.1 Conclusion 118
6.2 Future Scopes 120
Appendix-A 122
Appendix-B 126

Chapter 1

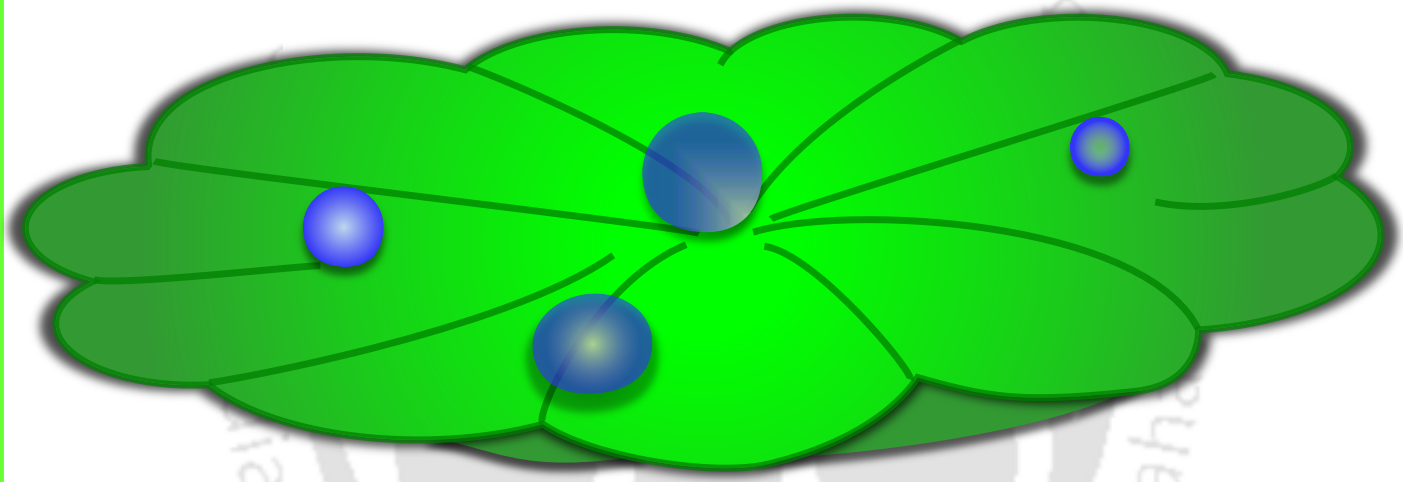

Chapter 1
Introduction

1.1. Chronological evolution of concepts of different contact angle

Surface science describes the physical and chemical changes that occur both at the surface and interface between solid-liquid, solid-gas, solid-vacuum, and liquid-gas systems.[1] The history dates back to 1805 when Thomas Young formulated Young's equation[2] which gives the relationship between contact angle θ, surface free energy of the solid γ_{sg}, interfacial tension between solid and liquid γ_{sl} and surface tension of the liquid γ_{lg}. The Young's Equation is given as:

$$\gamma_{sg} = \gamma_{sl} + \gamma_{lg} cos\theta_y$$

However, this equation is valid only for ideal homogenous surfaces, but in reality, all surfaces are generally microscopically rough and chemically non-uniform. Subsequently, in 1936, Robert Wenzel modified the Young's Equation to demonstrate the relationship between the roughness of a homogenous surface and wettability.[3] He stated that surface roughness would enhance wettability, i.e., adding surface roughness will enhance the hydrophobicity of the chemically hydrophobic surface. Based on that, he introduced a parameter *rr* called roughness ratio, and the Wenzel equation is given as:

$$\cos\theta_w = rcos\theta_y$$

$$rr = \frac{True\ area\ of\ the\ solid}{Projected\ area\ of\ the\ solid}$$

In 1944, Cassie and Baxter[4] derived another equation taking porous substrate as the chemically heterogeneous medium where liquid does not penetrate the air spaces present on the rough surface. The equation is given as:

$$cos\theta_{cb} = f_1 cos\theta_y - f_2$$

$$f_1 = Fractional\ area\ of\ solid\ surface\ under\ the\ liquid\ on\ the\ substrate$$

$f_2 = Fractional\ area\ of\ air\ under\ the\ liquid\ on\ the\ substrate$

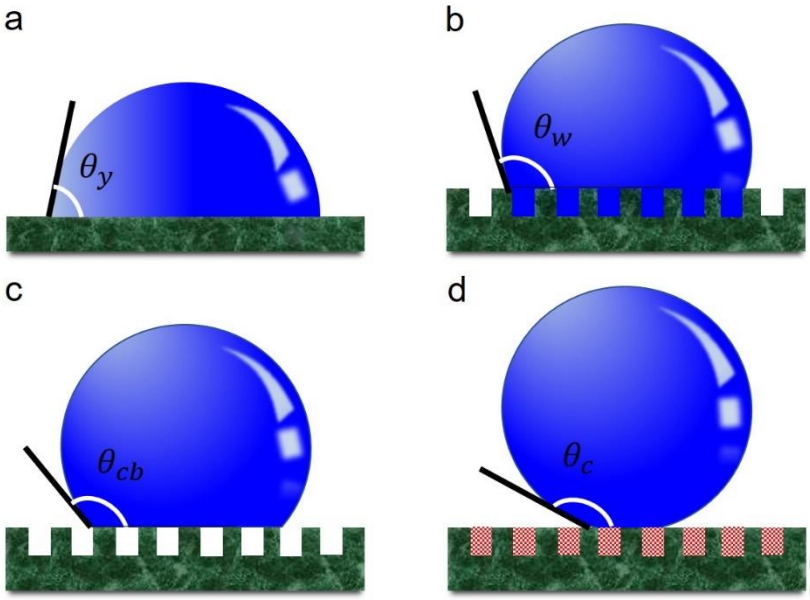

Figure 1.1. Schematic representation of different wetting behavior of a droplet placed on a substrate: (a) Young's model, (b) Wenzel's model, (c) Cassie Baxter's model, and (d) Cassie's model.

In 1948 Cassie[5] further derived Cassie's law analogous to Wenzel equation describing the contact angle based on the relationship between surface roughness and heterogeneous composite surface, given as:

$$cos\theta_c = \sigma_1 cos\theta_{y1} + \sigma_2 cos\theta_{y2}$$

$$\sigma_1 = Fractional\ surface\ area\ contact\ for\ material\ 1$$

$$\sigma_2 = Fractional\ surface\ area\ for\ material\ 2$$

1.2. Breakthrough in surface engineering

For the first time in 1964, Dettre and Johnson explained the phenomenon of superhydrophobicity using a theoretical model based on experiments done on rough hydrophobic surfaces i.e. glass beads coated with paraffin or polytetrafluoroethylene telomere.[6] However, surface engineering, which comes under the field of material science and manifests practical applications in the field of surface science, gained enormous attention only in the late twentieth century. It was Professor Barthlott[7,8] and his group that discovered extreme water repellency and self-cleaning properties of lotus leaf and termed it "lotus effect". As a result, in recent years, we

have seen tremendous importance to "surface," mostly superhydrophobic surfaces, both in academia and industry. Surface engineering techniques are generally used in automotive, aerospace, missile, power, electronic, biomedical, textile, petroleum, petrochemical, chemical, steel, cement, machine tools, and construction industries, including road surfacing. Categorically superhydrophobic materials have found potential applications in biomedical surface[9,10], anti-biofouling[11–13], transparent and anti-reflective superhydrophobic coating[14–17], anti-fogging optical surface[18–20], superhydrophobic valves[21,22], oil-water separation[23,24], self cleaning[25–27], anti-icing[28–30], water repellent electronics[31,32], enhancing buoyancy[33,34] etc.

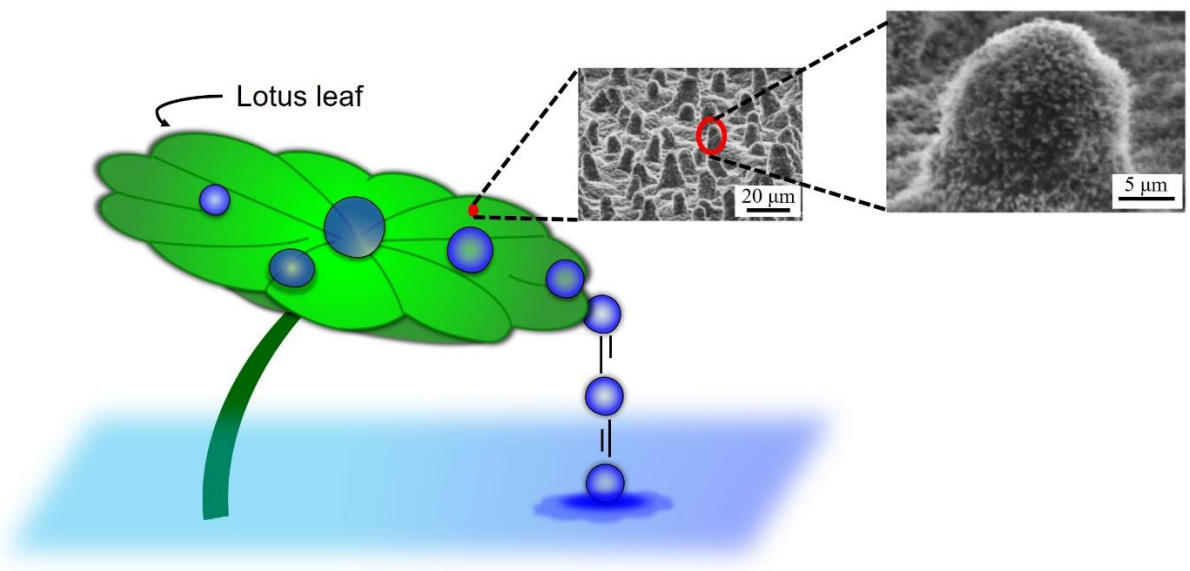

Figure 1.2. The picture shows the Superhydrophobic property of a Lotus (*Nelumbo nucifera*) leaf and the inset shows the SEM images[35] of a lotus leaf with hierarchical roughness.

1.3. Variations in surface found in nature

The nature around us is a miracle, and when we observe meticulously, we realize both the plant and animal kingdom is full of noteworthy hydrophilic and hydrophobic surfaces. These surfaces result from evolution for millions of years, and their designs sustain many unique and unusual properties. The most exciting fact is that the self-cleaning property of the lotus leaves has been familiar since ancient times. The Bhagavad Gita clearly mentioned that lotus leaves are untouched by water[36] and were considered a symbol of purity. The superhydrophobic and self-cleaning property of lotus leaves is an attribute of uniformly covered wax and hierarchical

roughness seen in lotus leaves[37,38]. The surface of lotus leaves has uniformly placed convex microbumps called papillae (Average peak-to-valley height: 13 μm and peak radius: 3 μm) and the surface of the papillae further contains nanobumps or nano-"hairs" (Average peak-to-valley height: 780 nm and peak radius: 150 nm).[35,39] The lotus effect is a special case of Cassie state as water cannot wet both the micro and nano bumps present on the surface, and usually air is trapped in these bumps. Similarly, rose petals are also superhydrophobic in nature, but unlike lotus petals, the droplets are stuck to the rose petals even after tilting or turning them upside down.[40] This high adhesion wetting state is known as the "Petal effect" due to hierarchical micro-nano structures on the petal surface. The periodic array of micropapillae has an average diameter and height of 16 μm and 7 μm repectively.[41] Each micropapillae further contains nano cuticular folds of 730 nm on its top. As the arrayed structures are larger than the lotus petal, the droplet is in Cassie impregnating Wenzel state. The water droplet can penetrate the bigger gaps between the microfolds but cannot wet the gaps between the nanofolds.[42]

The beautiful butterfly wings appear colorful and smooth to our eyes, but microscopically, they have squamous/scales and are not smooth. These scales are 40x80 μm in size with a spacing of 10-20 μm.[43,44] Additionally, each squamous have regularly placed riblets of 1000-1500 nm width. Hence, due to the air trapped in the repeated regularly arrayed similar micro-nano structures, the droplets are found in the Cassie state with WCA >140^0 for different types of butterfly wings, and the droplets roll off at an inclined angle of 3^0.[45]

Moreover, the Gecko lizard also has hierarchical structures ranging from macro to meso to micro to nanoscale. One Gecko toe contains ≈ 20 lamellae of 400-600 mm in size.[46] Each lamella has an array of thousands of stalks known as setae of length 120 μm and diameter 4.2 μm.[47,48] Further, each seta branches into millions of spatulae having several shaft levels. The final shaft level of spatulae have a diameter of 100 nm and a length 800 nm.[47,49] At the tip of the shaft, a spatula pad is present of length 300 nm, width 200 nm, and thickness 5 nm.[47,49,50] The superhydrophobicity (Cassie Baxter state with WCA= 150^0, CAH= 2^0-3^0) and dry adhesion

property (van der Waals force) of Gecko toe pads arise due to the high density of hair-like hierarchical structures and the presence of lipids on the setae.[51] However, after prolonged or repeated exposure to water, the toe pad gets transitioned into Wenzel state with complete wetting.[52]

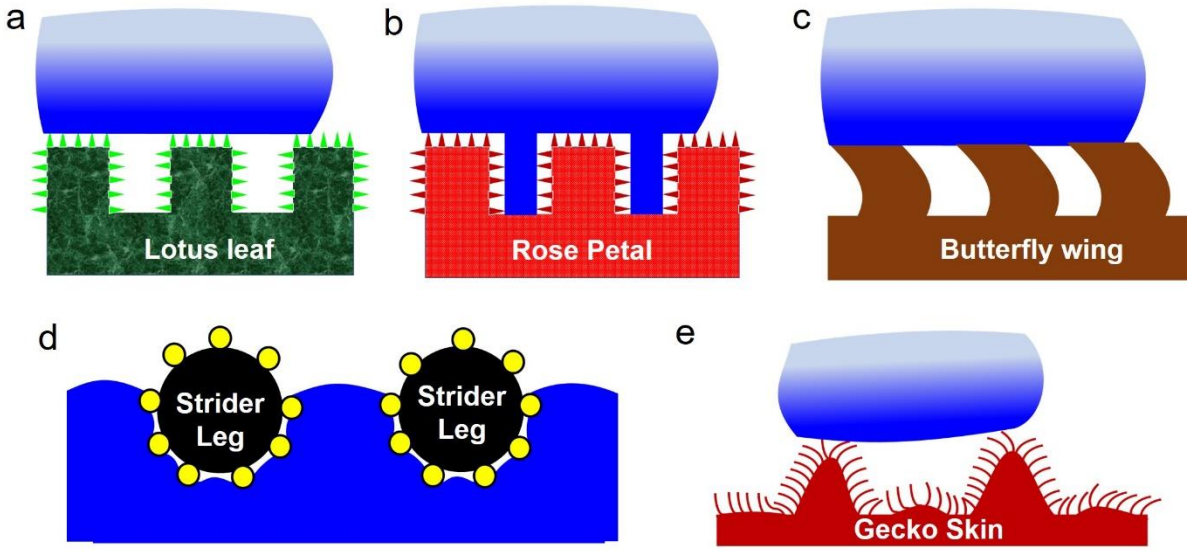

Figure 1.3. The figure shows the wetting behavior found in different objects in nature, such as: (a) Lotus leaf (Lotus effect, i.e., Special case of Cassie state), (b) Rose Petal (Petal effect, i.e., Cassie impregnating Wenzel state), (c) Butterfly wing (Cassie state), (d) Leg of strider (Coexistence of Wenzel-Cassie state) and (e) Gecko toe pad (Cassie Baxter state).

The legs of the strider have numerous needle-shaped 50 μm long setae whose diameter ranges from 3 μm to several hundred nanometers.[53] Even these structures are hierarchial as the setae further contain nano-sized grooves.[53,54] The strider can stand effortlessly or move quickly in water as the surface experiences the coexistence of both Wenzel-Cassie states.[55] The air trapped inside microsetae and nano grooves act as a cushion at the water-leg interface, thus preventing complete wetting.[56]

Some species, such as the darkling beetle, are found in one of the world's driest habitats, i.e., the African Namib Desert. The back and insect's wings have hydrophilic bumps that encourage harvesting dew from the condensation of fog. These bumps of 0.5 mm are randomly placed at a 0.5-1.5 mm distance.[57] Besides, these bumps are surrounded by hydrophobic troughs, which can collect the resulting droplets and channel them toward the beetle's mouth. The rolling-

off effect of the troughs is due to the flattened hemispheres of diameter 10 μm arranged in a regular hexagnal array.[57–59]

1.4. Characterization of various surfaces

Generally, researchers have defined that any surface with a static water contact angle (WCA) θ_{CA} >150^0 as superhydrophobic, θ_{CA} >90^0 as hydrophobic and θ_{CA} <90^0 as hydrophilic.[60,61] However, people are skeptical about the driving force that can support this definition. So, to study the wetting, dewetting and adhesive characteristics of these surfaces, both static and dynamic contact angle, sliding angle, adhesion forces etc., are commonly considered. Typically, optical contact angle instrument i.e., Goniometer connected to a syringe pump that can control the volume of dispensed liquid, is used to measure the contact angle. Additionally, the same instrument can be used as the stage in this instrument can be titled for measuring the sliding angle.[62,63]

1.4.1. Static contact angle

The Young's Equation is the first equation that tells us about the static WCA when a droplet is placed on a smooth homogenous substrate. Substrates with high surface energy tend to attract the water molecules towards it, thus wetting the surface.[64,65] Introducing roughness to the surface reduces the wetting area by the liquid above the substrate. The liquid is in contact with only the ridges present on the surface and not with the alternate recessed areas that have air in them, thus increasing the WCA.[66,67]

1.4.2. Contact Angle Hysteresis

Dynamic contact angle[68] forms the second basis of characterization, which has two types of contact angles, namely advancing contact angle θ_{Adv} and receding contact angle θ_{Rec}.[69] $\theta_{Adv} - \theta_{Rec}$ is known as the contact angle hysteresis (CAH) and superhydrophobic surfaces usually have low CAH.[55,61]. Apart from static WCA, contact angle hysteresis also plays an integral part in deciding the nature of the substrate. Two methods are usually used to measure the dynamic contact angle:

(a) Needle method **:** Dosing a pendant liquid droplet onto the substrate and increasing the droplet volume to measure the θ_{Adv}[70,71] and pumping out liquid from the same droplet to measure the θ_{Rec}.[72]

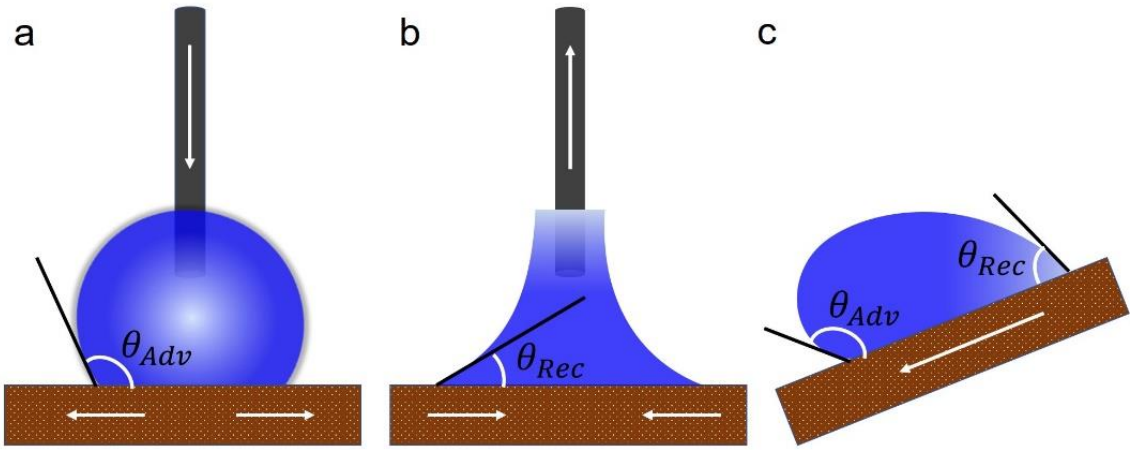

Figure 1.4. The techniques used to measure dynamic contact angle are (a) θ_{Adv} by needle method (b) θ_{Adv} by needle method and (c) Tilting method.

(b) Tilting method **:** The substrate is placed at a tilted angle with the horizontal, and the droplet is placed over it. θ_{Adv} is measured at the front of the droplet when it just starts to move while θ_{Rec} is measured at the back of the droplet at the same point[73,74].

In the Wenzel state, the water enters the rough grooves wetting the complete area of solid under the liquid, leading to pinning the contact line and increasing the solid-liquid adhesion.[75,76] It demonstrates high WCA (compared to equilibrium or θ_y), increasing θ_{Adv}, decreasing θ_{Rec} and high CAH.[77–79] However, in Cassie Baxter[80,81] air is entrapped at the valleys of the grooves, most specifically at the liquid-solid interface, which reduces the solid-liquid adhesion. It demonstrates high WCA (compared to equilibrium or θ_y), increasing both θ_{Adv} and θ_{Rec} thus low CAH, which makes the droplets roll.[78,79]

1.4.3. Sliding Angle

The sliding or roll-off angle is the critical angle between the substrate and the horizontal where the droplet starts to move due to gravity. When one end of the substrate is raised, there is minimum adhesive force between the droplet and the surface.[82–84] For both hydrophilic and

hydrophobic substrates the θ_{Adv} increases as the substrate is tilted wrt to the horizontal. Although for the superhydrophobic substrates CAH is very low i.e $\theta_{Adv} \approx \theta_{Rec}$, so the droplets roll-off when the substrate is placed at 0^0 or $<10^0$ wrt to the horizontal.[85,86]

1.4.4. Adhesive force

Another way to check the characteristics is the adhesion between solid and liquid.[65] The adhesion force is maximum in the case of a droplet placed on a hydrophilic substrate (when there is a decrease in the value of contact angle)[87] as it depends on the conformation of the microscopic three-phase contact line.[88] The adhesive force can be measured using a high-sensitivity micro-electrochemical balance system. A metal ring containing a specific volume of water droplets is placed above the sample in this instrument. The sample table approaches, contacts the metal ring, and finally leaves with a constant speed. The maximum force required to break the peak point during the sample table leaving process is taken as the value of adhesive force.[55]

1.5. Surface deposition techniques

Deposition adds a thin layer of materials that range from fractions of a nanometer to several micrometers in thickness for surface modification. The primary utility of "deposition" has been known to us since the 19th century when wet depositing metals like silver over a non-conductive substrate like glass manufactured household mirrors.[89] Simultaneously, surface modification is feasible by building up miniaturized micro-nano structures on a surface. Deposition and miniaturization, which is quite challenging, are possible through two approaches, namely, bottom-up and top-down.[90] The top-down approach is the technique of miniaturizing larger components into smaller components based on the requirements, but it has limitations in dimensional explorations smaller than 100nm.[91,92] Although this size is indeed one thousand times smaller when compared to everyday objects like a hair strand, yet Richard Feynmen[93], in his famous talk at the American Chemical Society in 1959, stated that "there is plenty of room at the bottom" due to the larger size compared to the length scale of atoms and molecules. Therefore, the bottom-up approach gained popularity where nanostructures are created by manipulating

atoms and molecules.[91,92,94] Broadly, deposition techniques can be classified as:

1.5.1. Chemical Deposition Processes

Chemical deposition, in simple terms, is depositing a solid layer when its precursor, i.e., the fluid undergoes chemical change on any solid substrate. Chemical deposition can be further divided into:

1.5.1.a. Solution based method

***(i) Plating*:** This deposition process usually requires an electrolyte with soluble salt of the coating metal, which travels through the aqueous medium to be deposited on the substrate. However, when an external power source, i.e., direct current provides the driving force, it is known as electroplating.[95,96] Presently, electroplating is mainly used to coat macro objects such as kitchenware, machinery parts, jewelry, coins, car parts, building structures, etc. Nonetheless, with the growing semiconductor industry, where the electronic components are lighter, thinner, shorter and smaller, electrochemical deposition an advanced form of electroplating, came about.[97,98] Here, the thickness of the deposited materials is usually in microns.[99,100]

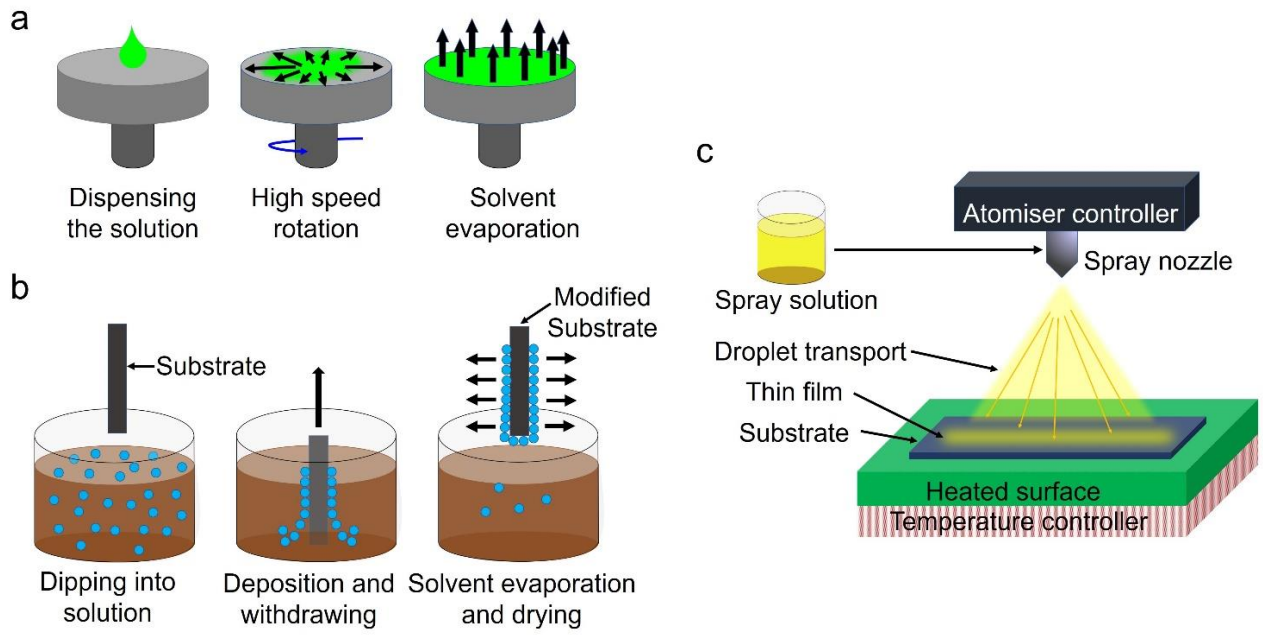

Figure 1.5. Illustration of various solution-based chemical deposition processes (a) Spin coating (b) Dip coating, and (c) Spray pyrolysis.

(ii) Chemical Solution Deposition (CSD) or Chemical Bath Deposition (CBD) : Here, a

solution of organometallic powders in an organic solvent is spin-coated to form a thin film over the substrate, which subsequently changes into a gel state when drying at a low temperature of <100 ºC.[101,102] CSD technique is used to prepare photovoltaics (like Perovskite)[103], optics, nanotubes, nanowires, nanofibres, nanomaterials, etc.[101]

(iii) Spin Coating : This versatile process involves a rotating horizontal disc where the substrate is placed for coating. After the viscous solution is placed over a substrate, it spreads over a large area of $\geq 30\ cm$ followed by evaporation of the solvent and leaving behind only the liquid or solid film.[104] This process produces highly uniform, controllable, and reproducible film thickness. Furthermore, it is applicable to inorganic, organic, and inorganic/organic solution mixtures. The deposited film has a thickness ranging from nanometres to micrometers.[105]

(v) Spray pyrolysis : This is yet another simple and inexpensive method used to deposit thin and thick films, ceramic coatings, and metal and metal oxide powders on a large scale.[111] This process is commonly used in the semiconductor industry to fabricate transparent electrical conductor film of SnO_x onto a glass substrate.[112] Basically, the solution is sprayed on the pre-heated surface whose constituents react and decompose to form chemical compounds.[113,114]

1.5.1.b. Vapour based methods

(i) Chemical Vapour deposition (CVD) : In this process, atoms, molecules, monomers etc., used as building blocks are initially converted into their gaseous form by heating or reducing the air pressure. These gaseous substances undergo either heterogeneous reaction or decomposition on the substrate to form a thin film.[115,116] This technique is very powerful and used in making sunglasses, potato chips bag[117], coatings (macro and micro-scale)[118,119], and solid thin films.[120] to high-end electronics. It is also used extensively in the high-end electronics industry to manufacture 1D carbon nanotubes[121], 2D materials such as graphene[122], and Molybdenum disulfide (MoS_2)[123] etc.

(ii) Atomic Layer Deposition (ALD) : ALD is the layer-by-layer growth technique used to

deposit a thin film of materials on a substrate from the vapor phase. Suntola and Antson first put forward this technique in the year 1977 by the name Atomic Layer Epitaxy (ALE), where two-dimensional ZnS or dielectric thin film layer was deposited for electroluminescent flat panel display.[124,125] The term ALD came into existence only around 2000 when researchers saw its potential applications in the semiconductor industry, particularly for depositing high-k oxides in microelectronic circuits.[126] ALD is the only thin-film technique that helps achieve the required uniform continuous pinhole-free films and the conformal requirements to high aspect ratio structures. Desired precursor atomic materials in gaseous states are pulsed sequentially onto the functionalized substrate to achieve the required thickness.[127,128] The excess precursor materials and reaction by-products are removed after each pulsing by purging inert carrier gas. The foremost advantage of this process is that the thickness can be controlled precisely to the Angstrom level.

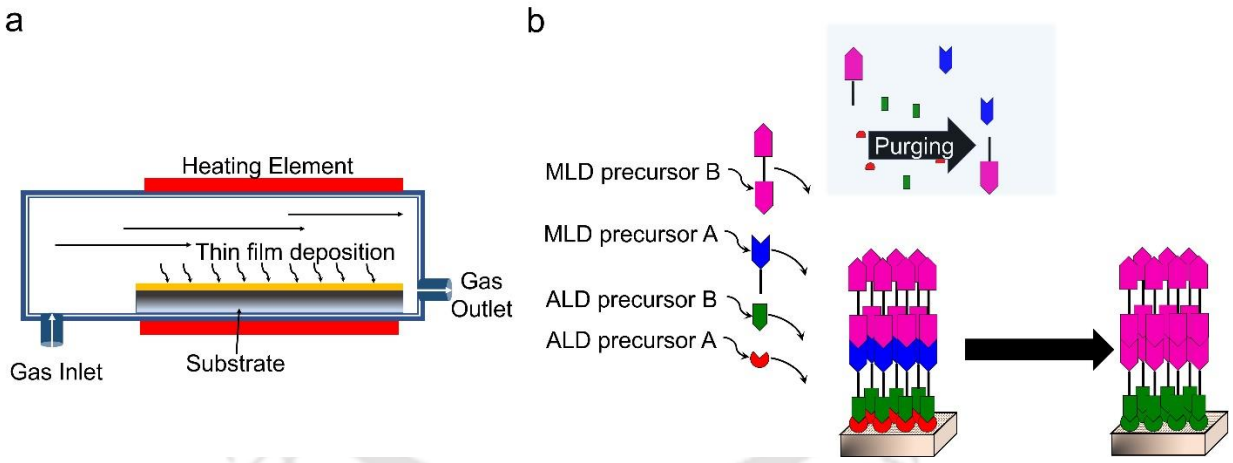

Figure 1.6. Various vapor-based chemical deposition processes (a) Chemical Vapor deposition (CVD) and (b) Combination of Atomic Layer Deposition (ALD) and Molecular Layer Deposition (MLD).

(iii) Molecular Layer Deposition (MLD) : This process is similar to ALD, where the molecular adsorption of vapor materials on the substrate occurs by alternating self-limiting and purging processes.[129,130] However, unlike ALD, where the deposition of atoms for inorganic material is done, MLD molecules are deposited on the substrate for polymer-based organic and organic-inorganic hybrid materials.[129–131] Further, the advantage of this process is that the thickness can be controlled precisely to Angstrom level even with dense organic/inorganic polymer film.[132,133]

1.5.2. Physical Vapour Deposition (PVD) Processes

This process is also known as vacuum deposition or vacuum coating, where the source material is initially in condensed form, which travels through the vacuum or low pressure environment in the form of vapor. These vapors then condense on the substrate to form a thin film coating.[134,135] They are usually two types: the source material evaporates and then condenses on the substrate and the source material is bombarded by gas ions which eject the molecules onto a substrate.

(i) Sputtering (magnetron, radio frequency, high-energy ionic scattering) : This process requires a vacuum chamber with an inert gas (for example, Argon, Krypton, Xenon, Neon, and Nitrogen) inside which there is a substrate (usually placed at the anode) and voltage applied target source material to be deposited on the substrate (usually placed at the cathode). Ionizing the inert gas creates the plasma to easily transfer electrons from target material.[136,137] These electrons collide with the outer shell of the inert gas atoms and drive off the like charge electron, thus making the inert gas atoms positive in charge. Finally, these positively charged atoms attract the negatively charged target source material at an extremely high velocity.[138] These bombarding ions have sufficient force to dislodge and eject (sputter off) atoms from the target material, which travels through the vacuum chamber and gets deposited precisely as a thin film on the substrate. The greatest advantage of this process is that the imbibed high kinetic energy helps in better adhesion of the atoms on the substrate, thus making this process suitable for fabricating anti-reflective glass coating, wear-resistant coatings, water-resistant coating, low friction coatings, anti-microbial amorphous carbon coatings etc.[139,140]

(ii) Thermal Evaporation : This technique is the simplest form of PVD. Here the source material (solid or liquid) is heated in a vacuum chamber until vapor pressure (typically between 0.1-1 Pa)[141] is reached to evaporate this material. This appreciable vapor pressure helps release the atoms and molecules from the material, thus depositing them as a thin film on the substrate.[142,143] This technique is usually compatible for large area solar cell fabrication.[144]

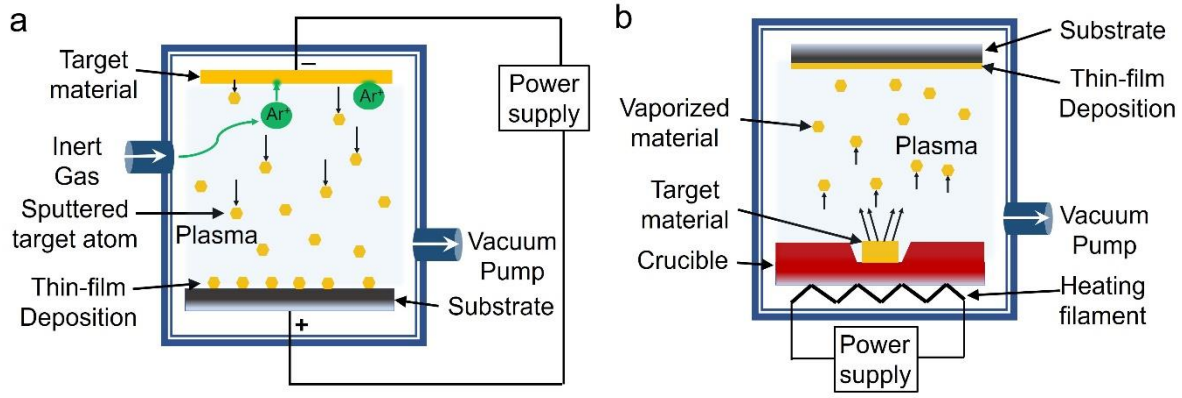

Figure 1.7. Schematic representation for physical vapor deposition (PVD) processes (a) Sputtering and (b) Thermal evaporation.

1.6. Self-Assembled Monolayer (SAM) on a substrate for surface modification

SAM is the widely used surface grafting polymerization technique where surface modification occurs when macromolecular polymer chains are orderly grafted onto an extended length scale of the substrate by covalent bonding.[145] Being a bottom-up process, it has many advantages, such as the surface can achieve required properties without changing the pristine substrate properties; easy, controllable, denser, and localized introduction of graft chains; long-term chemical stability; flexible and efficient.[145,146] The interactions responsible in effective bonding are van der Waals forces, chemisorptive bonding[147], hydrogen bonding, and electrostatic interaction. Though both solution or vapour deposition methods can be used for SAM deposition, the easiest is the simple solution chemistry performed in beakers.[148] Initially, surface activation is done through chemical reactions, ozone or UV exposure, high-energy electrons, etc., to create reactive sites on it for easy attachment of polymer molecules.[145] The two main types of organic polymer compounds used in the formation of SAM are:

(i) Alkanethiols, disulfides and sulfides (Organosulfurs): These have a strong affinity toward noble metallic surfaces such as Gold, Silver, Copper, and Platinum.[149] 16-Mercaptohexadecanoic acid (MHA)[150] and docosanethiolate are examples of some alkanethiols used in the formation of SAM on a substrate. The head group, i.e., the thiol group forms a strong bond with the substrate due to oxidative addition followed by reductive elimination of hydrogen.[151] Besides the linker

group, i.e., the rest of the molecules align with the neighbours.[152]

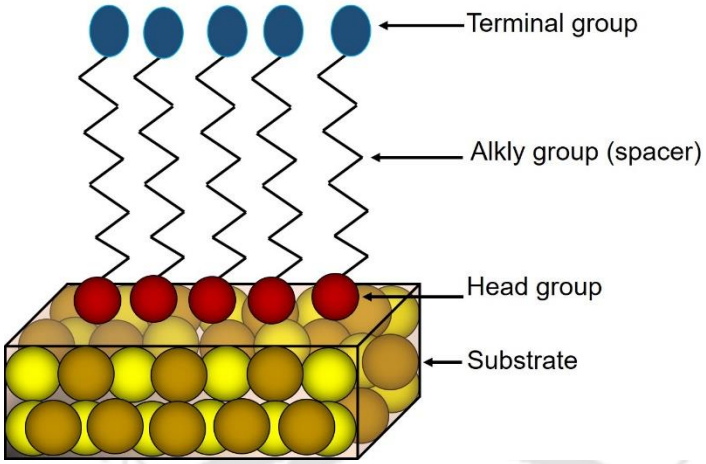

Figure 1.8. Schematic showing an ideal assemblage of Self Assembled Monolayer (SAM).

(ii) Alkylsiloxanes (Organosilnaes): Used in hydroxylic materials like glass and silica-based substrates. Alkyltrichloro/ alkyltrialkoxysilanes like Octodecyltrichlorosilane (OTS) and dimethyloctadecylchlorosilane (DMODCS)[153] are examples of extensively used organosilanes that follows two-step reaction. For example, in case of OTS, hydrolysis of the polar head group (-$SiCl_3$) occurs in the presence of water where Si-Cl bonds are converted into Si-Oh (Silanol) bonds, releasing HCl molecules in the first case. In the second step, silanol groups get strongly attracted to the hydrophilic hydroxylated silicon oxide surface forming a covalent Si-O-Si (Siloxane) bond between the surface and precursor molecules releasing a water molecule for each bond formed.[147] The thickness of the OTS monolayer is 2.6±0.2 nm with a roughness of ~1.0 Å.[154]

References

[1] K. Kolasinski, *Surface Science : Foundations of Catalysis and Nanoscience / Kurt Kolasinski*, John Wiley & Sons, **2019**.

[2] T. Young, *Philos. Trans. R. Soc. London* **1805**, 65–87.

[3] R. . Wenzel, *Ind. Eng. Chem.* **1936**, 988–994.

[4] A. B. D. Cassie, S. Baxter, *Trans. Faraday Soc.* **1944**, *40*, 546–551.

[5] A. B. D. Cassie, *Discuss. Faraday Soc.* **1948**, *3*, 11–16.

[6] R. H. Dettre, R. E. Johnson, in *Contact Angle, Wettability, Adhes.*, AMERICAN CHEMICAL SOCIETY, **1964**, pp. 112–135.

[7] C. Neinhuis, W. Barthlott, "Characterization and Distribution of Water-repellent, Self-cleaning Plant Surfaces," **1997**.

[8] W. Barthlott, C. Neinhuis, "Purity of the sacred lotus, or escape from contamination in biological surfaces," **1997**.

[9] C. A. P. Bastos, W. D. Thom, B. Reilly, I. L. Batalha, M. L. Burge Rogers, I. S. McCrone, N. Faria, J. J. Powell, *Sci. Rep.* **2020**, *10*, 1–8.

[10] E. Fadeeva, V. K. Truong, M. Stiesch, B. N. Chichkov, R. J. Crawford, J. Wang, E. P. Ivanova, *Langmuir* **2011**, *27*, 3012–3019.

[11] M. Moreno-Couranjou, R. Mauchauffé, S. Bonot, C. Detrembleur, P. Choquet, *J. Mater. Chem. B* **2018**, *6*, 614–623.

[12] S. Zhang, S. Zhang, P. Zuo, Y. Wang, Y. Wang, P. Onck, J. M. J. D. Toonder, J. M. J. D. Toonder, *ACS Appl. Mater. Interfaces* **2020**, *12*, 27726–27736.

[13] C. S. Gudipati, J. A. Finlay, J. A. Callow, M. E. Callow, K. L. Wooley, *Langmuir* **2005**, *21*, 3044–3053.

[14] S. D. Wang, Y. Y. Shu, *J. Coatings Technol. Res.* **2013**, *10*, 527–535.

[15] Y. Wu, X. Tan, Y. Wang, F. Tao, M. Yu, X. Chen, *Colloids Surfaces A Physicochem. Eng. Asp.* **2022**, *634*, 127919.

[16] Q. Zhang, H. Liu, S. Zhao, W. Dong, *Mater. Res. Express* **2021**, *8*, 046403.

[17] K. Isakov, C. Kauppinen, S. Franssila, H. Lipsanen, *ACS Appl. Mater. Interfaces* **2020**, *12*, 49957–49962.

[18] Z. Sun, T. Liao, K. Liu, L. Jiang, J. H. Kim, S. X. Dou, *Small* **2014**, *10*, 3001–3006.

[19] Z. Huang, W. Xu, Y. Wang, H. Wang, R. Zhang, X. Song, J. Li, *Micromachines* **2018**, *9*, 1–11.

[20] J. B. Chemin, S. Bulou, K. Baba, C. Fontaine, T. Sindzingre, N. D. Boscher, P. Choquet, *Sci. Rep.* **2018**, *8*, 1–8.

[21] D. L. Bark Jr, H. Vahabi, H. Bui, S. Movafaghi, B. Moore, A. K. Kota, K. Popat, L. P. Dasi, *Ann. Biomed. Eng.* **2017**, *45*, 452–463.

[22] G. Londe, A. Wesser, H. J. Cho, L. Zhai, A. Chunder, S. Subbarao, in *TRANSDUCERS 2007 - 2007 Int. Solid-State Sensors, Actuators Microsystems Conf.*, **2007**, pp. 1801–1804.

[23] H. Li, M. Zheng, L. Ma, C. Zhu, S. Lu, *Mater. Res. Bull.* **2013**, *48*, 25–29.

[24] T. Gong, J. Kim, J. Y. Woo, J. H. Jang, S. E. Lee, C. S. Han, *RSC Adv.* **2017**, *7*, 25796–25802.

[25] K. Liu, Z. Huang, A. Hemmatifar, D. I. Oyarzun, J. Zhou, J. G. Santiago, *ACS Appl. Mater. Interfaces* **2018**, *10*, 26759–26764.

[26] V. A. Ganesh, H. K. Raut, A. S. Nair, S. Ramakrishna, *J. Mater. Chem.* **2011**, *21*, 16304–16322.

[27] K. Koch, B. Bhushan, Y. C. Jung, W. Barthlott, *Langmuir* **2009**, *25*, 3240–3248.

[28] P. Tourkine, M. Le Merrer, D. Quéré, *Langmuir* **2009**, *25*, 7214–7216.

[29] L. Cao, A. K. Jones, V. K. Sikka, J. Wu, D. Gao, *Langmuir* **2009**, *25*, 12444–12448.

[30] W. Shi, L. Wang, Z. Guo, Y. Zheng, *Adv. Mater. Interfaces* **2015**, *2*, 1–8.

[31] V. K. Khanna, in *Extrem. Harsh-Environment Electron.*, IOP Publishing, **2017**, pp. 11–16.

[32] F. Ren, H. Guo, Z. Z. Guo, Y. L. Jin, H. J. Duan, P. G. Ren, D. X. Yan, *Polymers (Basel).* **2019**, *11*, 1–17.

[33] Z. Wang, X. Liu, J. Ji, T. Tao, T. Zhang, J. Xu, Y. Jiao, K. Liu, *ACS Appl. Mater. Interfaces* **2021**, *13*, 48270–48280.

[34] G. B. Hwang, A. Patir, K. Page, Y. Lu, E. Allan, I. P. Parkin, *Nanoscale* **2017**, *9*, 7588–7594.

[35] M. Nosonovsky, B. Bhushan, *Ultramicroscopy* **2007**, *107*, 969–979.

[36] *The Bhagavad-Gita*, Chicago, Ill. : The University Of Chicago Press, **1929**.

[37] T. Darmanin, F. Guittard, *Mater. Today* **2015**, *18*, 273–285.

[38] W. Barthlott, C. Neinhuis, *Planta* **1997**, *202*, 1–8.

[39] Y. T. Cheng, D. E. Rodak, *Appl. Phys. Lett.* **2005**, *86*, 144101.

[40] C. Chen, M. Liu, L. Zhang, Y. Hou, M. Yu, S. Fu, *ACS Appl. Mater. Interfaces* **2019**, *11*, 7431–7440.

[41] L. Feng, Y. Zhang, J. Xi, Y. Zhu, F. Xia, L. Jiang, *Langmuir* **2008**, *24*, 4114–4119.

[42] Z. Cheng, M. Du, H. Lai, N. Zhang, K. Sun, *Nanoscale* **2013**, *5*, 2776–2783.

[43] Y. Fang, G. Sun, T. Wang, Q. Cong, L. Ren, *Chinese Sci. Bull.* **2007**, *52*, 711–716.

[44] T. Chen, Q. Cong, Y. Qi, J. Jin, K. L. Choy, *PLoS One* **2018**, *13*, e0188775.

[45] G. Chen, Q. Cong, Y. Feng, L. Ren, *Inst. Phys. Conf. Ser.* **2003**, *180*, 245–251.

[46] M. Heim, L. Romer, T. Scheibel, *Chem. Soc. Rev.* **2010**, *39*, 156–164.

[47] Y. Tian, N. Pesika, H. Zeng, K. Rosenberg, B. Zhao, P. Mcguiggan, K. Autumn, J. Israelachvili, *Proc. Natl. Acad. Sci. U. S. A.* **2006**, *103*, 19320–19325.

[48] Y. Zhang, S. Qu, X. Cheng, X. Gao, X. Guo, *J. Bionic Eng.* **2016**, *13*, 132–142.

[49] K. Autumn, Y. A. Liang, S. T. Hsieh, W. Zesch, W. P. Chan, T. W. Kenny, R. Fearing, R. J. Full, *Nature* **2000**, *405*, 681–685.

[50] Z. L. Peng, C. Wang, S. H. Chen, *Colloids Surfaces B Biointerfaces* **2014**, *122*, 662–668.

[51] I. Badge, A. Y. Stark, E. L. Paoloni, P. H. Niewiarowski, A. Dhinojwala, *Sci. Rep.* **2014**, *4*, 1–8.

[52] A. Y. Stark, S. Subarajan, D. Jain, A. Niewiarowa, H. Peter, D. Dhinojwal, *Philos. Trans. R.*

Soc. A **2016**, *374*, 1–15.

[53] X. Feng, X. Gao, Z. Wu, L. Jiang, Q. Zheng, *Langmuir* **2007**, *23*, 4892–4896.

[54] X. Gao, L. Jiang, *Nature* **2004**, *432*, 36.

[55] S. Li, J. Huang, Z. Chen, G. Chen, Y. Lai, *J. Mater. Chem. A* **2017**, *5*, 31–55.

[56] X. Lu, H. Cai, Y. Wu, C. Teng, C. Jiang, Y. Zhu, L. Jiang, *Sci. Bull.* **2015**, *60*, 453–459.

[57] C. R. Lawrence, A. R. Parker, *Nature* **2001**, *414*, 33–34.

[58] R. P. Garrod, L. G. Harris, W. C. E. Schofield, J. McGettrick, L. J. Ward, D. O. H. Teare, J. P. S. Badyal, *Langmuir* **2007**, *23*, 689–693.

[59] X. Zeng, L. Qian, Y. Xianxia, C. Zhou, Z. Li, J. Cheng, S. Xu, S. Wang, P.-H. Pi, X. Wen, *ACS Nano* **2016**, *11*, DOI 10.1021/acsnano.6b07182.

[60] N. Verplanck, Y. Coffinier, V. Thomy, R. Boukherroub, *Nanoscale Res. Lett.* **2007**, *2*, 577–596.

[61] C. Dorrer, J. Ruhe, *Langmuir* **2006**, *22*, 7652–7657.

[62] K. G. Kabza, J. E. Gestwicki, J. L. McGrath, *J. Chem. Educ.* **2000**, *77*, 63.

[63] M. Vuckovac, M. Latikka, K. Liu, T. Huhtamäki, R. H. A. Ras, *Soft Matter* **2019**, *15*, 7089–7096.

[64] H. W. Fox, W. A. Zisman, *J. Colloid Sci.* **1950**, *5*, 514–531.

[65] W. A. ZISMAN, in *Contact Angle, Wettability, Adhes.*, AMERICAN CHEMICAL SOCIETY, **1964**, p. 1.

[66] M. Peng, T. Kurokawa, J. P. Gong, Y. Osada, Q. Zheng, *J. Phys. Chem. B* **2002**, *106*, 3073–3081.

[67] M. A. Quetzeri-Santiago, A. A. Castrejón-Pita, J. R. Castrejón-Pita, *Sci. Rep.* **2019**, *9*, 1–10.

[68] M. Miyama, Y. Yang, T. Yasuda, T. Okuno, H. K. Yasuda, *Langmuir* **1997**, *13*, 5494–5503.

[69] J. H. Kim, P. Kavehpour, J. P. Rothstein, *Phys. Fluids* **2015**, *27*, 032107.

[70] M. Jin, R. Sanedrin, D. Frese, C. Scheithauer, T. Willers, *Colloid Polym. Sci.* **2016**, *294*, 657–665.

[71] N. K. Mandsberg, R. Taboryski, *Surf. Topogr. Metrol. Prop.* **2017**, *5*, 024001.

[72] J. T. Korhonen, T. Huhtamäki, O. Ikkala, R. H. A. Ras, *Langmuir* **2013**, *29*, 3858–3863.

[73] E. Pierce, J. Carmona, A. Amirfazli, *Colloids Surfaces A Physicochem. Eng. Asp.* **2008**, *323*, 73–82.

[74] B. E. Rapp, in *Micro Nano Technol.* (Ed.: B.E.B.T.-M.M. Rapp Mechanics and Mathematics), Elsevier, Oxford, **2017**, pp. 421–444.

[75] D. Quéré, *Annu. Rev. Mater. Res.* **2008**, *38*, 71–99.

[76] T. T. Chau, W. J. Bruckard, P. T. L. Koh, A. V Nguyen, *Adv. Colloid Interface Sci.* **2009**, *150*, 106–115.

[77] J. Geils, G. Patzelt, A. Kesel, *Bionik Pat. Aus Der Natur.* **2019**, 188–195.

[78] J. Wang, Y. Wu, Y. Cao, G. Li, Y. Liao, *Colloid Polym. Sci.* **2020**, *298*, 1107–1112.

[79] B. Sahoo, K. Yoon, J. Seo, T. Lee, *Coatings* **2018**, *8*, 1–32.

[80] B. M. L. Koch, A. Amirfazli, J. A. W. Elliott, *J. Phys. Chem. C* **2014**, *118*, 23777–23782.

[81] A. Mohammad Karim, J. P. Rothstein, H. P. Kavehpour, *J. Colloid Interface Sci.* **2018**, *513*, 658–665.

[82] J. Zimmermann, M. Rabe, G. R. J. Artus, S. Seeger, *Soft Matter* **2008**, *4*, 450–452.

[83] Z. Chu, S. Seeger, *Chem. Soc. Rev.* **2014**, *43*, 2784–2798.

[84] G. R. J. Artus, S. Jung, J. Zimmermann, H. P. Gautschi, K. Marquardt, S. Seeger, *Adv. Mater.* **2006**, *18*, 2758–2762.

[85] L. Gao, T. J. Mccarthy, *Langmuir* **2008**, *24*, 546–550.

[86] G. Commentary, *J. Phys. Chem. Lett.* **2014**, *5*, 686–688.

[87] Y. Sun, Y. Li, X. Dong, X. Bu, J. W. Drelich, *Colloids Surfaces A* **2020**, *591*, 124562.

[88] D. Wang, Y. Jiang, Z. Zhu, W. Yin, K. Asawa, C. H. Choi, J. W. Drelich, *ACS Appl. Mater. Interfaces* **2020**, *36*, 2622–2628.

[89] J. Liebig, *Justus Liebigs Ann. Chem.* **1856**, *98*, 132–139.

[90] X. Meng, *J. Mater. Chem. A* **2017**, *5*, 18326–18378.

[91] V. Balzani, *Small* **2005**, *1*, 278–283.

[92] V. Balzani, *Pure Appl. Chem.* **2008**, *80*, 1631–1650.

[93] R. P. Feynman, *Eng. Sci.* **1960**, 22–36.

[94] S. Kumar, P. Bhushan, S. Bhattacharya, in (Eds.: S. Bhattacharya, A.K. Agarwal, N. Chanda, A. Pandey, A.K. Sen), Springer Singapore, Singapore, **2018**, pp. 167–198.

[95] A. A. Ojo, I. M. Dharmadasa, *Coatings* **2018**, *8*, 1–17.

[96] W. Giurlani, G. Zangari, F. Gambinossi, M. Passaponti, E. Salvietti, F. Di Benedetto, S. Caporali, M. Innocenti, *Coatings* **2018**, *8*, 1–25.

[97] F. Wang, Z. Zhao, N. Nie, F. Wang, W. Zhu, *Sci. Rep.* **2017**, *7*, 1–9.

[98] C. Zhang, N. Driver, Q. Tian, W. Jiang, H. Liu, *J. Biomed. Mater. Res. Part A* **2018**, 1887–1895.

[99] S. Li, M. S. Toprak, H. M. A. Soliman, J. Zhou, M. Muhammed, D. Platzek, E. Müller, *Chem. Mater.* **2006**, *18*, 3627–3633.

[100] P. Lansdell, J. P. G. Farr, *Trans. Inst. Met. Finish.* **1997**, *75*, 219–223.

[101] Q. Zhang, D. Sando, V. Nagarajan, *J. Mater. Chem. C* **2016**, *4*, 4092–4124.

[102] R. W. Schwartz, T. Schneller, R. Waser, *Comptes Rendus Chim.* **2004**, *7*, 433–461.

[103] R. Schwartz, *Chem. Mater.* **1997**, *9*, 2325–2340.

[104] K. Norrman, A. Ghanbari-siahkali, N. B. Larsen, *Annu. Reports Sect. C (Physical Chem.* **2005**, *101*, 174–201.

[105] E. Hedl, I. Fabijanic, I. S. Rakic, I. Vadla, J. Sancho-Parramon, *Coatings* **2021**, *11*, 1015.

[106] A. Evertz, D. Schrein, E. Olsen, G. Hoffmann, L. Overmeyer, *Opt. Fiber Technol.* **2021**, *66*, 102638.

[107] X. Tang, X. Yan, *J. Sol-Gel Sci. Technol.* **2017**, 378–404.

[108] H. S. Sundaram, X. Han, A. K. Nowinski, C. Wimbish, P. Marek, K. Senecal, S. Jiang, *ACS Appl. Mater. Interfaces* **2014**, *6*, 6664–6671.

[109] S. Lindholm, Development of a Polymeric Dip Coating Procedure for Nanosplasmonic

Fiber Optic Sensors, Chalmers University of Technology, Gothenburg, **2020**.

[110] R. Smith, H. Inomata, C. Peters, in *Introd. to Supercrit. Fluids* (Eds.: R. Smith, H. Inomata, C.B.T.-S.F.S. and T. Peters), Elsevier, **2013**, pp. 175–273.

[111] A. Zhussupbekova, D. Caffrey, K. Zhussupbekov, C. M. Smith, I. V Shvets, K. Fleischer, *ACS Appl. Mater. Interfaces* **2020**, *12*, 46892–46899.

[112] J. B. Mooney, S. B. Radding, *Annu. Rev. Mater. Sci.* **1982**, *12*, 81–101.

[113] V. K. Singh, *J. Emerg. Technol. Innov. Res.* **2017**, *4*, 910–918.

[114] S. Muthukrishnan, V. Subramaniam, T. Mahalingam, S. J. Helen, P. Sumathi, *J. Thin Film. Coat. Sci. Technol. Appl.* **2017**, *4*, 1–5.

[115] P. M. Martin, Ed. , in *Handb. Depos. Technol. Film. Coatings*, William Andrew Publishing, Boston, **2010**, pp. 1–31.

[116] S. K. Amin, H. A. M. Abdallah, M. H. Roushdy, S. A. El-Sherbiny, *Int. J. Appl. Eng. Res.* **2016**, *11*, 7708–7721.

[117] R. Messier, *MRS Bull.* **1988**, 18–21.

[118] R. Gorthy, S. Krumdieck, C. Bishop, *Materials (Basel).* **2020**, *13*, 1668.

[119] D. Vernardou, *Materials (Basel).* **2020**, *13*, 4167.

[120] L. Sun, G. Yuan, L. Gao, J. Yang, M. Chhowalla, M. H. Gharahcheshmeh, K. K. Gleason, Y. S. Choi, B. H. Hong, Z. Liu, *Nat. Rev. Methods Prim.* **2021**, *1*, 5.

[121] W. Khan, R. Sharma, P. Saini, in *Carbon Nanotub. - Curr. Prog. Their Polym. Compos.*, **2016**, pp. 1–46.

[122] Y. I. Zhang, L. Zhang, C. Zhou, *Acc. Chem. Res.* **2013**, *46*, 2329–2339.

[123] A. Zobel, A. Boson, P. M. Wilson, D. S. Muratov, D. V. Kuznetsov, A. Sinitskii, *J. Mater. Chem. C* **2016**, *4*, 11081–11087.

[124] T. Suntola, J. Antson, *Method for Producing Compound Thin Films*, **1977**.

[125] T. Suntola, *Mater. Sci. Reports* **1989**, *4*, 261–312.

[126] S. Lee, H. Kim, P. C. Mcintyre, *Appl. Phys. Lett.* **2003**, *82*, 2874–2876.

[127] S. M. George, *Chem. Rev.* **2010**, 111–131.

[128] R. W. Johnson, A. Hultqvist, S. F. Bent, *Mater. Today* **2014**, *17*, 236–246.

[129] X. Meng, *J. Mater. Chem. A* **2017**, 18326–18378.

[130] R. L. Patel, Y. Jiang, X. Liang, *Ceram. Int.* **2015**, *41*, 2240–2246.

[131] Y. Zhao, X. Sun, *ACS Energy Lett.* **2018**, *3*, 899–914.

[132] X. Liang, A. W. Weimer, *Curr. Opin. Solid State Mater. Sci.* **2015**, *19*, 115–125.

[133] A. A. Dameron, D. Seghete, B. B. Burton, S. D. Davidson, A. S. Cavanagh, J. A. Bertrand, S. M. George, *Chem. Mater.* **2008**, *20*, 3315–3326.

[134] A. S. H. Makhlouf, in *Nanocoatings Ultra-Thin Film.* (Ed.: A.S.H. Makhlouf), Woodhead Publishing, **2011**, pp. 3–23.

[135] K. Reichelt, X. Jiang, *Thin Solid Films* **1990**, *191*, 91–126.

[136] P. Sigmund, *Phys. Rev.* **1969**, *184*, 383–416.

[137] A. Zhou, in *Adv. Sci. Technol. Mn+1AXn Phases* (Ed.: I.M.B.T.-A. in S. and T. of M.P. Low), Woodhead Publishing, **2012**, pp. 21–46.

[138] V. S. Smentkowski, *Prog. Surf. Sci.* **2000**, *64*, 1–58.

[139] G. Sanzone, S. Field, D. Lee, J. Liu, P. Ju, M. Wang, P. Navabpour, H. Sun, J. Yin, P. Lievens, *ACS Appl. Mater. Interfaces* **2022**, *14*, 10154–10166.

[140] P. J. Kelly, R. D. Arnell, *Vacuum* **2000**, *56*, 159–172.

[141] F. Heym, B. J. M. Etzold, C. Kern, A. Jess, *Green Chem.* **2011**, *13*, 1453–1466.

[142] O. A. Fouad, A. A. Ismail, Z. I. Zaki, R. M. Mohamed, *Appl. Catal. B Environ.* **2006**, *62*, 144–149.

[143] X. Ma, M. Shi, *Nano-Micro Lett.* **2013**, *5*, 135–139.

[144] S. Wang, X. Li, J. Wu, W. Wen, Y. Qi, *Curr. Opin. Electrochem.* **2018**, *11*, 130–140.

[145] E. Ruckenstein, Z. F. Li, *Adv. Colloid Interface Sci.* **2005**, *113*, 43–63.

[146] C. Silien, M. Buck, R. Madueno, M. T. Ra, *Nature* **2008**, *454*, 618–621.

[147] J. Barriga, B. Coto, B. Fernandez, *Tribol. Int.* **2007**, *40*, 960–966.

[148] T. Manifar, A. Rezaee, M. Sheikhzadeh, S. Mittler, *Appl. Surf. Sci.* **2008**, *254*, 4611–4619.

[149] W. Senaratne, L. Andruzzi, C. K. Ober, *Biomacromolecules* **2005**, *6*, 2427–2448.

[150] F. C. Meldrum, J. Flath, W. Knoll, *Langmuir* **1997**, *13*, 2033–2049.

[151] A. Ulman, *Chem. Rev.* **1996**, *96*, 1533–1554.

[152] K. H. Smith, E. Tejeda-Montes, M. Poch, A. Mata, *Chem. Soc. Rev.* **2011**, *40*, 4563–4577.

[153] S. Monolayers, D. L. Angst, G. W. Simmons, *Langmuir* **1991**, *7*, 2236–2242.

[154] Y. Wang, M. Lieberman, *Langmuir* **2003**, *19*, 1159–1167.

Chapter 2

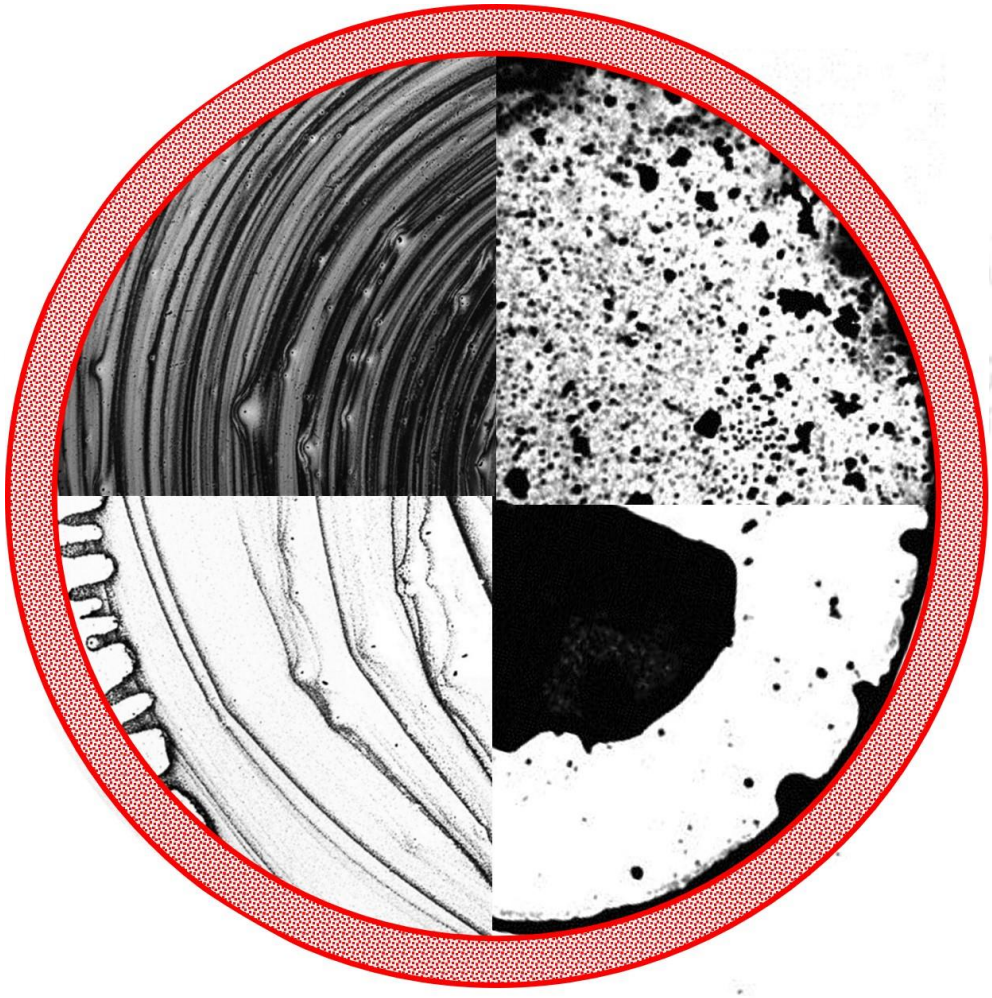

Chapter 2

Toward Controlling Evaporative Deposition: Effects of Substrate, Solvent and Solute

ABSTRACT

Understanding evaporative deposition from a colloidal suspension and on-demand control over it are important due to its industrial and biomedical applications. In particular, it is known that interactions among substrate, solute and solvent have important consequences on evaporative depositions; however, how these are affecting the deposition patterns and at which conditions these interactions are prominent need detailed investigations. Here we report that the total time of deposition (t_d) and the geometric shape of the droplet (L_C = Initial footprint diameter/Height) have a significant role in determining the evaporative deposition patterns. We have identified four zones based on t_d and L_C, and found that with longer deposition time (high t_d) and larger available space for particle motion within a liquid droplet (high L_C), deposition patterns were governed by the interactions among the substrate, solute, and solvent. We also experimentally demonstrated that the pinned contact line is indispensable for "coffee ring" effect by comparing the deposition on surfaces with and without hysteresis. The effect of Marangoni flow is also discussed, and it is shown that by controlling Marangoni flow, one can manipulate the droplet deposition from uniform disk-like to coffee ring with a central deposition.

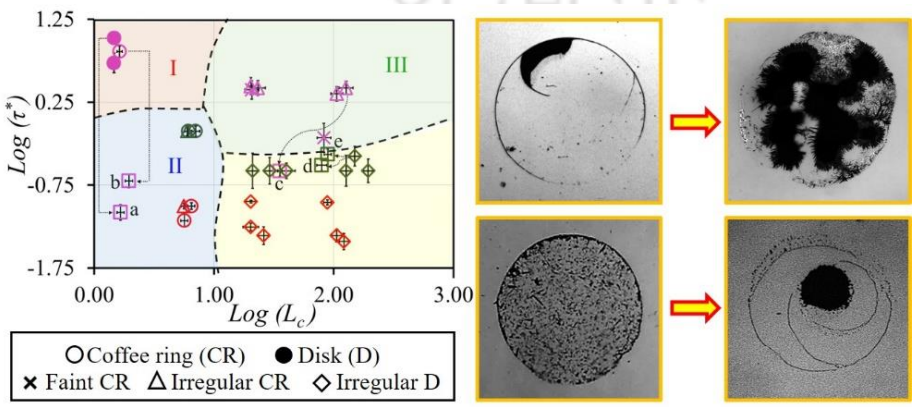

This work is published in ***J. Phys. Chem. B*** 2020, 124, 11530–11539
https://doi.org/10.1021/acs.jpcb.0c08045

2.1. Introduction

Evaporation of a suspension or a colloidal sessile droplet often leaves a ring-like stain on the surface due to the deposition of the particles near the periphery of the droplet footprint. This phenomenon is known as "coffee ring effect" and is encountered almost everyday while the drying of rain droplet on windowpane or on a windshield of a car is observed or the drying of a liquid beverage such as tea or coffee from which the term "coffee ring effect" is coined. Understanding the coffee ring effect poses an interesting challenge to the researchers due to its academic richness as well as practical importance in industrial and biomedical fronts. It has potential applications in versatile fields such as the fabrication of devices for disease diagnostics,[1,2] in patterning a high throughput sensing node using photonic crystals,[3] in fabrication of electronic chip,[4] in conventional printing[5–7] and in paint technology.[8] Controlled and fast deposition of solutions and suspensions of conductive materials by inkjet printing[5,9,10] can be employed in roll to roll fabrication of flexible microelectronics or photovoltaic applications. Recent advancements in this field also demonstrated the transformation of two-dimensional coffee stain structures into well-defined three-dimensional hollow sphere-like structures on superhydrophobic substrates.[11] In proteomics or in DNA mapping[12–14] for gene expressions, patterns created by evaporative droplets are potential candidates for diagnosis of health conditions.[1,2,15] For example, droplets containing nonmotile bacteria forms ring-like deposits after evaporation whereas motile bacteria develops disk patterns in the process of swimming toward the centre of the evaporating drops for survival. This discovery has potential applications in biosensors or bionanodevices.[16] Thus, understanding and controlling evaporative depositions of substrates from droplets is essential in achieving high efficiency in applications mentioned above.

The current knowledge on the conditions necessary for coffee ring effect[17,18] include nonzero contact angle, pinning of contact line, and volatility of the solvent. It was pointed out that the rate of evaporation is not uniform throughout the droplet surface, and it is higher near the periphery. In order to replenish the rapid drying up near the contact line, induced capillary flow of

the liquid from the interior toward the droplet periphery takes place.[8,17] However, this pinning of contact line may not be the sole criterion for the coffee ring effect to take place; rather some disk-like depositions are also associated with pinned contact line.[19,20] In an ideal wetting hysteresis free atomically smooth surface (i.e. $\theta_{Adv} \approx \theta_{Rec} \approx \theta_{Eq}$, where θ_{Adv}, θ_{Rec}, and θ_{Eq} are the advancing, receding and equilibrium contact angle of the droplet), if the contact angle of the drop deviates from its equilibrium value, the drop immediately restores back to θ_{Eq} through a continuous process,[21] thus resulting in a "stick" free contact line motion. In contrast, on a surface having defects or irregularities,[8,18] or self-pinning of the solute particles at the wedge-shaped corner of a solution droplet,[4,8] geometrical constraints[8] may lead to frequent pinning activities[22] and can induce the stick-slip like relaxation of the contact line.[23] Based on the duration of stick phase and frequency of the slip events, evaporative droplet may form multiple coffee ring structures. Bodiguel et al.[24] described a model for the deposition process, taking into account the variation of the pinning force with the velocity of the contact line. Others considered the composition (with or without surfactant) and concentration of salt solution[25] or colloidal suspension[26–28] as well. It is observed that at a low velocity of the contact line and high concentration of the solute, the droplet experiences stick-slip motion whereas, this is nullified at relatively higher velocities and low concentrations.[24,29] On the other hand, the surface tension gradient, promoting Marangoni flow, can inhibit the coffee stain phenomenon.[30,31] Variations in deposited structure, viz. conical, pillar or disk-like features from polymer solution, are also reported depending on different controlling parameters such as concentrations, contact angle, relative humidity, pressure, and temperature.[32,33]

For the last few decades, due to the advancement of the imaging technologies and computational ease, experimental[8,9,16,18,34–36] as well as theoretical[5,12,37–39] efforts were extended to understand different aspects of this phenomenon. While Wong et. al.[40] showed the importance of the solute particle size from chromatographic viewpoint, the same group in another article, also advocated for the importance of the evaporation time scale as well as the time required for meeting of two adjacent particles near the contact

line.[41] The diameter of the footprint of a droplet needs to be larger than a critical length scale to form a ring structure. The experimental results indicate that, along with the moving contact line, the dynamics of liquid-gas phase transition, the equilibrium and non-equilibrium phase behaviors, the rheology of high concentration suspensions and solutions, and the shape of a droplet play major roles in the pattern of the deposition.[42] Apart from the effect of moving contact line, dewetting comes into the picture when the contact angle is relatively small, and the droplet eventually forms a thin film of liquid containing solute particles.[34] Following analytical lubrication theory or considering the dynamics of the contact line, contact angle, net evaporative flux, and induced capillary flow within a liquid droplet, researchers attempted to simulate and describe the mechanism of particle deposition from evaporative droplets.[12,37] Initially Hu and Larson[12,37] using the finite element method (FEM) and later Breinlinger and Kraft[5] with Brownian dynamics simulated the deposition patterns from evaporative droplet.

There are plethora of literatures that report the deposition from evaporative droplets on various different surfaces such as glass,[9,17] smooth homogenous substrate like mica,[18] hydrophilic surface,[3,43] superhydrophobic substrates,[11] nondissolving or dissolving substrates,[44] and flexible substrate like PET.[9,45] Only a few systematic experimental studies for the effect of substrate on deposition pattern in the light of surface ζ potential[46,47] and fewer studies on particle-substrate interactions[48–50] are reported.

In what follows, in this chapter, we revisit this phenomenon focusing mainly on the interactions among all the three entities - solute, solvent, and the substrate. This study demonstrates that a particular solute particle from the same solution can develop different patterns on different chemically modified smooth surfaces. We offer qualitative explanation of the deposition mechanism and reason behind different types of deposition patterns such as prominent coffee ring, multiple coffee ring or uniform disk. Unlike the conventional notion,[41] it is observed that completely distinct deposition patterns, such as disk-like or coffee ring, can be obtained due to the variation in the solute-solvent-substrate interactions, even though the droplet geometry and the deposition time scale are similar. Eventually, a deposition zone diagram is presented to map the deposition patterns from a low to moderately concentrated microdroplet in the light of simple

measurable parameters such as deposition time and a characteristic geometric length scale accounting for available "space" for the distribution of solute particles. The novelty here is in identifying a specific zone where the solute-solvent-substrate interactions play a crucial role and other deposition zones where it is governed solely by the geometry of the droplets or by the solvent-substrate interaction. We anticipate that the zone diagram will serve as a guide for researchers trying to identify the initial optimized system for the required deposition pattern. We have also demonstrated that the mesoscale morphology can be manipulated by controlling the Marangoni flow inside the droplet. This on-demand Marangoni flow pattern can be achieved by inducing a directed gradient of a solvent vapor concentration across an aqueous droplet surface. This study, hopefully, will provide a better insight into the phenomenon - involving solute deposition - occurring within a droplet when it undergoes evaporation under a particular condition.

2.2. Experimental Section

2.2.1. Preparation of substrate

The experiments were carried out on atomically smooth silicon (Si) wafers (M/s N.J. International Corporation, Mumbai, Maharashtra; type/Dopant, P/Boron; orientation, <100>; single side polished), which was chemically modified to tune the surface energy. Before any modifications, the Si wafers were cleaned,[51,52] a detailed protocol of which is elaborated on in Appendix A.1.

Three types of substrates were used to carry out the experiments. First was the untreated/unmodified as purchased Si wafer (only cleaned before use), which was moderately hydrophilic in nature; second was the ozone-treated wafer, which was strongly hydrophilic in nature; and the third category was strongly hydrophobic surface, fabricated by forming self-assembled monolayer (SAM) of the octadecyl-trichlorosilane (OTS) on Si wafer.

(a) Hydrophilic substrate. The cleaned Si wafers, which were stored in DI water, were dried with a jet of nitrogen gas before carrying out the experiments. The Si wafers, after drying with nitrogen jet, were kept in the UV-ozone chamber (Novascan Technologies, Model: PSD UV4) for

60 min. After UV-ozone treatment, the surface, being of high energy and being highly reactive due to the formation of Si-O-H bond, was prone to contamination easily. Thus, experiments were carried out as soon as it was taken out of the UV-ozone chamber.

(b)Hydrophobic substrate. The Si substrate was made hydrophobic by silanizing the surface following earlier literature.[53] Briefly, the Si surface was activated in the UV-ozone chamber adopting the procedure described in the previous section. Then, the activated Si wafers were dipped in the OTS solution (mixture of 20 μL OTS in 10 mL of toluene) for 30 s. This facilitated the tethering of the Si of the OTS with the oxygen of O-Si (wafer) and the formation of Si(OTS)-O-Si(wafer) bonds.[54] The dangling hydrocarbon chain of the OTS molecule imparted hydrophobicity to the surface.

2.2.2. Preparation of solution

Three types of dye particles were used to carry out the experiments. Nile red (strongly hydrophobic), fluorescein (hydrophobic), and last, fluorescein sodium (Na) salt (strongly hydrophilic) were used to prepare solutions in two different types of solvents. One is polar solvent, i.e., deionised (DI) water and the others are toluene and chloroform, which are nonpolar solvents. The solubility data of all three dyes with the solvents are as follows:

Table 2.1. Solubility data of different dyes

Solvent / Dye	Water	Toluene	Chloroform
Nile Red	< 1 μg/mL[55]	1.79 mg/mL[56]	1 mg/mL[57]
Fluorescein	0.05 g/L[58]	Insoluble	Insoluble[59]
Fluorescein sodium salt	500 g/L[60]	Insoluble[61]	Insoluble

Keeping the above solubility data as a reference, the concentration of the dye was kept at 1 mg/mL for all the experiments unless otherwise stated. The solutions prepared were sonicated in a sonicator for about 30 min just before dispensing a droplet on the substrate.

2.2.3. Experimental setup

The schematic of the experimental setup is shown in Figure 2.1. The evaporation process of a sessile droplet on different types of the Si wafer was investigated under normal diffusion

condition by enclosing the sample in a partially closed chamber as depicted in Figure 2.1. It is a cubical enclosure, which is open at the top. A 2 μL droplet was dispensed on the substrate through the top open space of the cubical enclosure.

The dimensions of the chamber are approximately 2.5 cm x 2.5 cm x 2.5 cm. A provision for small windows at the walls was kept to monitor the droplet with a goniometer. The temperature (~ 23 ± 2 ºC) and the humidity (~ 65 ± 2 %) were maintained throughout the experiments. The droplet volume for all the experiments was fixed to 2 μL unless otherwise stated.

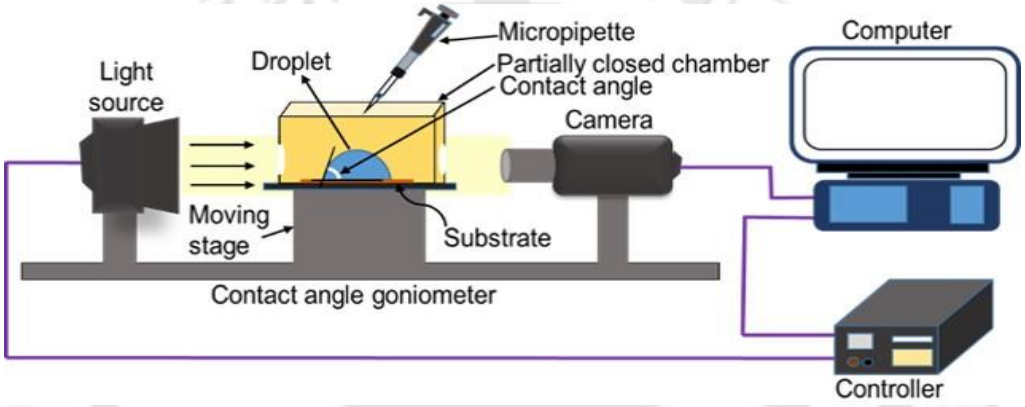

Figure 2.1. Schematic of the experimental set-up. Here, 2 μL droplets were dispensed by a micropipette on the chosen substrate fixed on a contact angle goniometer (HO-IAD-CAM-01B). The videos and images were captured using a 5MP CMOS camera and recorded on a PC for subsequent analysis.

2.2.4. Contact angle measurement and quantitative analysis

We recorded the evaporation of the droplet at a frame rate of 30 fps using a contact angle Goniometer (Holmarc Opto-Mechatronics, Model: HO-IAD-CAM-01B) to measure the contact angles with respect to time. An open-source software, "ImageJ", was used to estimate the diameter of the footprint (D_F) and the height (H) of the sessile droplets. The purpose of the experiment was to track the time evolution of the contact angle and the footprint of the droplet on different types of substrate and to estimate the total time for the complete deposition (t_d) of the dye particles.

The deposition from the completely evaporated droplets was finally observed under the optical microscope (Leica Microsystems, Model: DM2500 M and Carl Zeiss, Model: A1 MAT HAL 100). For each combination of the substrate, solute, and the solvents, the experiments were carried out at least four times to check the reproducibility.

2.3. Results and Discussion

We investigated the deposition patterns from 2 μL liquid droplets on substrates having different surface energies. Three types of interactions were considered for the qualitative analysis of the deposition patterns:

1) Interaction between particle and liquid solvent (I_{pl});

2) Interaction between particle and the substrate (I_{ps});

3) Interaction between solvent and the substrate (I_{ls});

The last interaction, I_{ls}, predominantly determines the contact angle as well as the shape of a sessile droplet on a surface. The effects of the first two interactions become important depending on the evaporation rate of the droplet (discussed later), which in turn depends on the shape of the droplet, in addition to other parameters related to the solvent. Before going into the details let us discuss the results sequentially. First, the evaporative deposition of strongly hydrophobic dye (Nile red) solution in different solvents on different substrates will be discussed followed by a moderately hydrophobic dye (fluorescein) and a hydrophilic dye (fluorescein Na salt) solution. Three different substrates were considered:

a) Ozone-treated Si wafer (strongly hydrophilic surface);

b) As-purchased Si wafer (moderately hydrophilic surface);

c) OTS-treated Si wafer (hydrophobic surface).

2.3.1 Evaporative Deposition of Nile Red

Nile red is a strongly hydrophobic dye, hence its solubility in water is much lower than the other dyes considered in this work. Figure 2.2A shows the deposition patterns of Nile red on three different surfaces (with different levels of hydrophilicity) from 2 μL droplets of chloroform, toluene, and aqueous solutions.

Based on the deposition, we have classified the patterns into (i) faint coffee ring, (ii) coffee ring, (iii) irregular disk-like (having dense multiple coffee rings), and (iv) uniform disk-like patterns. It is observed that the dye deposited from chloroform solution formed irregular disk-like shapes

on hydrophilic ozone-treated Si surface as well as on untreated Si surface. On the other hand, on a hydrophobic OTS-treated Si surface it forms predominantly a coffee ring with some deposition at a corner (pinned location) at the last stage of the evaporation (Figure 2.2.A (c)). As the rate of

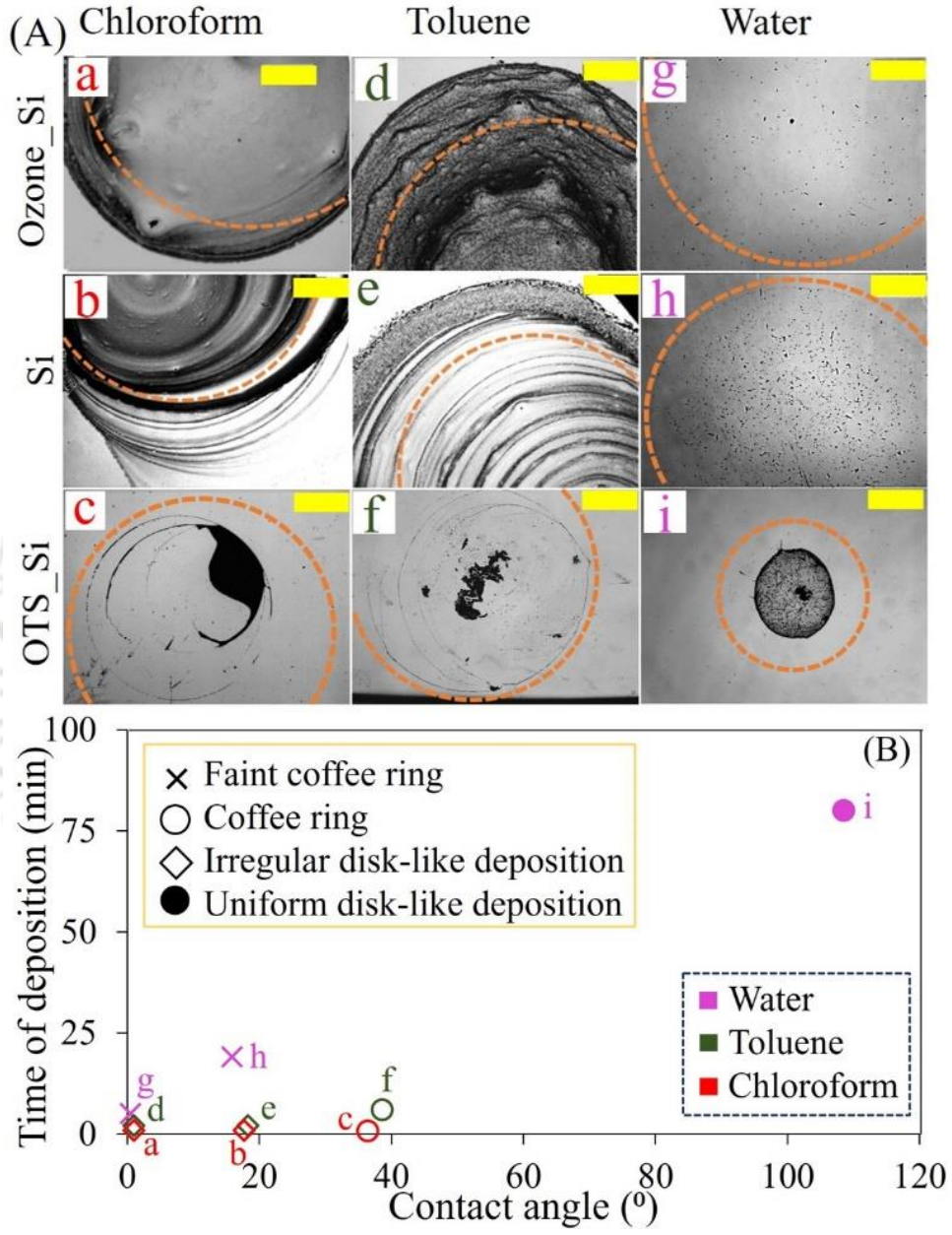

Figure 2.2. (A) Optical images of the deposited patterns of Nile red after complete evaporation. Brown dotted line indicates initial footprint (B) Overview of time of deposition against contact angle for the liquid droplet containing Nile red. The dye concentration was 1 mg/mL for all the solutions. All scale bars represent 1mm.

the evaporation of the chloroform is fast (~ 0.05 μL/s) at the room temperature of 23 °C, the droplet evaporated within 45 s. On Ozone-treated (contact angle (CA) θ ~ 0°) and on untreated Si wafer (CA, θ ~ 17°) the droplet formed thin liquid circular films. Since the contact angles were

small, particles within liquid drop got confined by the substrate and the air-liquid interface and did not get enough space for unrestricted Brownian motion. Fast evaporation of this thin liquid film led to fast deposition of particles having little space as well as time to diffuse and redistribute. This resulted in irregular disk-like patterns on the ozone-treated surface and irregular disk with multiple ring-like structures on untreated surface.

On the untreated surface, a fast stick-slip motion of the receding contact line induced multiple dense coffee ring type depositions, leading to an irregular disk-like pattern. On a hydrophobic OTS-treated Si surface (CA, θ ~ 37°), the dye particles could redistribute due to enough available space to move toward the pinned contact line. Due to fast evaporation, the deposition exhibited a few intermediate pinning states and resulted in multiple coffee rings. Here cohesive interaction among particles is stronger than the particle-substrate interaction, thus forming a ring-like deposition as the redistribution of particles was possible due to relatively higher contact angle of the liquid droplet.

Nile red in an organic nonpolar solvent like toluene followed deposition patterns similar to that from chloroform solution. In this case also, irregular disk-like deposition was observed on ozone-treated surface due to confinement of the particles in a thin liquid film (CA, θ ~ 1°). As the contact angle was low, the liquid drop spread over the surface, and because of the high mass transfer area, the evaporation rate was significant. On the other hand, on OTS-treated hydrophobic surface (CA, θ ~ 38°), the evaporation rate was comparatively slower than that on the hydrophilic surfaces and almost all the particles had sufficient time to redistribute. In this case, particles steered toward the pinned contact line due to induced capillary flow from the bulk of the droplet. On the moderately hydrophilic surface (untreated Si wafer), the deposition was irregular disk-like due to the formation of multiple dense ring-like structure. This was because of the combined effect of moderate CA (θ ~ 18°) and faster evaporation rate. Here, the pinned contact line was associated with the reduction of the contact angle with time due to evaporative mass loss and that continued to reduce until the component of the surface tension of the liquid ($\gamma_{lg} Cos\theta$) and the solid-liquid

interfacial tension (γ_{sl}) along the interface (assumed undeformed, rigid solid surface) exceeded the substrate surface tension (γ_{sg}) and the pinning force per unit length of the contact line (F_{pin}). Once the condition, $(\gamma_{lg} Cos\ \theta + \gamma_{sl}) > (\gamma_{sg} + F_{pin})$ was achieved, the contact line slipped out of the stuck position (a metastable potential well) and leaped inward to a new position (another new metastable state) with contact angle θ, close to its equilibrium contact angle θ_{Eq}. This whole process repetitively continued till the complete loss of the whole mass of the liquid droplet and in this process, multiple coffee ring depositions at the pinning positions took place.

For the aqueous solution of Nile red, as the saturation vapour pressure of water at 23 °C is less (~ 2.4 kPa) compared to that of toluene (~ 3.8 kPa) and much lesser to that of chloroform (~ 26 kPa), the total evaporation time of the aqueous droplet was longer than the case of the solution in chloroform or toluene. Although based on the substrate, the contact angle and the total effective mass transfer area as well as the total evaporation time varies, the particles get enough time to redistribute themselves based on the solvent-particle or particle-substrate interactions. Nile red—being hydrophobic in nature—has an affinity towards hydrophobic surfaces compared to hydrophilic one while deposition from aqueous solution is concerned. Thus, in case of ozone-treated hydrophilic Si wafer or untreated Si wafer, Nile red particles remained unbiased to be dispersed or deposited on the surface. Natural capillary flow induced faint coffee ring structure, and sparing distribution of the particles inside the faint coffee ring structure was observed due to final deposition of the thin liquid film as contact angle was quite small (CA ~ 0° to 16°).

In contrast, on OTS treated substrate, due to hydrophobic attractive interaction, Nile red particles preferred to be deposited on the substrate as opposed to be surrounded by polar water molecules. Also, the particles got sufficient time (~ 1 h) to be distributed and diffused, thus resulted in uniform deposition on the substrate. Table 2.2 summarises the initial footprint of the droplet, initial contact angle, and the total evaporation time for the different liquid solvents and for different substrates.

Table 2.2. Initial footprint, contact angle, and time of complete evaporation for Nile Red dye

Solvent	Concentration (mg/mL)	Type of substrate	Initial footprint (mm)	Contact angle (in degrees)	Time of complete evaporation (min)
Water	1	Ozone treated Si wafer	5.8 ± 0.49	0 ± 1	5 ± 2.02
		Bare Si wafer	4.97 ± 0.31	15 ± 1.3	19 ± 4.92
		OTS treated Si wafer	2.62 ± 0.03	108 ± 2.2	80 ± 8.81
Toluene	1	Ozone treated Si wafer	6.35 ± 0.32	1± 1	2 ± 0.85
		Bare Si wafer	6.1 ± 0.22	18 ± 1.2	2 ± 0.98
		OTS treated Si wafer	4.51 ± 0.06	38 ± 2.5	6 ± 0.85
Chloroform	1	Ozone treated Si wafer	6.2 ± 0.27	1 ± 1	0 ± 0.05
		Bare Si wafer	5.5 ± 0.20	17 ± 1.2	0 ± 0.03
		OTS treated Si wafer	4.22 ± 0.60	36 ± 2.4	0 ± 0.07

2.3.2 Evaporative Deposition of Fluorescein

Fluorescein dye has three deprotonation sites, and pK_a values of the fluorescein dye are 2.22, 4.34, 6.68.[54] This dye is relatively more polar than the Nile red but still sufficiently hydrophobic in nature.

The characteristics of the deposition from fluorescein dye resemble that of the Nile Red. The phenomena occurring inside the droplet on evaporation due to solute, solvent and substrate interactions are almost similar to the strongly hydrophobic dye (Nile Red) and is depicted in Figure 2.3. An irregular coffee ring with random patchy depositions inside it on hydrophilic ozone-treated substrate was observed after complete evaporation of the polar solvent water. As the contact angle of water on hydrophilic substrate is low, it formed a thin circular liquid film on the substrate. The evaporation rate was fast due to larger mass transfer area and dewetting of thin liquid film, leading to the formation of irregular patchy depositions.

The time taken for the evaporation of water is slightly longer than the previous case of Nile red (molecular aggregates) on hydrophilic surface, hence the particles of Fluorescein got

carried to some extent towards the contact line along with some sparing deposits inside the contact line while evaporation continued. The initial footprint, contact angle, and time of complete evaporation for all the solvents on different types of substrates are provided in Table 2.3. Identical to the strongly hydrophobic dye, Nile red, on the highly hydrophobic substrate (OTS treated Si wafer), fluorescein formed uniform disk-like deposition with the dye solution in polar solvent like water. Furthermore, after evaporation of the dye solution in nonpolar solvents (toluene and chloroform) on untreated Si wafer and ozone-treated Si wafer it formed irregular disk-like deposition, while one could find prominent coffee ring effect on OTS-treated Si wafer. FESEM images of typical representative deposition patterns from Fluorescein dye are shown in Figure 2.4.

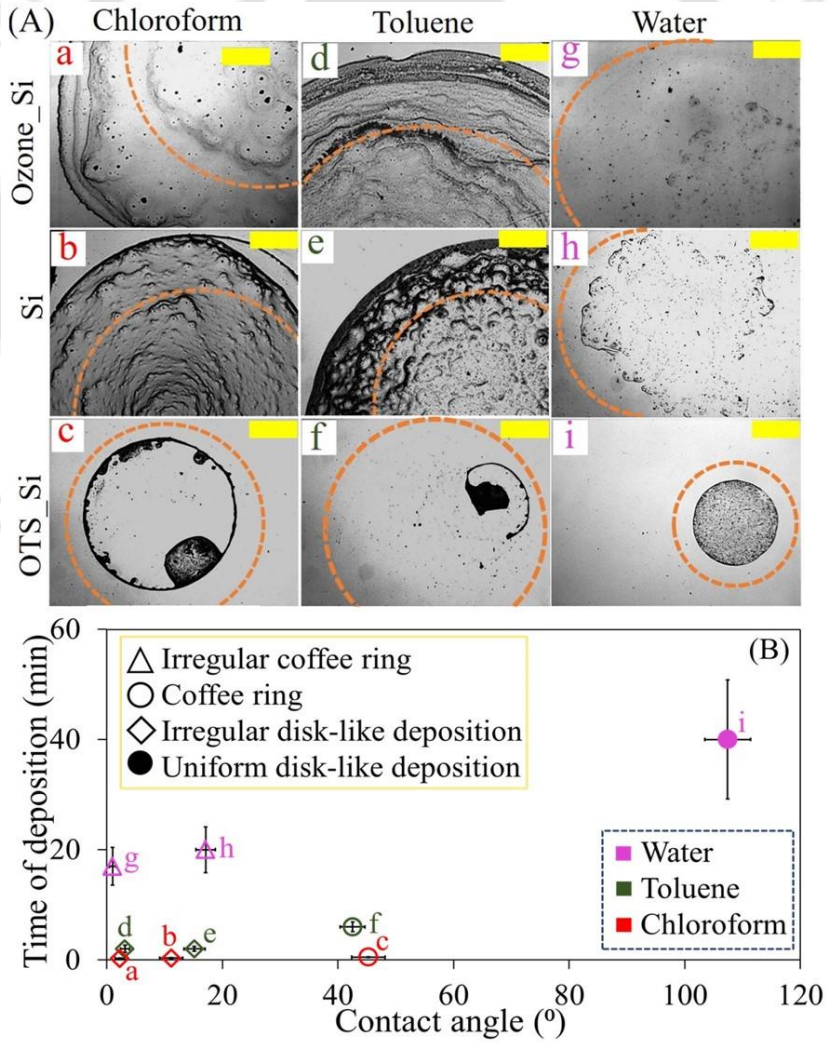

Figure 2.3. (A) Optical images of the deposited patterns of fluorescein after complete evaporation. Brown dotted line indicates initial footprint (B) Overview of time of deposition against contact angle for the fluorescein dye. The dye concentration was 1 mg/mL for all the solutions. All scale bars represent 1 mm.

Table 2.3. Initial footprint, contact angle, and time of complete evaporation for fluorescein dye

Solvent	Concentration (mg/ml)	Type of substrate	Initial footprint (mm)	Contact angle (in degrees)	Time of complete evaporation (min)
Water	1	Ozone treated Si wafer	5.3 ± 0.39	1 ± 1	17 ± 3.42
		Bare Si wafer	4.43 ± 0.21	17 ± 1.7	20 ± 4.15
		OTS treated Si wafer	2.43 ± 0.03	107 ± 4	40 ± 10.80
Toluene	1	Ozone treated Si wafer	9.7 ± 0.30	3 ± 1	2 ± 0.65
		Bare Si wafer	7.66 ± 0.24	15 ± 1.8	2 ± 0.43
		OTS treated Si wafer	4.3 ± 0.06	42 ± 2.1	6 ± 0.87
Chloroform	1	Ozone treated Si wafer	7.3 ± 0.21	2 ± 1	0.28 ± 0.06
		Bare Si wafer	6.5 ± 0.18	11 ± 2	0.33 ± 0.08
		OTS treated Si wafer	3.85 ± 0.09	45 ± 2.9	0.5 ± 0.09

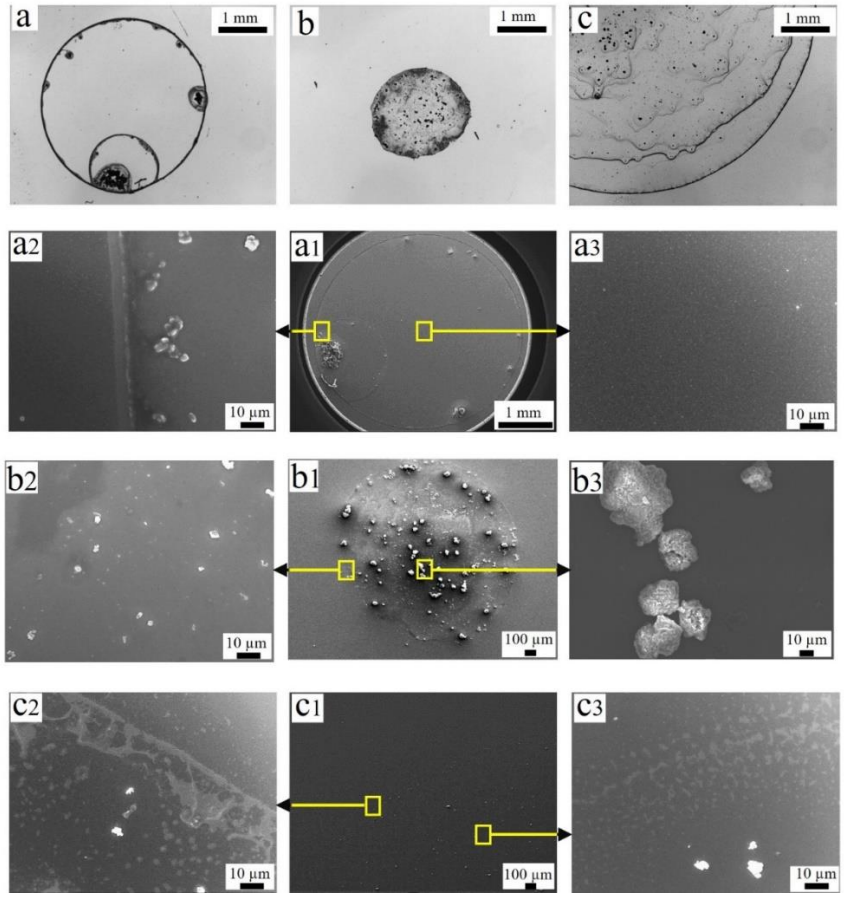

Figure 2.4. Optical images of the typical coffee ring (a), disk-like (b) and irregular (c) deposition from the fluorescein dye (similar to figure 2.3A (c), 2.3A (i) and 2.3A (d)) and the

corresponding FESEM images (a1), (b1) and (c1) respectively. a2, a3, b2, b3, c2 and c3 are the magnified FESEM images as indicated.

2.3.3 Evaporative Deposition of Fluorescein Na salt

Fluorescein Na salt is strongly polar and hydrophilic in nature and highly soluble in aqueous medium. Irrespective of the solvent, the dye was observed to have a tendency to have an irregular disk-like deposition on the hydrophilic substrate, i.e., ozone-treated surface and to some extent on untreated Si substrate. Although from water, the deposition pattern also had prominent irregular coffee ring associated with the disk-like structure.

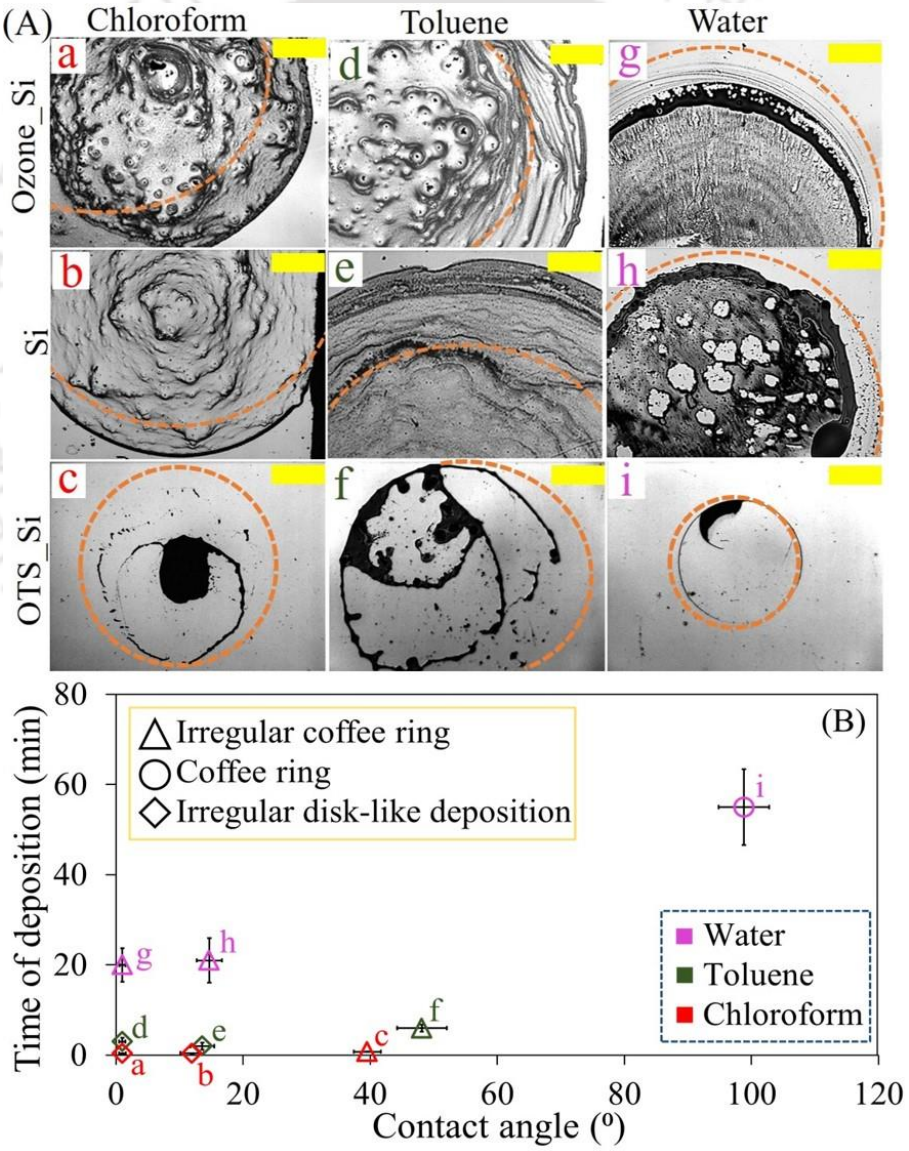

Figure 2.5. (A) Optical images of the deposited patterns of fluorescein Na salt formed after complete evaporation. Brown dotted line indicates initial footprint (B) Overview of time of deposition against contact angle for the fluorescein Na salt. The dye concentration was 1 mg/mL for all the solutions. All scale bars represent 1 mm.

On untreated Si wafer, from aqueous solution, signature of dewetted structure was present on the deposits as well (Fig 2.5.A(h)). Whereas on OTS-treated hydrophobic substrate, the dye remained in the aqueous solvent and made prominent coffee ring structure (Fig 2.5.A(i)). In case of organic solvents, the partial deposition or irregular coffee stain was observed on hydrophobic surface. The initial footprint, contact angle, time of complete evaporation for all the solvents on different types of substrates are provided in Table 2.4.

Table 2.4. Initial footprint, contact angle, and time of complete evaporation for fluorescein Na salt

Solvent	Concentration (mg/mL)	Type of substrate	Initial footprint (mm)	Contact angle (in degrees)	Time of complete evaporation (min)
Water	1	Ozone treated Si wafer	6.35 ± 0.52	1 ± 1	20 ± 3.70
		Bare Si wafer	5.9 ± 0.33	14 ± 2	21 ± 4.97
		OTS treated Si wafer	2.38 ± 0.03	98 ± 4	55 ± 8.43
Toluene	1	Ozone treated Si wafer	7.5 ± 0.39	1 ± 1	3 ± 0.83
		Bare Si wafer	7.6 ± 0.27	13 ± 1.9	2 ± 0.75
		OTS treated Si wafer	4.55 ± 0.06	48 ± 4	6 ± 0.75
Chloroform	1	Ozone treated Si wafer	5.3 ± 0.33	1 ± 1	0.33 ± 0.06
		Bare Si wafer	6.3 ± 0.23	11 ± 1.9	0.42 ± 0.04
		OTS treated Si wafer	3.6 ± 0.04	39 ± 2.1	0.75 ± 0.06

"Time" and "space" are two crucial parameters that decide how the interactions among the solute, solvent, and substrate dictate the evaporative deposition pattern. Importance of time is already pointed out in the literature in the light of evaporative time scale (τ_{evap}) and time scale of meeting of two adjacent particles near the contact line ($\tau_{particle}$).[41] Shen et al. defined a nondimensional time scale $C_R = \frac{\tau_{particle}}{\tau_{evap}}$ and showed that C_R<1 provides sufficient time to form the coffee stain effect. However, importance of geometric confinement was not considered. To address this, we introduce a nondimensional length scale defined as $L_C = \frac{D_F}{H}$, where D_F is the

diameter of the footprint just after the dispense of the droplet and *H* is the initial height of the droplet. Larger the value of the L_C, smaller is the height and the droplet is more confined for the flow of the particles. As the diffusive flow is dominant compared to the convective flow near the substrate for all practical cases of low Peclet number,[41,62] the deposition time scale t_d can be normalized by the diffusion time scale t_D such that $\tau^* \sim \frac{t_d}{t_D}$, thus representing a dimensionless time scale. The time scale, t_D can be estimated assuming one-dimensional diffusion from the relation: $t_D \sim \frac{\langle X^2 \rangle}{2D}$, where '*X*' is the thickness of the liquid layer from the substrate until which the diffusive flow is dominant and is assumed to be on the order of micron in the present experimental settings and particle loading. The diffusivity *D* is estimated from the Stokes-Einstein relationship,[63]: $\frac{D}{\mu} = k_B T$, where μ is the mobility of the particle obtained from Stokes equation $\mu = \frac{1}{6\pi\eta r}$, k_B is the Boltzmann constant and *T* is the absolute temperature.

The particle deposition will be governed by the interactions among solute, solvent and substrate if the deposition time scale τ^* is higher and L_c is smaller. This ensures enough "time" and "space" available to distribute particle on the surface depending on the solute, solvent and substrate interactions (Zone I, Figure 2.6). This zone represents either clean prominent coffee ring-like deposition or uniform disk-like patterns solely governed by all three types of interactions mentioned above.

Zone II depicts less to moderate deposition time but with larger "space" available to form prominent to irregular coffee ring-like deposition. Due to low available time (low τ^*), the deposition in this zone was not as prominent as in Zone I, thus leads to irregularities. Similarly, high τ^* and high L_c offer favourable conditions for the faint to irregular coffee ring deposition (Zone III). On the other hand, irregular disk-like deposition is observed when deposition time is small (low τ^*) and the confinement is high (high L_c) (Zone IV). Although the above zone diagram successfully depicts the deposition patterns from low to moderately concentrated micro droplets

having radius, $r \leq$ the capillary length scale ($\lambda_c \sim \sqrt{\frac{\gamma}{\rho g}}$), but for larger droplets ($r \gg \lambda_c$) also, irregular deposition was observed, which corresponds to high L_c domain.

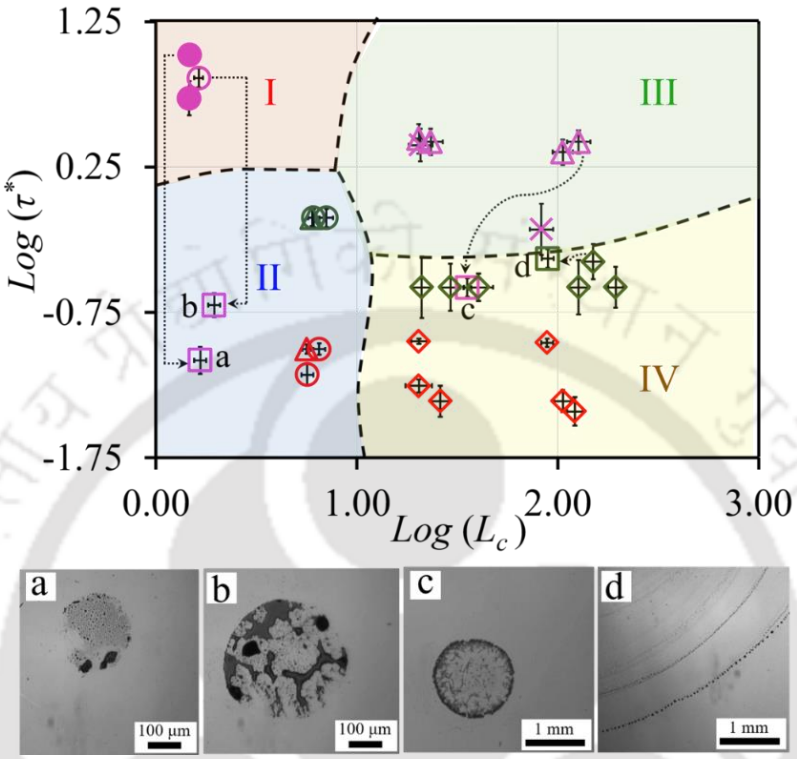

Figure 2.6. Top panel shows deposition zone diagram in terms of the dimensionless deposition time $\tau^*$and characteristic length scale L_c(see text). The symbol colors pink, green and red depict water, toluene and chloroform respectively. Filled circle (●) depicts uniform disk, open circle (○) indicates prominent coffee ring, open triangle (Δ) and cross (×) represent irregular and faint coffee rings, respectively, and open diamond (◊) depicts irregular disk-like deposition from 2 µL droplets. Zone-I depicts uniform disk and coffee ring deposition dictated by interactions among solute-solvent-substrate. Similar interactions are still valid in Zone-II but due to less deposition time, the pattern becomes irregular. Zone-III is for irregular coffee ring and faint coffee ring deposition due to low available space (high L_c). Zone-IV indicates irregular disk like deposition due to low available space (high L_c) and time (low τ^*). The square (□) symbols (a-d) in the top panel indicate depositions from droplets other than 2 µL volume. Corresponding optical micrographs (a-d) for square symbols are shown in the bottom panel (see text for details).

To examine the generic nature of the zone diagram, a few experiments were performed with varying droplet volume other than 2 µL. To observe the effect of reduced evaporation time, the deposition from a smaller droplet of aqueous Nile red solution on the OTS-treated surface was examined (Figure 2.6.a). This indeed showed the transformation of the deposition pattern from uniform disk-like (Zone I) to irregular deposition (Zone II). Similarly, coffee ring deposition (Zone I) from an aqueous fluorescein Na salt solution on OTS-treated surface changed to irregular

disk-like deposition (Zone II) (Figure 2.6.b) when the droplet size was reduced. For the transformation from Zone III to Zone IV, deposition from a smaller drop of aqueous fluorescein Na salt solution on ozone-treated substrate was examined (Figure 2.6.c). The faint coffee stain structure (in Zone III) for larger droplet of same system now showed the tendency to form irregular disk-like deposition (Zone IV). Lastly, a slight modification in the surface energy, by reducing the duration of ozone treatment of the substrate, shifted the deposition pattern of fluorescein Na salt from toluene towards the zone boundary between Zone III and Zone IV. Thus faint irregular coffee ring structures emerged which is the signature of Zone III. All these points are shown in the Zone diagram with open square symbols and the transformations are marked by dotted arrows. The optical micrographs of these deposition patterns are shown in the bottom panel of Figure 2.6.

2.3.4. Effect of contact line pinning

So far the effects of the interactions among solute, solvent, and substrate have been discussed. Along with that, pinning of the contact line is also essential for the formation of coffee ring that was pointed out by Deegan et al.[17] earlier. On a hydrophobic surface, the deposition of hydrophilic dye from aqueous solution showed a prominent coffee stain effect if only the contact line was pinned (Figure 2.4.A(i)). We intended to compare this with the deposition on slippery surface where contact line pinning is inhibited. For this purpose, hydrophobic lubricant coated surface was considered as a substrate. For this purpose, on a Poly(dimethylsiloxane) (PDMS) substrate, a thin film of silicone oil was spin-coated at a speed of 1000 rpm for 60 s. The base PDMS film was prepared by pouring a mixer of oligomer- cross-linker in the ratio of 10:1 (Sylgard (R) 184 Silicone Elastomer Kit, Dow Chemical International Pvt. Ltd. USA) on a cleaned glass slide and the thickness was maintained at ~1 mm. Then the PDMS film was cured at 60 ℃ for 2 h on a hot plate.

The experiment was performed with aqueous solution of hydrophilic dye having two different concentrations (1 mg/mL, Figure 2.7(A) and 0.25 mg/mL, Figure 2.7(B)). As the aqueous

droplet was placed on silicone oil embedded PDMS, silicone oil climbed up the periphery of the droplet slightly as shown in Figure 2.7, parts C and D. We did not witness any contact line pinning during evaporation of the droplet. Moreover, the solute being hydrophilic in nature, the dye particles showed no affinity towards the silicone oil rather remained suspended within the aqueous droplet only. As a result, at relatively higher concentration, the evaporative droplet squeezed itself to a smaller footprint and ultimately the solute accumulated to settle at the centre of the droplet. Pham et al. showed with numerical simulations that on a flat surface without contact line pinning the particle concentration increases with time towards center of the droplet gradually. On the other hand, deliberate contact line pinning makes the particle concentration higher near the pinned contact line.[64] Although those observations were reported for "thin" droplets, in our experiments, we observed the same even for not so thin droplets (low L_c) as well (Figure 2.7(C)). During the evaporation of droplet on hydrophobic lubricant-coated surface, the time scale of evaporation (~ 2 h 30 min) was much larger than normal evaporation process (~ 1 h 20 min). This was probably due to the formation of a lubricant skirt that masked the high evaporation zone of the droplet (near the contact line) and effectively reduced the mass transfer area.[65] A recent article advocates the importance of the flow field, contact line motion and the wetting state of the film surrounding the droplet on the deposition pattern of a suspension droplet.[66] Similar coffee stain to uniform deposition is also reported when contact line pinning is suppressed using a lubricant layer.[67]

The particles, which initially moved towards the periphery, similar to that on the normal hydrophobic surface as depicted in Figure 2.4.A(i) and in 2.4.B(i), retracted back to the centre due to the inertial motion of the aggregated particles and the absence of the pinned contact line (Figure 2.7(A)). These aggregated particles eventually settled when the concentration increased further due to evaporative loss of water. On the other hand, for lower concentration of particle, we could see some scattered deposition throughout the whole footprint, with major multiple depositions at the centre of the droplet. This happened because at lower concentration, agglomeration of dye particles was less, led to the deposition throughout the footprint of the droplet due to dominant

Brownian motion compared to the inertial motion (Figure 2.7(D)). When aqueous solution of hydrophobic dye, i.e., Nile red was used, the dye was absorbed on the film of hydrophobic silicone oil lubricant layer and finally diffused in the lubricant layer covering a large area (not shown here).

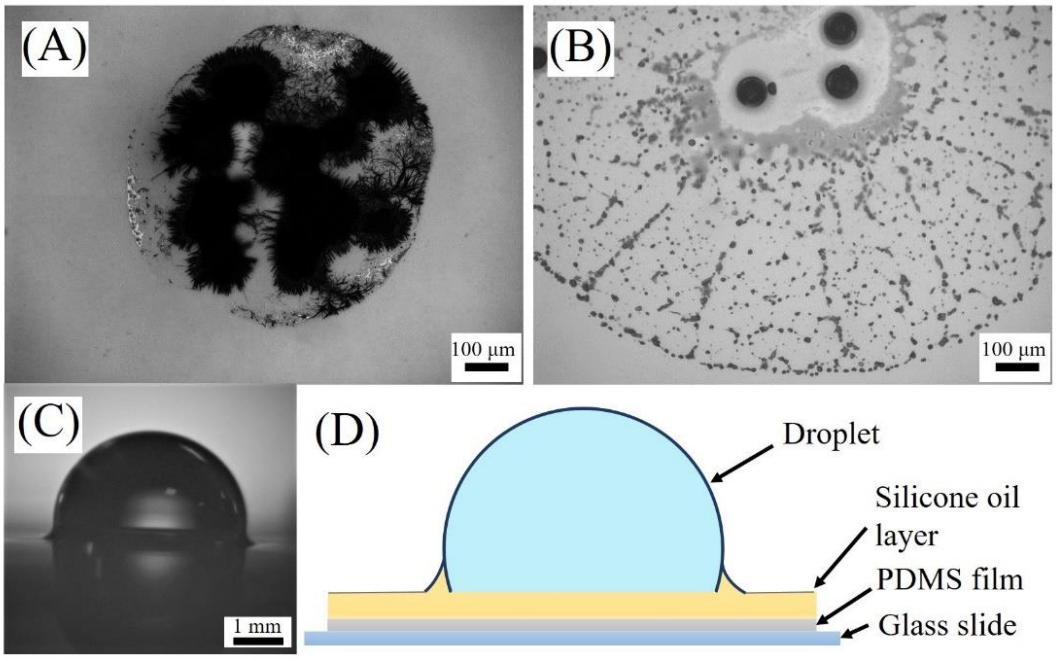

Figure 2.7. Optical images of the deposition from aqueous solution of hydrophilic dye, fluorescein Na salt, at a higher concentration (A) and at a lower concentration (B) on silicone oil layer. (C) The optical image of sessile droplet, forming the wetting ridge on the silicone oil layer. (D) Schematic showing the sessile droplet on the substrate.

2.3.5. Controlling the deposition patterns

On demand control of the deposition pattern is essential from application point of view. By introducing the gradient of the concentration of surface active molecule across the droplet surface one can induce Marangoni flow and thus can manipulate the deposition pattern. In order to demonstrate this effect, we used a cotton tip soaked in a mixture of low boiling solvents, methanol (vapour pressure =13.02 kPa, surface tension = 22.7 mN/m at 20 °C) and diethyl ether (vapour pressure =58.66 kPa, surface tension = 17 mN/m at 20 °C) strategically placed just above the centre of the evaporative water droplet or at one side of the droplet near the contact line. On the OTS-treated hydrophobic surface an aqueous droplet, containing hydrophilic Fe_2O_3 microparticles, was placed. In the first experiment a microtip containing cotton, soaked in a mixture of 1:1 volume ratio of methanol and diethyl ether, was placed over the top of the droplet.

Diethyl ether and methanol molecules preferentially accumulated at the top surface of the water droplet, due to relatively higher local concentration compared to the surroundings, and reduced the surface tension locally thus creating a surface tension gradient along the surface of the drop.

Because of Marangoni effect a circular flow, as shown in the schematic in the inset of Figure 2.8(A), took place, and the particles were carried along with the fluids due to the inertial flow. A high density (~ 5.24 g/mL) of Fe_2O_3 particles slowed down near the contact line, and the particles were deposited there due to low kinetic energy, forming a prominent coffee ring. In the process of evaporation, several pinning sites might have developed and hence multiple coffee ring formation took place. For this flow circulation, a low velocity zone or stagnant zone also might have been created at the centre of the droplet, and thus, deposition of large number of particles took place nearly at the central region of the droplet as shown in Figure 2.8(A).

In the second experiment, the tip of the methanol and diethyl ether (1:1 volume ratio) soaked cotton was placed at one side of the droplet. In this case, large deposition of the particles was observed on the opposite side of the exposure point (Figure 2.8(B)). The Marangoni flow (shown in the schematic of 2.8(B)) drove the majority of the particle towards the opposite side of the solvent exposure. Due to the Marangoni flow of attenuated intensity, in the same side of the cotton tip exposure, a faint coffee ring was also observed at the contact line. Similar experiment with low density (1.2 g/cm^3) hydrophobic dye (Nile red) showed patchy depositions in the opposite side of the solvent soaked cotton exposure without any coffee ring (Figure 2.8(C)). On the other hand, when compared with the similar system but without any solvent exposure, a drastic contrast of uniform deposition was noticed (Figure 2.8(D)). The deposition pattern also can be dynamically controlled by altering the vapor source position during the lifetime of the droplet.[68] Here we focus on the contrast and compare the deposition patterns from the same systems with and without induced Marangoni flow. Based on the requirement, one can follow the zone diagram (Figure 2.6) for natural deposition or can manipulate it by introducing the Marangoni flow as shown here in this section or by suppressing the pinning of contact line as discussed in previous

section. The results demonstrate its potential applications in paint or printing industries, in biomolecule sensing etc.

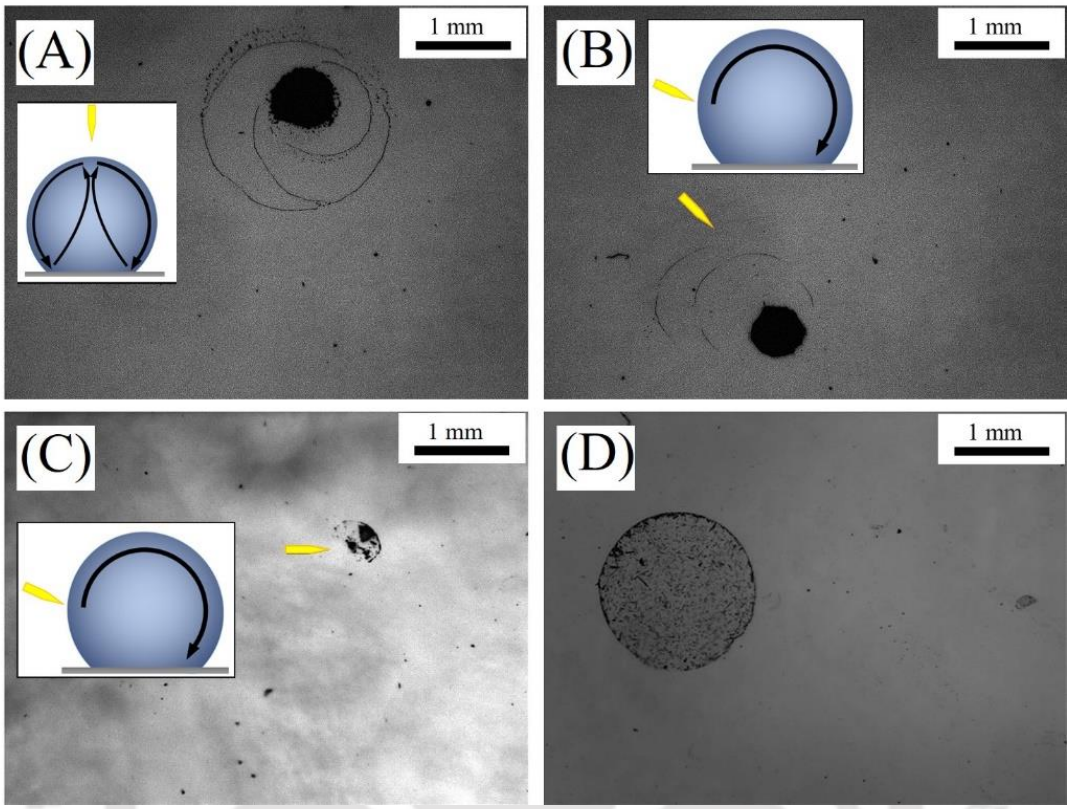

Figure 2.8. Optical images of final deposited patterns formed with hydrophilic iron oxide particles in water due to lower surface tension zone created at the (A) top and (B) the side. The substrate is OTS treated Si wafer, i.e., hydrophobic in nature. To create the low surface tension zone, mixture of methanol and diethyl ether in the ratio of 1:1 was used. The schematic shows the flow pattern inside the droplet. The yellow arrow indicates the position of the microtip containing solvent soaked cotton. Low density hydrophobic dye (Nile red) deposition from aqueous solution on OTS-treated surface with (C) and without (D) solvent vapour (methanol and diethyl ether in the ratio of 1:1) exposure are shown in the optical images.

2.4. Conclusions

It is challenging to unify the understanding of the deposition pattern from an evaporative droplet in a simplistic manner. However, additional evidence for depositions under varied experimental conditions would add to the understanding. We have attempted here to draw attention to a few aspects of the evaporative deposition in this work and demonstrated a few tunable parameters to manipulate the deposition pattern. A qualitative phase diagram-like the deposition zone diagram was identified based on time of deposition and a nondimensional length scale accounting for confinement effect:

- Zone I: It is presented that the interactions among the particle, the liquid, and the substrate governs the deposition behavior on the substrate if the time of deposition (τ^*) is high and if the nondimensional length scale L_c, which is the ratio of the initial footprint diameter to the height of the droplet, is small (i.e., no confinement).
- Zone II: Irregular deposition as well as irregular prominent coffee ring deposition was visualized due to low deposition time but with moderate confinement.
- Zone III: Irregular or faint coffee ring deposition could be observed in moderately deposition time and higher confinement.
- Zone IV: High confinement and low deposition time promoted irregular disk-like patterns.

The novel finding of this study is to identify the Zone I, where, in spite of the similar geometry of the drop shape and the deposition time, the deposition pattern can be completely different – uniform disk-like or coffee ring like due to the interactions among solute, solvent, and the substrate. Moreover, zone diagram presented using simple experimental parameters may help to design a system for required deposition patterns. It is also observed that for a prominent coffee stain effect, contact line pinning is essential but for a disk-like deposition, aggregation of particles, and thus concentration of the particles is also important. Finally, it is depicted that by regulating the surrounding ambience of the droplet, one could tune the Marangoni flow at the surface that in turn governs the internal inertial flow field of the droplet. As this internal flow field dictates the deposition patterns, one can tune this flow field by some external means, such as by electrical or magnetic actuation of the particle or by acoustic manipulation to get desired deposition of particles. This study is expected to be useful for fundamental scientific research and industrial applications that require specific micro-/nano deposition patterns of particles from colloids or suspensions.

References

[1] B. Sobac, D. Brutin, *Phys. Rev. E* **2011**, *84*, 011603.

[2] Y. Deng, X. Y. Zhu, T. Kienlen, A. Guo, *J. Am. Chem. Soc.* **2006**, *128*, 2768–2769.

[3] J. Wang, L. Wang, Y. Song, L. Jiang, *J. Mater. Chem. C* **2013**, *1*, 6048–6058.

[4] S. Magdassi, M. Grouchko, D. Toker, A. Kamyshny, I. Balberg, O. Millo, *Langmuir* **2005**, *21*, 10264–10267.

[5] T. Breinlinger, T. Kraft, *Powder Technol.* **2014**, *256*, 279–284.

[6] J. Park, J. Moon, *Langmuir* **2006**, *22*, 3506–3513.

[7] G. Hu, L. Yang, Z. Yang, Y. Wang, X. Jin, J. Dai, Q. Wu, S. Liu, X. Zhu, X. Wang, T. Wu, R. C. T. Howe, T. Albrow-owen, L. W. T. Ng, Q. Yang, L. G. Occhipinti, R. I. Woodward, E. J. R. Kelleher, Z. Sun, X. Huang, M. Zhang, C. D. Bain, T. Hasan, *Sci. Adv.* **2020**, *6*, 1–6.

[8] R. D. Deegan, O. Bakajin, T. F. Dupont, G. Huber, S. R. Nagel, T. A. Witten, *Phys. Rev. E* **2000**, *62*, 756–765.

[9] S. Biswas, S. Gawande, V. Bromberg, Y. Sun, *J. Sol. Energy Eng.* **2010**, *132*, 021010.

[10] D. Soltman, V. Subramanian, *Langmuir* **2008**, *24*, 2224–2231.

[11] I. B. Dogru, C. K. Soz, D. A. Press, R. Melikov, E. Begar, D. Conkar, E. N. F. Karalar, E. Yilgor, I. Yilgor, S. Nizamoglu, *Mater. Chem. Front.* **2017**, *1*, 2360–2367.

[12] H. Hu, R. G. Larson, *J. Phys. Chem. B* **2002**, *106*, 1334–1344.

[13] J. Jing, J. Reed, J. Huang, X. Hu, V. Clarke, J. Edington, D. Housman, T. S. Anantharaman, E. J. Huff, B. Mishra, B. Porter, A. Shenker, E. Wolfson, C. Hiort, R. Kantor, C. Aston, D. C. Schwartz, W. Englander, *Proc. Natl. Acad. Sci. U. S. A.* **1998**, *95*, 8046–51.

[14] S. Maheshwari, L. Zhang, Y. Zhu, H. C. Chang, *Phys. Rev. Lett.* **2008**, *100*, 044503.

[15] D. Brutin, B. Sobac, B. Loquet, J. Sampol, *J. Fluid Mech.* **2011**, *667*, 85–95.

[16] T. T. Nellimoottil, P. N. Rao, S. S. Ghosh, A. Chattopadhyay, *Langmuir* **2007**, *23*, 8655–

8658.

[17] R. D. Deegan, O. Bakajin, T. F. Dupont, G. Huber, S. R. Nagel, T. A. Witten, *Nature* **1997**, *389*, 827–829.

[18] R. D. Deegan, *Phys. Rev. E* **2000**, *61*, 475–485.

[19] J. Ren, A. Crivoi, F. Duan, *Langmuir* **2020**, *36*, 15064–15074.

[20] Y. Hu, B. Zhao, S. Lin, X. Deng, L. Chen, *Int. J. Heat Mass Transf.* **2020**, *159*, 120063.

[21] P. S. Goohpattader, S. Mettu, M. K. Chaudhury, *Langmuir* **2009**, *25*, 9969–9979.

[22] M. K. Chaudhury, P. S. Goohpattader, *Eur. Phys. J. E* **2013**, *36*, 1–14.

[23] S. Mettu, M. K. Chaudhury, *Langmuir* **2010**, *26*, 8131–8140.

[24] H. Bodiguel, F. Doumenc, B. Guerrier, *Langmuir* **2010**, *26*, 10758–10763.

[25] N. Basu, R. Mukherjee, *Soft Matter* **2018**, *14*, 7883–7893.

[26] V. X. Nguyen, K. J. Stebe, *Phys. Rev. Lett.* **2002**, *88*, 164501.

[27] T. Still, P. J. Yunker, A. G. Yodh, *Langmuir* **2012**, *28*, 4984–4988.

[28] D. M. Kuncicky, O. D. Velev, *Langmuir* **2008**, *24*, 1371–1380.

[29] E. Rio, A. Daerr, F. Lequeux, L. Limat, *Langmuir* **2006**, *22*, 3186–3191.

[30] M. Majumder, C. S. Rendall, J. A. Eukel, J. Y. L. Wang, N. Behabtu, C. L. Pint, T. Y. Liu, A. W. Orbaek, F. Mirri, J. Nam, A. R. Barron, R. H. Hauge, H. K. Schmidt, M. Pasquali, *J. Phys. Chem. B* **2012**, *116*, 6536–6542.

[31] R. Savino, N. Favaloro, D. Paterna, *J. Thermophys. Heat Transf.* **2002**, *16*, 562–574.

[32] D. Willmer, K. A. Baldwin, C. Kwartnik, D. J. Fairhurst, *Phys. Chem. Chem. Phys.* **2010**, *12*, 3998–4004.

[33] K. A. Baldwin, M. Granjard, D. I. Willmer, K. Sefiane, D. J. Fairhurst, *Soft Matter* **2011**, *7*, 7819–7826.

[34] U. Thiele, *Adv. Colloid Interface Sci.* **2014**, *206*, 399–413.

[35] P. J. Yunker, T. Still, M. A. Lohr, A. G. Yodh, *Nature* **2011**, *476*, 308–311.

[36] C. Monteux, F. Lequeux, *Langmuir* **2011**, *27*, 2917–2922.

[37] H. Hu, R. G. Larson, *Langmuir* **2005**, *21*, 3963–3971.

[38] J. Eggers, L. M. Pismen, *Phys. Fluids* **2010**, *22*, 112101.

[39] E. Pauliac-Vaujour, A. Stannard, C. P. Martin, M. O. Blunt, I. Notingher, P. J. Moriarty, I. Vancea, U. Thiele, *Phys. Rev. Lett.* **2008**, *100*, 176102.

[40] T. S. Wong, T. H. Chen, X. Shen, C. M. Ho, *Anal. Chem.* **2011**, *83*, 1871–1873.

[41] X. Shen, C. M. Ho, T. S. Wong, *J. Phys. Chem. B* **2010**, *114*, 5269–5274.

[42] P. J. Sáenz, A. W. Wray, Z. Che, O. K. Matar, P. Valluri, J. Kim, K. Sefiane, *Nat. Commun.* **2017**, *8*, 14783.

[43] Y. F. Li, Y. J. Sheng, H. K. Tsao, *Langmuir* **2013**, *29*, 7802–7811.

[44] M. Gonuguntla, A. Sharma, *Langmuir* **2004**, *20*, 3456–3463.

[45] E. Bormashenko, A. Musin, M. Zinigrad, *Colloids Surfaces A-physicochemical Eng. Asp.* **2011**, *385*, 235–240.

[46] R. Bhardwaj, X. Fang, P. Somasundaran, D. Attinger, *Langmuir* **2010**, *26*, 7833–7842.

[47] M. Anyfantakis, D. Baigl, *ChemPhysChem* **2015**, *16*, 2726–2734.

[48] M. Anyfantakis, Z. Geng, M. Morel, S. Rudiuk, D. Baigl, *Langmuir* **2015**, *31*, 4113–4120.

[49] Q. Yan, L. Gao, V. Sharma, Y. M. Chiang, C. C. Wong, *Langmuir* **2008**, *24*, 11518–11522.

[50] A. Crivoi, F. Duan, *Phys. Rev. E - Stat. Nonlinear, Soft Matter Phys.* **2013**, *87*, 1–8.

[51] W. Kern, J. E. Soc, *J. Electrochem. Soc.* **1990**, *137*, 1887–1892.

[52] M. Lessel, O. Bäumchen, M. Klos, H. Hähl, R. Fetzer, R. Seemann, K. Jacobs, *Surf. Interface Anal.* **2015**, *47*, 557–564.

[53] E. Orgiu, M. A. Squillaci, W. Rekab, K. Börjesson, F. Liscio, L. Zhang, P. Samorì, *Chem. Commun.* **2015**, *51*, 5414–5417.

[54] S. Smith, W. Pretorius, *Water SA* **2002**, *28*, 395–402.

[55] P. Greenspan, S. D. Fowler, *J. Lipid Res.* **1985**, *26*, 781–789.

[56] M. Ben Moshe, S. Magdassi, Y. Cohen, L. Avram, *J. Colloid Interface Sci.* **2004**, *276*, 221–226.

[57] M. Tamminga, E. Hengstmann, E. K. Fischer, *SDRP J. Earth Sci. Environ. Stud.* **2017**, *2*, 165–172.

[58] W. M. Dehn, *J. Am. Chem. Soc.* **1917**, *39*, 1399–1404.

[59] R. F. Chen, *Arch. Biochem. Biophys.* **1969**, *133*, 263–276.

[60] D. Samanta, N. Hosseini-Nassab, R. N. Zare, *Nanoscale* **2016**, *8*, 9310–9317.

[61] X. Luo, X. T. Cui, *Electrochem. commun.* **2009**, *11*, 402–404.

[62] N. Shahidzadeh, M. F. L. Schut, J. Desarnaud, M. Prat, D. Bonn, *Sci. Rep.* **2015**, *5*, 10335.

[63] A. Einstein, *Investigations on the Theory of, the Brownian Movement*, Dover Publications, INC., New York, USA, **1956**.

[64] T. Pham, S. Kumar, *Langmuir* **2017**, *33*, 10061–10076.

[65] J. H. Guan, G. G. Wells, B. Xu, G. McHale, D. Wood, J. Martin, S. Stuart-Cole, *Langmuir* **2015**, *31*, 11781–11789.

[66] Y. Li, C. Diddens, T. Segers, H. Wijshoff, M. Versluis, D. Lohse, *Proc. Natl. Acad. Sci. U. S. A.* **2020**, *117*, 16756–16763.

[67] S. Das, A. Dey, G. Reddy, D. D. Sarma, *J. Phys. Chem.* **2017**, *8*, 4704–4709.

[68] R. Malinowski, G. Volpe, I. P. Parkin, G. Volpe, *J. Phys. Chem. Lett.* **2018**, *9*, 659–664.

Chapter 3

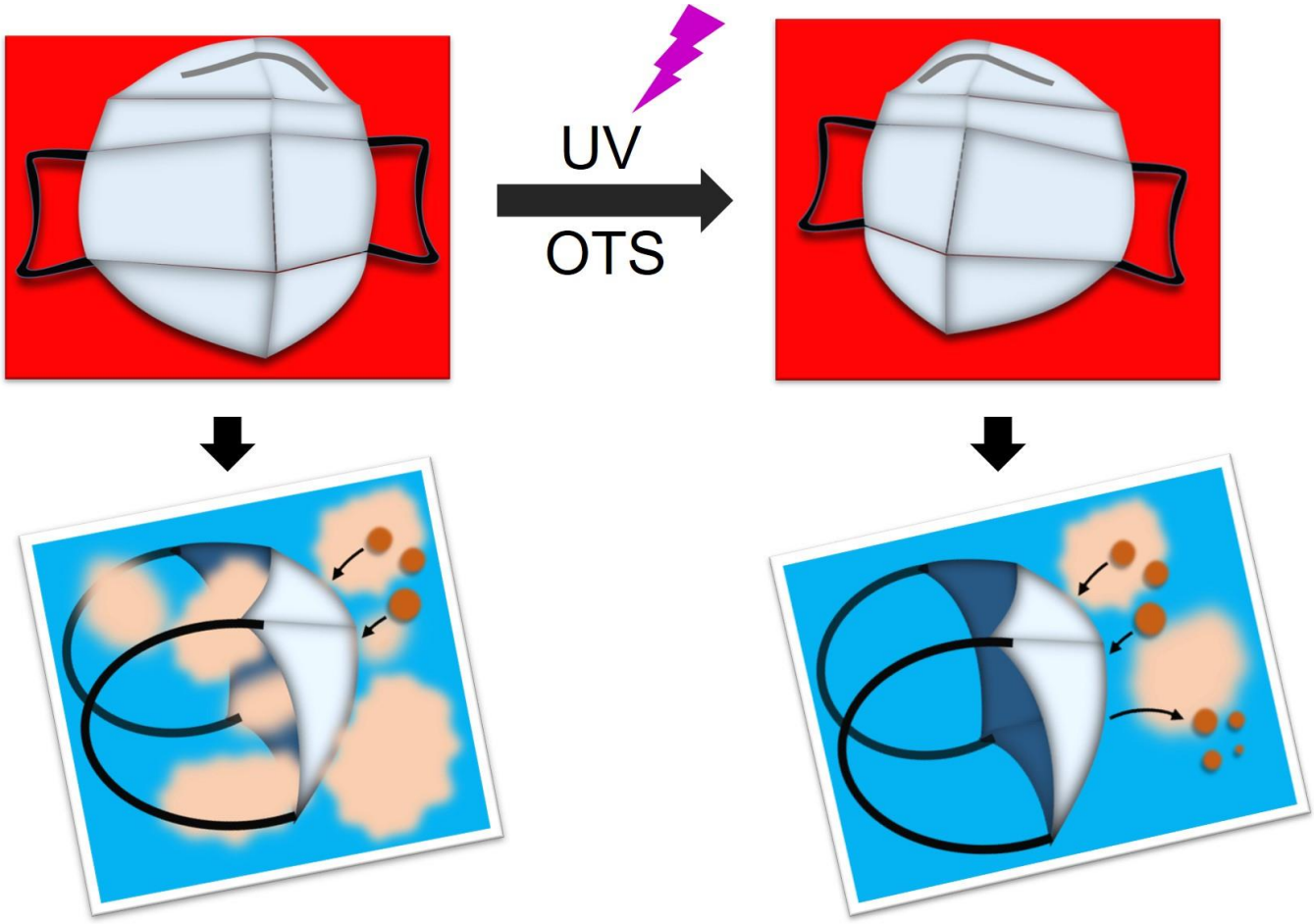

Chapter 3

Nanometer-Thick Extremely Hydrophobic Coating Renders Cloth Mask Potentially Effective Against Aerosol-Driven Infections

ABSTRACT

The advent of COVID-19 pandemic has made it necessary to wear masks across populations. While the N95 mask offers great performance against airborne infections, its multi-layered sealed design makes it difficult to breathe for a longer duration of use. The option of using highly breathable cloth or silk masks especially for a large populace is fraught with the danger of infection. As a normal cloth or silk mask absorbs airborne liquid, it can be a source of plausible infection. We demonstrate the chemical modification of one such mask, Eri silk, to make it hydrophobic (contact angle of water is 143.7^{0}), which reduces the liquid absorption capacity without reducing the breathability of the mask significantly. The breathability reduces only 22% for hydrophobic Eri silk compared to the pristine Eri silk, whereas N95 shows a 59% reduction of breathability. The modified hydrophobic silk can repel the incoming aqueous liquid droplets without wetting the surface. The results indicate that a multilayered modified silk mask to make it hydrophobic can be an affordable and breathable alternative to the N95 mask.

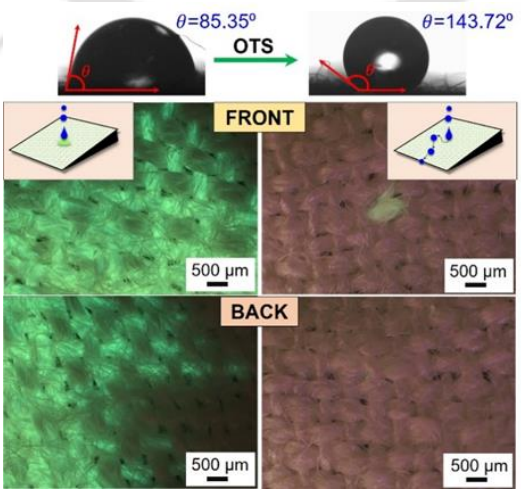

This work is published in ***ACS Appl. Bio Mater.*** 2021, 4, 7921-7931
https://doi.org/10.1021/acsabm.1c00851

3.1. Introduction

The ubiquitous presence of facemask globally in the context of the ongoing coronavirus disease - 2019 (COVID-19) pandemic underscores the need for effective preparations for prevention against aerosol-driven infections. It has been proven beyond doubt that wearing a facemask is an effective way of preventing rapid transmission of infection due to severe acute respiratory syndrome coronavirus-2 (SARS-CoV-2) through airborne droplets, especially when treatment options are still evolving. For example, although the risk of infection of SARS-CoV-2 is high within 1 m of separation,[1] studies indicate that the transmission can be prevented in a community through the use of masks.[2] It is also important to emphasize that universal access to high-performance masks is arguably one of the easiest ways of ensuring healthcare for a large populace.

The World Health Organization (WHO) recommends wearing N95 masks as a protective measure from infection due to SARS CoV-2,[3] which has an efficiency of 95% or more to block 0.3 μm particles.[4] An N95 mask is usually made up of four layers: first is a polymeric hydrophobic microfiber[5] layer to repel droplets, second is a support layer that provides rigidity, the third layer is the nonwoven meltblown polypropylene, and the fourth is again a hydrophobic layer that prevents internally created moistures from entering the filter.[6] Commercially available surgical masks are usually three-layered with a hydrophobic outer layer,[7,8] and the middle polypropylene[9] layer usually has the smallest fiber of 5.7 $\pm$ 2.8 μm diameter to act as a filtration medium[10]. Surgical masks have a filtration efficiency of >80% with respect to 50-500 nm particles; however, a significant amount of particles within 100 nm range can easily pass through them.[6] Surgical and N95 masks act as better protectors against the aerosol-driven virus but are expensive and thus are mostly used by medical personnel, scientist, and other working professionals. On the other hand, there is also demand for cost-effective and easily available alternatives, especially cloth and silk masks that suffice to meet the American Society for Testing and Materials (ASTM) standards.[11–13] However, it is reported that the transmission probability of aerosol particles through cloth mask is greater than N95.[14] The filtration efficiency of cloth mask depends on factors such as fabric

type, width, yarn count, and mass. Some silk fabrics are hydrophilic such as the Eri silk[15] and Paat silk,[13] and some are hydrophobic, such as Muga silk.[16] Masks made of cotton, natural silk, or chiffon with tighter weave are 50% effective, and four-layered silk is > 85% effective in blocking 10 nm - 6 μm ranged droplets.[17] In addition to that, 600 TPI cotton provides excellent efficiency of 98% by blocking 300 nm to 6 μm aerosol droplets.

In addition to the nature of the mask, factors such as exhale to inhale (E : I) ratio, the gap between the mask and the nose may affect the efficiency of different types of layered masks.[18] Following sneezing, the droplets can travel distances ranging from 0.5 to 0.8 m in the forward direction for a layered or surgical mask.[19] However, the sneezing droplets leaked from the sides and top of the N95 mask due to gaps between the nose and the mask can remain suspended in the air and travel 0.6 m backward. It is also reported that the secondary atomization of the droplets while passing through the different layers of masks[20] is also an important factor to be considered during selecting a mask along with appropriate filter materials and the number of layers. A double-layered surgical mask can block about 92% of the initial cough droplets of size 620 μm, whereas the secondary atomized droplets (diameter < 100 μm) consist of about 28% of total droplets transmitted[20] possessing a greater risk of transmitting the disease. Moreover, the range of droplet transmission fraction is from 0.1% in the N95 mask to 110% for polyester/spandex neck gaiter, which is higher if not wearing a mask is considered as 100%.[21]

Although the N95 mask is designed to provide 95% protection against airborne viruses, the reported penetration value for virions of 10-80 nm is 5.6% at a relatively high flow rate of 85 L/min in the certification test.[22] Also, a recent report suggests that the infection from a pathogen-laden filter needs to be considered seriously as SARS-CoV-2 can become airborne from the same.[23] A strong flow of air induced by inhalation through the contaminated filter may worsen the situation, especially when wearing a mask for the whole day.

However, fundamental to the workings of the masks is the materials and designs used to fabricate the same. For example, in a multilayered N95 mask, the major filtration work is done by

the 100 - 1000 μm thick meltblown hydrophobic[24,25] polypropylene fiber layer.[26] A comfortable mask should have a pressure drop < 8 mm water column (WC),[27] but N95 specifications make a higher pressure drop of 25-35 mm WC[6,27] and even encounter breathing resistance of 142–1 Pa.[28] As cloth or silk masks are flexible and comfortable to wear with less suffocation compared to N95,[27,28] chemical modification of such mask materials is a potential strategy to improve their performance. For example, Copper (Cu)/silver (Ag) nanoparticles incorporated reduced graphene oxide (RGO) coating increases the efficiency of cotton as a protective measure.[29] Additionally, charged[30,31] polystyrene fiber with electret effect[32] provided a high filtration efficiency of about 99.8% with a low air resistance of only 72 Pa, making it a suitable material for manufacturing a mask.[33] While large droplets (>1 μm) settle due to gravitational force after being exhaled[17,24] or adhere to the mask fibers due to the inertial impaction,[34,35] the smaller droplets (< 1 μm) may float around for a considerable time and diffuse through the pores of filters due to Brownian motion or adhere to the fiber due to interception.[34,36] Thus, to understand the transfer routes of pathogens to the human body, it is important to probe interactions between aerosol droplets and the fiber of the mask materials.

A thin and rather porous cloth mask is expected to provide the least protection against aerosol-driven viral infection. This is due to the rapid absorption of water droplets by the hydrophilic[37] cotton or silk fabrics within 7 s.[38] Hence, the question remains whether the chemical modification of the hydrophilic cotton or silk masks to hydrophobic masks retains the comfortability of breathing and at the same time provides better protection against viral infection. Herein, we report that nanometer-thick coatings by superhydrophobic molecule octadecyltricholorosilane (OTS) rendered cotton and silk fabrics resistant to the passing of aerosol droplets and thus potential mask materials against aerosol-driven viral disease such as COVID-19. Further, with high oxygen permeability, even after coating with the superhydrophobic molecule compared to the N95 mask, they provide superior options for ease of breathing with a high level of protection against aerosol-borne viral diseases such as SARS-CoV-2 for a large populace.

3.2. Materials And Methods

3.2.1. Type of Masks

In this study, we considered four different types, namely, N95 mask (manufactured by E-Spin Nanotech Pvt. Ltd., India), surgical mask (locally procured), cloth masks (locally procured), and silk masks (locally procured). We have considered the masks for study in this report based on their ease of accessibility to a large populace such as cotton mask (Cloth 1 and Cloth 2), silk mask (Muga silk, Eri silk, and Paat (Mulberry) silk), surgical mask and N95 mask (Table 3.1). Cloth masks i.e., cotton, polyester, or silk varieties are easily available and are also cost-effective. All the above-mentioned masks are being used by people for protection from airborne infections and pollution. The Muga silk is produced from a wild silkworm *Antheraea assamensis* from Assam, located in the north-eastern region of India.[39] Eri silk comes from the caterpillar *Samia ricini* that is regional to northeast India and some parts of China and Japan.[40] Paat silk also known as Mulberry silk comes from silkworm *Bombyx textor*, which feeds on mulberry leaves.[41]

Table 3.1. Types of masks used in the current study[a]

A	B	C	D
			
Cloth 1	Cloth 2	Muga Silk	Eri Silk
2 layers/3 layers	2 layers/3 layers	2 layers/3 layers	2 layers/3 layers
Hydrophilic[7]	Hydrophobic	Hydrophobic[16]	Hydrophilic[15]
E	**F**	**G**	**---**
			,,
Paat Silk	Surgical	N95	Super-hydrophobic
2 layers/3 layers	3 layers	5 layers filtration membrane technology	??
Hydrophilic[13]	Hydrophobic[8]	Hydrophobic[5]	

[a]The superscripts in the last column denotes references

3.2.2. Materials

Human mucus[42] is more viscous than water. To mimic the viscosity of mucus, 60% v/v glycerol solution was used to carry out the experiments. For clear detection of the droplets absorbed on the fabric that constitutes the mask, fluorescein sodium salt (dissolved in the solution mentioned above) was used as a marker. After adding the marker, droplets were clearly visible under fluorescence microscopy.

3.2.3. Experimental setup

All the experiments were carried out in a closed cuboidal chamber of approximate dimensions 30 cm x 16 cm x 15 cm. Two 4 cm x 4 cm windows were cut out on the opposite faces with respect to the box's length. On one window, a mask fabric was fixed with the outer side of the mask fabric facing the inside of the box. On the opposite, a spray bottle was placed containing the glycerol solution as shown in Figure 3.1. After placing the sample, the spray bottle was pressed twice, and then the sample was observed under the fluorescence microscope.

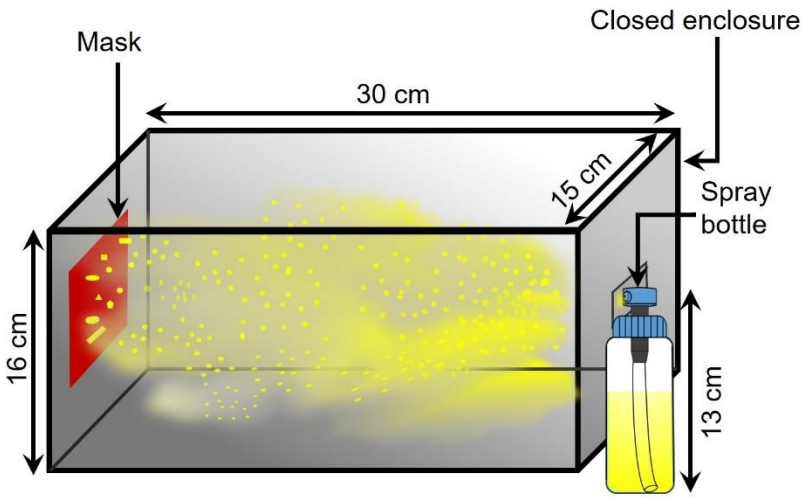

Figure 3.1. Schematic showing the experimental setup of a cuboidal enclosure of length ~30 cm that had a mask on one end and an opening for spraying from the other end.

3.2.4. Preparation of octadecyltrichlorosilane (OTS) solution

OTS is used extensively as a surface-modifying chemical because of its fluorine-free composition, which makes it both nonhazardous to the health and the environment.[43,44] The OTS solution was prepared by mixing 20 μL of octadecyltrichlorosilane (OTS) in 10 mL of toluene.[45]

The mixer solution was stirred for 10 min and then was heated on a hot plate at 60 ºC for 30 min. After that, the solution was cooled to room temperature for some time before being used for further experiment.

3.2.5. Preparation of hydrophobic Eri silk

The procured Eri silk fabric was first washed with detergent to remove the excess dirt or oil present in it and then dried naturally under the sun. The dried silk pieces were first washed with acetone for 1 min to remove any excess detergent stuck to the fabric. Subsequently, they were washed in DI water for 2 min to remove the acetone. First, it was dried with nitrogen gas to remove the excess water. Once the cloth pieces become moist, they were dried in a hot-air oven at around 100 ºC for 10 min to make it complete drying. After that, UV-ozone treatment was done for 2 min in the UV-ozone chamber (Novascan Technologies, Model: PSD UV4) and the fabric was immediately transferred to the OTS solution[45] prepared (several pieces of them). After keeping the cloth pieces in the solution for 30 min, they were washed with toluene to remove the excess OTS present on the fiber. Then, the pieces were dried with nitrogen and finally kept in a hot-air oven at 100 ºC for 10 min. The plausible chemical reaction of OTS with the fabric (Figure 3.2) showed that the Si molecules of OTS formed chemical bond with the -OH groups of the fabric and the long hydrocarbon chains of the OTS dangled outside in the air. The dangled hydrocarbon chains are not harmful, and thus the OTS-treated silk masks are safer for human use.

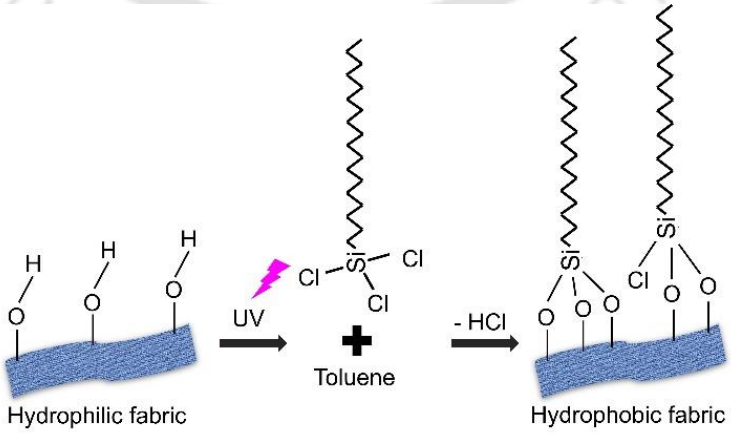

Figure 3.2. The figure shows the plusible chemical reaction undergoing during modification of hydrophilic to hydrophobic Eri Silk fabric using octadecyltrichlorosilane (OTS).

3.2.6. Characterization of hydrophobic Eri silk

Typically, 2 nm – 3 nm[46] OTS layer is known to form on the surface of Si, which may well be the case here that rendered the silk hydrophobic (Sample D1). The thickness of the deposited OTS layer was measured with Ellipsometer. As laser light interacts with cloth fabric, thickness measurement on cloth was not feasible. Moreover, the conformal topography formed by the thin layer of coated OTS over the textured silk fabric made the ellipsometric measurements difficult over the cloth.[47] Instead, cleaned silicon wafer was ozone-treated for 30 min followed by a 30 min of OTS treatment and then measured with an Ellipsometer for thickness as an alternative. The thickness of the OTS layer was measured to be 1.9 ± 0.1 nm with a root mean square error (RMSE) of 0.585.

Ellipsometer operating data

Ellipsometry (EP3 Nanofilm, Accurion, Germany) was performed to find the thickness of the OTS film on Silicon wafer. The angle of incidence (AOI) and angle of reflectance were taken as 70^{0}. The wavelength selection of the laser was 658 nm. In ellipsometric measurements the main concept is to find the minimum intensity in a Region of Interest (ROI) by rotating the polarizer and analyzer. So, we followed four zone approach for 3 ROIs, which gave the minimum signal for four zones by rotating the polarizer and analyzer. Next a three layer model was designed with material Si- Crystalline Silicon (100 orientation) at the bottom followed by SiO_2 layer and Material_1 i.e. silane on top. The ambient condition surrounding the sample was taken as Air. In order to fit the data, for Material_1 Cauchy dispersion function was selected and the values taken were: A_n: 1.48, B_n: 2273 nm^2, C_n: 1.674E+8 nm^4, A_k: 0.176, B_k: 846 nm^2, C_k: 1.233E+8 nm^4.

The coating of the silk by OTS was confirmed by Fourier transform infrared (FTIR) spectroscopy with characteristic peaks of the compound being present in the spectrum as shown in Figure 3.3. For treated Eri silk, the peaks at 2845 and 2918 cm^{-1} are for asymmetric and symmetric stretching of CH_2 bond due to n-octadecyl hydrocarbon chain.[48,49] Additionally, the

peak at 1445 cm^{-1} is due to Si-C bond vibration, and 1026 cm^{-1} corresponds to Si-O-Si asymmetric and symmetric bond vibrations.[48] For the untreated Eri silk, the peaks at 1227 cm^{-1}, 1535 cm^{-1}, and 1635 cm^{-1} correspond to amide III, amide II, and amide I absorption bands, respectively.[15] The FTIR data were supported by the presence of the Si on the treated Eri silk captured in the EDS analysis (Figure 3.4).

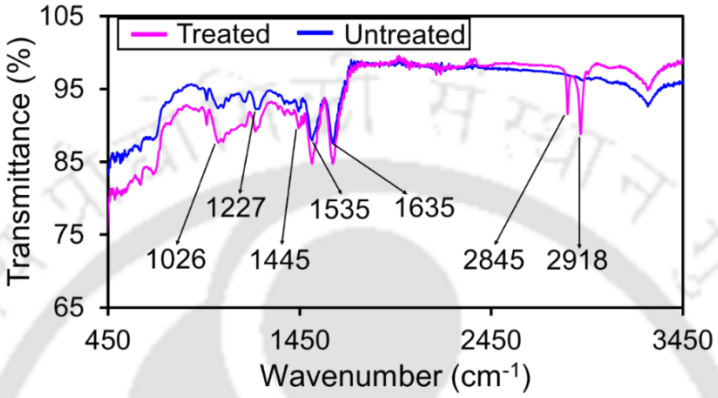

Figure 3.3. FTIR-ATR spectra of as-purchased and treated Eri silk fabrics.

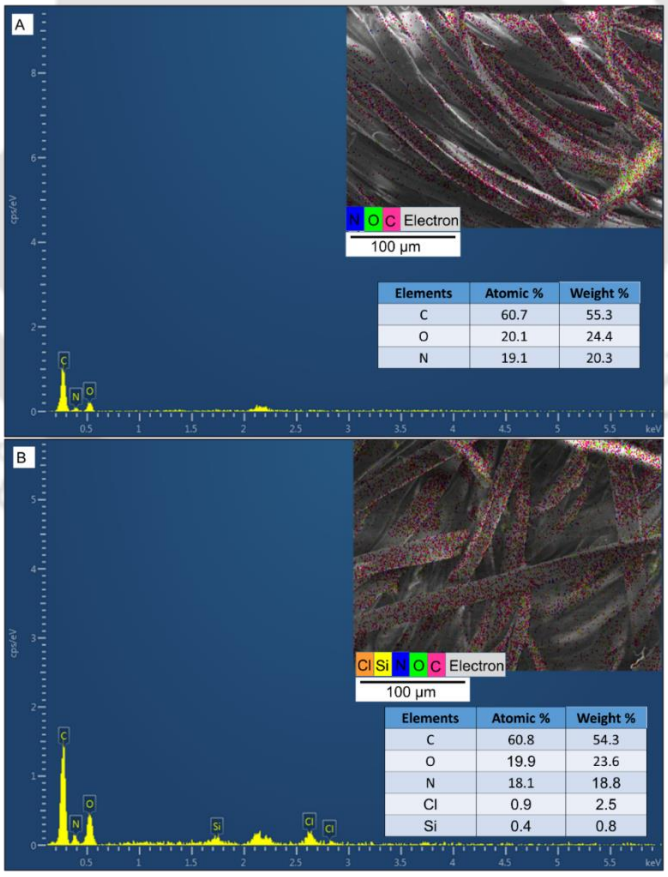

Figure 3.4. FESEM-EDS graphs showing distribution of different elements for, A: as-purchased Eri silk, B: OTS treated Eri silk. Inset shows the elemental mapping and the atomic % and weight % of different elements present on the fabric.

The hydrophobicity of the treated Eri silk was maintained even after three times washing with detergent. At room temperature, the samples were dipped inside commercially available laundry detergent solution and, at the same time, the fabric surface was rubbed six times with fingers inside the detergent solution. The fabric was again cleaned with only water to remove the detergent and dried first with N_2 gas followed by heating on a hot plate at around 80 ^{o}C for 5 min. After washing and drying, the water droplets falling on the treated Eri silk were seen to be rolling away as before from the surface without wetting the silk.

3.2.7. Quantitative analysis

All images from the fluorescence microscope (Carl Zeiss, Model A1MAT HAL 100) were analyzed in an open-source software "ImageJ" for measurement of the area covered by the droplets on the surface of the mask. The quantitative measurements were done in "Microsoft Excel" and "Origin." In "ImageJ" software, we can adjust the image with threshold function and then analyze and measure the area of the image with ROI Manager function. In "Origin" software with the frequency count function, we can find the normalized probability distribution of the pore area of the mask. The contact angle measurements for all the samples were done immediately with the help of the contact angle goniometer (Holmarc Opto-Mechatronics, Model: HO-IAD-CAM-01B) after disposing a 2 μL DI water droplet on the fabric surface. To have better clarity about the spatial arrangement of the fibers on all masks, field emission scanning electron microscopy (FESEM) (JSM 7610 F, JEOL, Japan) was also performed. EDS analysis of the treated and pristine Eri silk was performed using FESEM with an EDS detector (Zeiss, Model: Sigma 300).

3.3. Results and Discussion

3.3.1. *Hydrophobicity and Liquid Absorption Capacity of Mask Fabrics*

Our central aim has been to study the behavior of different types of masks when sprayed from a distance with model aerosol. The types of masks and their nomenclature used in this work is presented in Table 3.1. A first impression about the effectiveness of a mask against an incoming aerosol can be made from the fractional area coverage on the outer layer of the mask upon impact.

We pursued this by placing the mask cloth sample (4 cm x 4 cm) at one end of an enclosed chamber, 30 cm away from the other end having an opening for a spray bottle that sprayed aerosol (Figure 3.1). The chamber was maintained at 23 ± 2 °C and a relative humidity of ~ 58 ± 2%. The liquid used was a fluorescein salt solution in 60% (v/v) aqueous glycerol. The air-dried fabric was viewed under a fluorescence microscope and then the fractional area coverage of the deposited dye was calculated using the open-source software ImageJ. A plot of correlation between the fractional coverage of the absorbed dye with the hydrophobicity of the mask fabric is shown in Figure 3.5a. The hydrophobicity of the mask fabric was measured based on the contact angle of water on the fabric. It was observed that the hydrophobic mask fabric (with a higher water contact angle) had lower fractional coverage of the dye in comparison to hydrophilic mask fabric (having a lower contact angle). For example, the water contact angle for N95 mask fabric (sample G) was ~ 127.4° ± 3.39 and the fractional coverage for the same was ~ 6% ± 0.028. On the other hand, cotton cloth 1 sample (sample A) with a water contact angle of ~ 66.7° ± 3.71 had a fractional coverage of ~ 56% ± 0.098. As is clear from the figure 3.5a, the water contact angles and fractional dye coverage for all other mask fabrics were measured to have values in between the above ranges (as applicable).

Importantly, the as-purchased Eri silk fabric had a water contact angle of 85.4° ± 2.4 and also had a high dye fractional coverage area of 50% ± 0.133. The OTS-treated Eri silk, on the other hand, exhibited excellent hydrophobic properties with a water contact angle of 143.7° ± 1.13 and fractional area coverage of only 14.6% ± 0.032, which is better than most of the masks reported here (Table 3.2). The OTS-treated cotton cloth 1 (sample A) also displayed hydrophobic characteristics with a water contact angle of 140.4° as shown in Figure 3.6. Silk fabric mainly consists of fibroin and sericin (protein)[50] and a small amount of fats and minerals. Whereas, cotton mainly consists of cellulose (carbohydrate)[51] and a small amount of protein, fats, and minerals. But both cotton and silk have -OH groups on the fabric which helps in the easy attachment of Si

molecules of OTS. This helps in forming a self-assembled monolayer above the fabric surface, which is the real reason behind the hydrophobic characteristics.

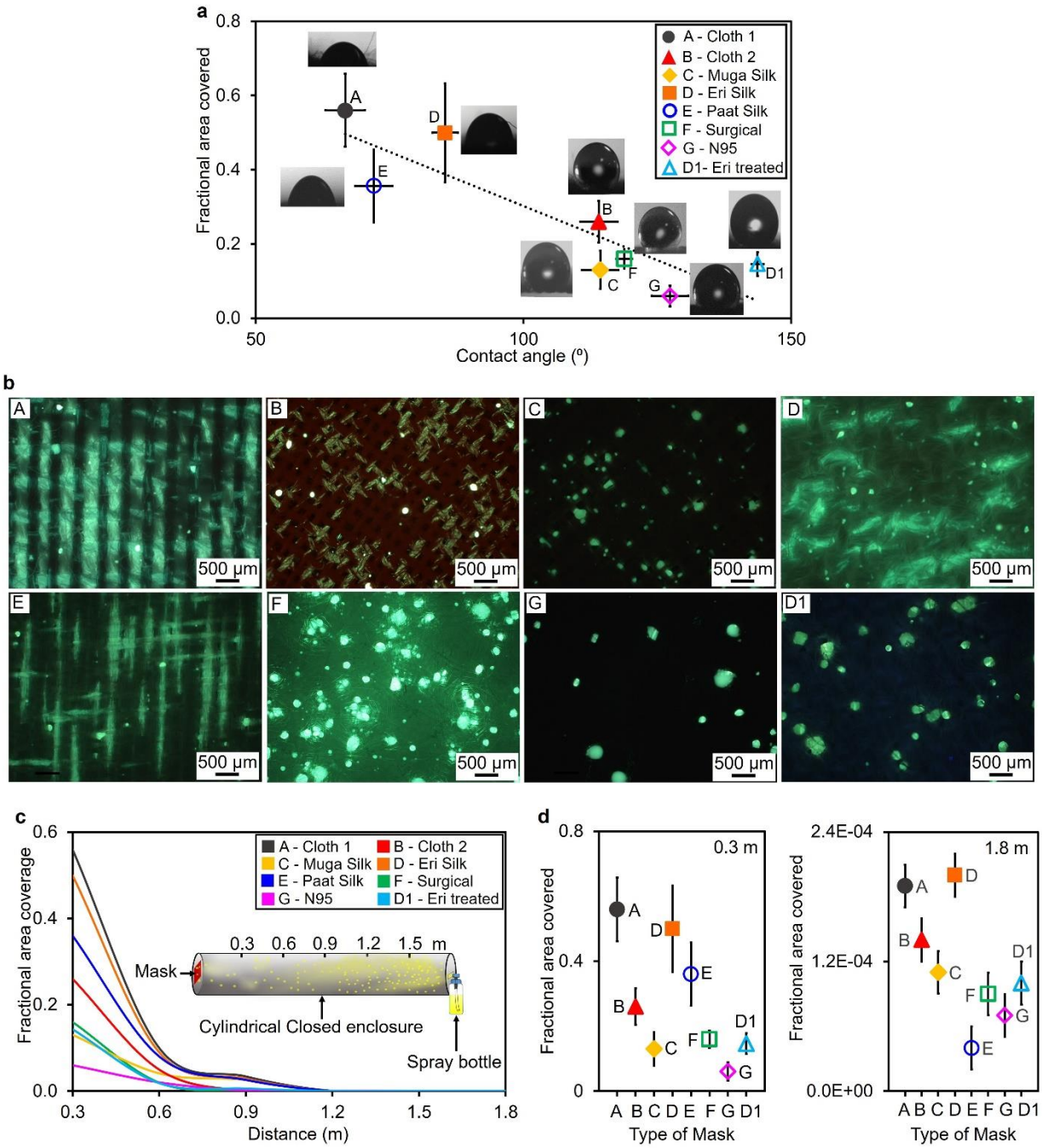

Figure 3.5. Fractional area covered on masks. (a) Graph depicting the fractional area coverage of the absorbed dye after drying of the deposited droplets as a function of the contact angle of water on the mask materials. The black dotted line is the linearly-fitted curve. Insets close to each point show the optical images of the water droplet on the mask surface (b) Typical fluorescence micrograph of the mask sample after spraying of two puffs from a spray bottle kept at 30 cm away in an enclosure shown in the experimental setup, A: Cloth 1, B: Cloth 2, C: Muga Silk, D: Eri Silk, E: Paat Silk, F: Surgical, G: N95, D1: Treated Eri silk. (c) Graph showing the fractional area covered for different types of masks at different distances ranging from 0.3 m to 1.8 m. Inset shows the experimental set-up of a long cylindrical closed space of length 1.8 m with a diameter

of 0.1 m. and (d) Comparative graphs showing the sharp decline in fractional area coverage at distances 0.3 m and 1.8 m, respectively. Corresponding data are provided in Table 3.4.

Table 3.2. This table shows the fractional area coverage of the absorbed dye after drying of the deposited droplets as a function of the contact angle of water on the mask materials

Mask	Contact Angle	Fractional area covered
Cloth 1	66.70 ± 3.71	56 ± 0.098
Cloth 2	114.06 ± 3.50	26 ± 0.056
Muga	114.33 ± 3.41	13 ± 0.051
Eri	85.35 ± 2.40	50 ± 0.133
Paat	72.05 ± 3.45	35.6 ± 0.098
Surgical	118.80 ± 1.46	16 ± 0.026
N95	127.37 ± 3.39	6 ± 0.028
Eri treated	143.72 ± 1.13	14.6 ± 0.032

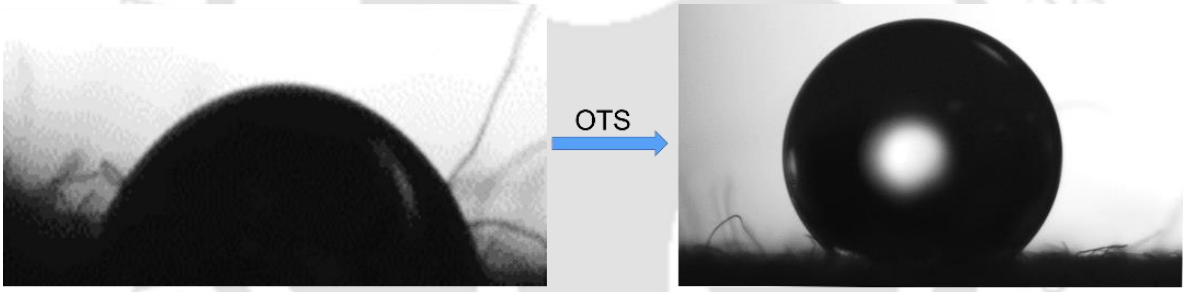

Figure 3.6. The figure on the left shows the contact angle made by water on as-purchased cotton cloth 1 fabric (Sample A) which is 66.7°. After OTS treatment the fabric turned hydrophobic (right) having contact angle made by water as 140.4°.

Table 3.3. This table shows the fractional area coverage of the absorbed dye after drying of the deposited droplets at distances 0.3 m, 0.6 m, 0.9 m, 1.2 m, 1.5 m and 1.8 m

Mask	Fraction covered at 0.3 m	Fraction covered at 0.6 m	Fraction covered at 0.9 m	Fraction covered at 1.2 m	Fraction covered at 1.5 m	Fraction covered at 1.8 m
Cloth 1	0.56	0.100	0.0340	0.00052	0.00020	0.00019
Cloth 2	0.26	0.050	0.0010	0.00047	0.00010	0.00014
Muga	0.13	0.041	0.0260	0.00053	0.00026	0.00011
Eri	0.50	0.090	0.0290	0.00037	0.00045	0.00020
Paat	0.36	0.080	0.0256	0.00014	0.00014	0.00004
Surgical	0.16	0.019	0.0009	0.00009	0.00009	0.00009
N95	0.06	0.020	0.0009	0.00063	0.00024	0.00007
Eri treated	0.14	0.018	0.0059	0.00025	0.00020	0.00010

Fluorescence microscopic images for the area coverage of absorbed dye after drying on different types of masks are shown in Figure 3.5b. These fluorescence microscopy images for all samples also showed that the area covered by the sprayed droplets on sample G is the least followed by D1 and D. The results clearly indicated that by modifying the hydrophobicity of mask material or fabric, it was possible to have superior performance against aerosol. Thus, an affordable mask can be chemically tailored to have better protection against viral infection that spreads through aerosol.

An important parameter that determines the plausibility of viral infection is the physical distance of separation of the recipient from the source. In other words, it is important to understand the profiles of the impression of aerosol droplets that contain a chosen molecule (as a model for pathogen) on the mask fabric as a function of the distance of separation from the source. To emulate the profile, we fabricated a cylindrical tunnel, with a spray bottle at one end (source of droplets) and a test mask sample fabric fitted at a particular distance (0.3 m-1.8 m) from the source.

Table 3.4. This table shows the percentage decrease in area covered by droplets on a mask when sprayed from a distance of 1.8 m with reference to that from 0.3 m

Mask	Fraction covered at 0.3 m	Fraction covered at 1.8 m	Difference	Percentage decrease in area covered
Cloth 1	0.56	0.00019	0.5598	99.966
Cloth 2	0.26	0.00014	0.2599	99.946
Muga	0.13	0.00011	0.1298	99.915
Eri	0.50	0.0002	0.4997	99.960
Paat	0.36	0.00004	0.3564	99.989
Surgical	0.16	0.00009	0.1599	99.944
N95	0.06	0.00007	0.0599	99.883
Eri treated	0.143	0.00010	0.1429	99.930

The fractional area coverage versus distance for all the samples are plotted in Figure 3.5c and is also presented in Table 3.3. Further, as is clear from the figure, the fractional area coverage decreased quickly from a distance of 0.3 m-0.6 m for all the fabrics. At 0.3 m of distance, the fractional coverage (Figure 3.5c) was high for Cloth 1 (56%), and Eri silk (50%) fabrics; whereas it was moderate for Paat silk (36%) and Cloth 2 (26%). On the other hand, the coverage was low for OTS-treated Eri silk (14.6%), muga silk (13%), surgical mask (16%), and N95 mask (6%). The

results indicated that the more hydrophobic the fabric was, the less fractional area coverage for the deposited dye was at 0.3 m. Importantly, as shown in Figure 3.5d, at 1.8 m, the fractional area coverage for all samples was reduced by 99.9% with respect to the fractional area coverage at 0.3 m. Moreover, trends in coverage were similar for both at 0.3 m and 1.8 m. In view of the above, we subsequently focused on characteristics at 0.3 m distance between the source and the sample mask fabric.

3.3.2. Droplet size and porosity of mask

To estimate the droplet size distribution at a particular distance, an experimental set-up consisting of a high-speed camera (Phantom VEO 640L, 512 x 512 resolution, 300 fps), which can capture the droplets illuminated with a laser sheet was used (Figure 3.7a). The droplets were sprayed from a bottle placed at different distances from the laser sheet. A laser beam that came out of a laser source (RayPower 450, Dantec Dynamics) was converted to a laser sheet with the help of a cylindrical lens. The droplet images thus captured were then analyzed with an open-source software ImageJ, and the distribution of the droplet size was constructed from 3000 data points extracted from three individual files of the recorded images using Origin software.

The microscopic images in the transmittance mode revealed that the materials for the cloth masks (sample A, B), and the silk masks (sample C, D, E) (Figure 3.7b) have been interwoven to form rectangular pore arrangements of different sizes. Sample C has the largest pore size of around 72 500 μm^2. Sample F and G are the non-woven surgical and N95 masks, respectively, having relatively small, irregularly shaped pores compared to samples B, C, D, and E (Figure 3.7b). The pore size distribution of sample - A was comparable to that of N95 (sample G) where the maximum pore size overserved was 8250 μm^2 (Figure 3.7c). It has been inferred from Figure 3.7c that sample G would be the best in terms of protection, as most of the smaller size droplets (distribution of which is denoted by black dotted line), which came onto the surface of the N95 mask were less likely to pass through it. This is because the maximum pore size, as well as the density of the pores of any particular size on this mask, was smaller compared to the density of

the droplets of that particular size. Similarly, cloth 1 (sample A) was also expected to have better performance in terms of droplet penetration. However, due to the high liquid absorption capacity, the use of this mask may not be advisable.

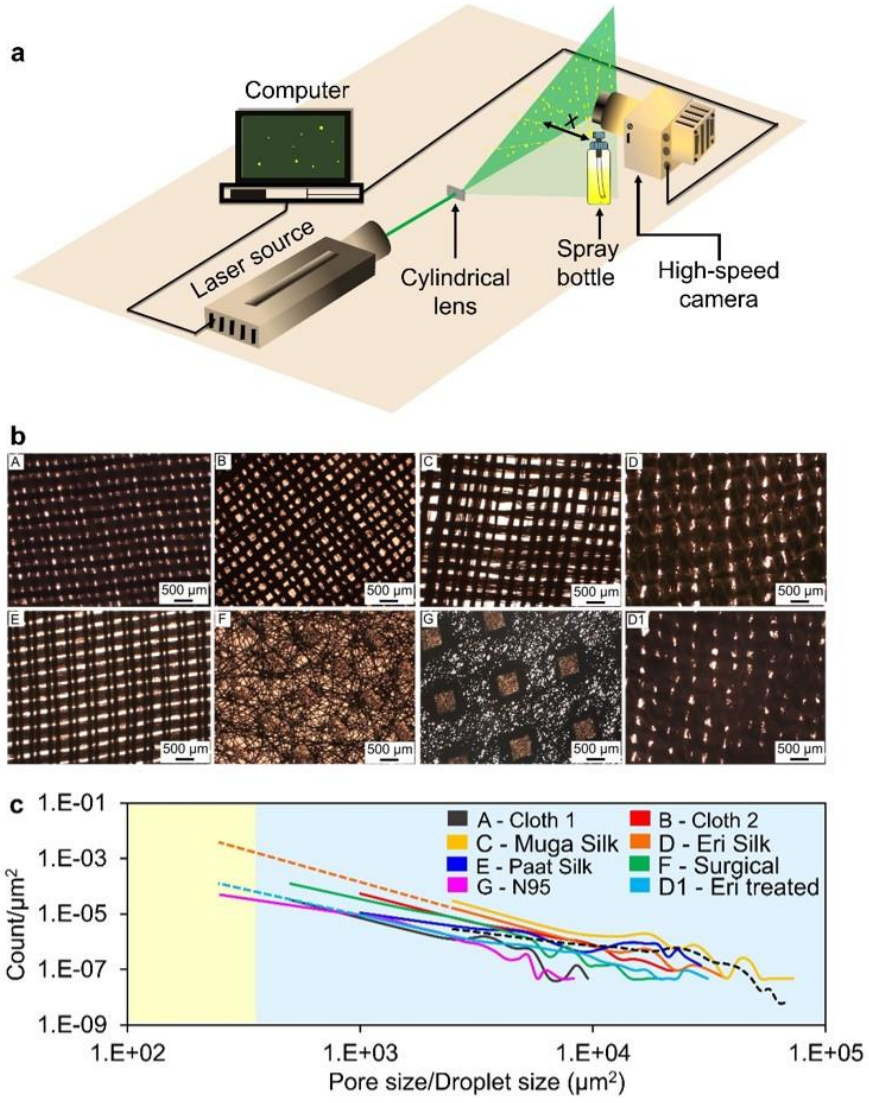

Figure 3.7. (a) Experimental set-up showing the method used for measuring the droplet size spread after spraying from a bottle. A laser sheet is used to illuminate the droplets and the image was recorded with a high-speed camera (Phantom VEO 640L) at 300 fps. Here, "*x*" is the distance between the spray nozzle and the laser sheet. The values of *x* were 5, 10, and 15 cm. (b) Transmission optical micrograph of the pore sizes of the first layer of the mask materials: the sample names indicated in the images correspond to those mentioned in Table 3.1. Corresponding FESEM images are provided in Figure 3.8. (c) Graph showing the pore size distribution of all types of masks. The black dotted line is the droplet size distribution plot for the value of x = 10 cm. Similar data with droplet size distribution for the value of x = 5 cm and 15 cm are presented in the Appendix A.3.1.

On the other hand, Mask C (Muga silk) has a considerable number of larger pores (with the largest pore size observed being 72500 μm^2) with respect to the small droplets hitting the

surface (Figure 3.7c). This would lead to a significant amount of droplet penetration through the mask layer. After the treatment with OTS, the largest pore size of sample D1 was reduced by some extent to 31 000 μm^2 compared to unmodified sample D with 37 500 μm^2 (Figure 3.7c). The reduction in pore size for sample D1 would block smaller droplets more in numbers coming towards it than sample D. The pore size distribution of D1 revealed that after OTS treatment, the mask prevented relatively larger droplets from penetration that was similar to that of a surgical mask and also was better than a surgical mask for small size droplets. Next, we will focus our discussion on OTS-treated mask (D1) and its behavior with droplet impact and its breathability compared to the untreated mask (D).

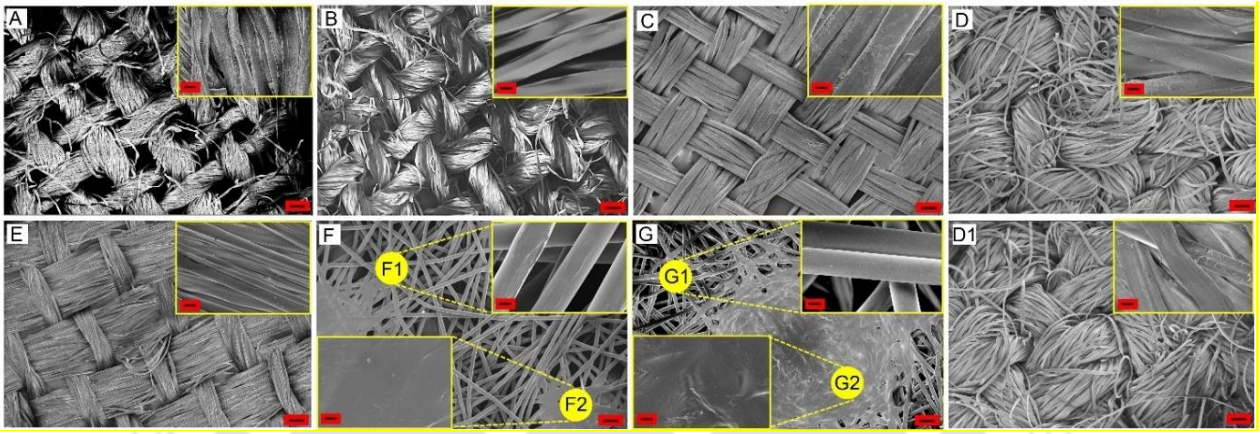

Figure 3.8. FESEM images showing the pores of mask surface. A: Cloth 1, B: Cloth 2, C: Muga Silk, D: Eri Silk, E: Paat Silk, F: Surgical Mask, G: N95, D1: Treated Eri silk. The scale bars (shown on right side of the images) for all the images represent 100 μm. The scale bar of the inset images (shown on left side of the images) represent 10 μm. F1 and G1 shows the zoomed in images for the fibres. F2 and G2 shows the zoomed in images for the solid patches present in between the fibres.

The spherical SARS-CoV-2 viruses with spikes are usually 120 nm in diameter.[52] Droplets ranging from 1 to 200 μm in diameter are considered to be airborne.[53] The viruses aggregated into clusters are cited to be potentially transmitted via droplets of diameter 20 μm.[54] Taking this as an instance, from Figure 3.7c, we could clearly see that N95 mask was very efficient in blocking these model droplets. As this mask has smaller counts for pore size in the range of 200 - 400 μm^2, it could typically block droplets having an area of approximately 400 μm^2. Although the largest pore size available in N95 was noticed as 8250 μm^2, a minimal amount of smaller-sized droplets would

definitely pass through the meshes. Similarly, when sample D and D1 were extrapolated (represented by orange and blue dotted lines respectively in Figure 3.7c), D1 was seen to have a smaller pore size compared to D and almost comparable to N95 in performance in resisting deposition and/or penetration of such model droplets.

3.3.3 Droplet impact on a treated mask

An experiment was carried out to examine the impact behavior of a 10 μL aqueous glycerol (60 %) droplet when dropped from a height of ~33 cm (emulating high impact) and ~5 cm (emulating low impact) on an unmodified Eri silk and OTS-treated hydrophobic Eri silk. A single layer of the test silk sample was tightly clamped to a custom-made holder and kept at an inclination of 15° to the horizontal axis. The experimental setup is shown in the inset of Figure 3.9a. To detect whether the liquid was absorbed by the fabric or not, the fluorescein Na salt dye was mixed with the aqueous glycerol and used for this experiment. A high-speed camera (Phantom VEO E-340L model, 5600 fps, 1024x 500 resolution) was used to capture the impact events. Interestingly, for the high-impact experiments, the droplet falling on the unmodified silk sieved through the fabric in 9 ms. On the other hand, for the OTS-treated hydrophobic Eri silk, the droplet did not pass through the fabric. Due to the high impact, the parent droplet after hitting the treated silk first fragmented into smaller daughter droplets and the remaining parent droplet adhered to the surface of the fabric, which oscillated on the surface with diminishing amplitude, and eventually evaporated after a long time (50 min) leaving a trace of the dye on the front surface of the fabric only (as shown in Figure 3.10). The trajectory of the apex of the falling parent droplet was tracked and is shown in Figure 3.9a. The liquid dye did not get absorbed by the fabric, which was apparent from the cleanliness of the backside of the fabric (Figure 3.9) at the end of the experiment. On the other hand, the unmodified Eri silk completely soaked the dye droplet and both the front and backside of the fabric became yellow spanning over the large area (Figure 3.9e).

A similar experiment with a droplet falling from a height of ~5 cm (low impact) showed that the droplet was stuck on the untreated surface with diminishing oscillation. The trajectory of

the apex of the falling droplet was tracked and is depicted by the blue line in Figure 3.9b. The droplet was stuck into a low-energy "Cassie impregnated Wenzel state"[55,56] due to the impact on the micro projections and secondary micro/nanofolds on the fabric surface. The droplet initially wetted the large micro pits, but as the water could not penetrate further into the smaller micro/

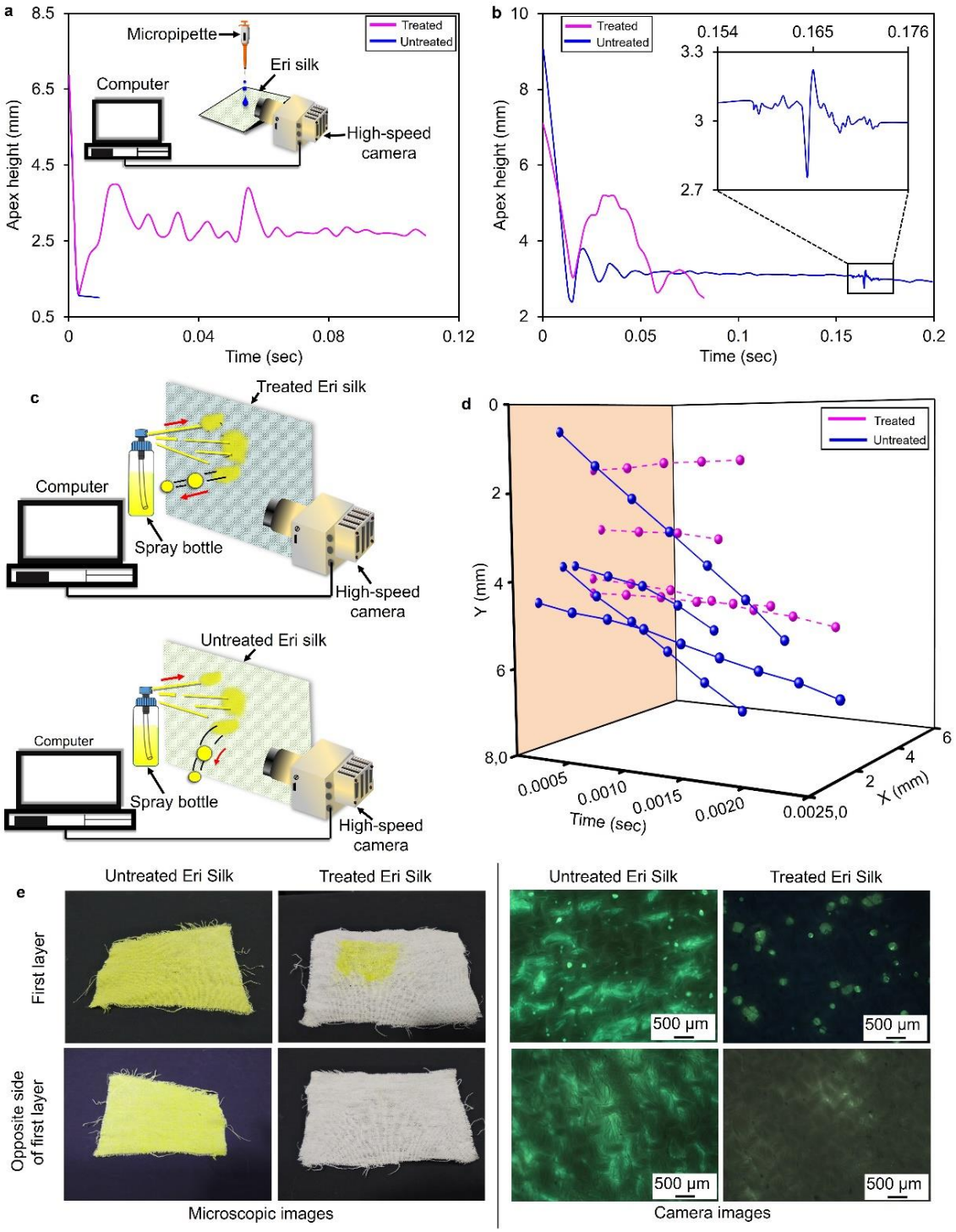

Figure 3.9. Droplet behavior on treated and untreated Eri silk mask. (a) The behavior of a 10 µL droplet when it was dropped on a slanted silk surface from a height of 33 cm (high impact). The

angle of the slope was 15^0 to the horizontal axis. The inset shows the experimental setup for the same. The plot shows the droplet apex height trail with time on as-purchased (blue line) and OTS-treated (pink line) Eri silk fabric surfaces, respectively. (b) Results from the experiment similar to that in (a), but the droplet fell from a relatively shorter height of 5 cm (low impact) on as-purchased (blue line) and OTS-treated (pink line) Eri silk fabric surfaces, respectively. The inset graph shows the behavior when the droplet had transformed from Cassie-impregnated Wenzel state to Wenzel state on the as-purchased Eri silk fabric surface (see text for details). (c) Experimental setup to capture the droplets bouncing back from vertically placed treated (top) and as-purchased (bottom) Eri silk upon spraying from 5 cm distance. The droplets bouncing back from treated Eri silk initially traveled faster in a straighter path, whereas the as-purchased Eri silk followed a curved downward path due to the lower velocity experienced by the droplets. (d) Plot showing the trajectories of typical droplets bouncing back from the vertically placed as-purchased (blue) and OTS-treated (pink) Eri silk fabric as shown in (c) after hitting the surface. (e) Optical and fluorescence microscopic images of both as-purchased and OTS-treated Eri silk cloth pieces (front surface and back surface) after spraying with the liquid dye as depicted in (c).

nanofolds, it created small air pockets. These air pockets helped to retain the droplet into the Cassie impregnated Wenzel state for some time. The droplet oscillation at this state completely diminishes after ~70 ms, and at ~150 ms, the droplet transited to the relatively lower-energy "Wenzel" state associated with the fluctuation of the droplet again (see fluctuation at the inset of Figure 3.9b).

Importantly, on the treated hydrophobic silk surface, upon impact, droplets bounced back to the air completely and eventually rolled down the surface without leaving any trace of the liquid or dye. The trajectory of the drop apex is shown by the pink line in Figure 3.9b. To emulate a more realistic scenario of the mask-droplet interaction, the dyed liquid was sprayed on a vertically placed unmodified and treated Eri silk surface from a distance of ~5 cm. The schematic of this experiment is shown in Figure 3.9c. The droplet bouncing velocities from such surfaces was estimated from the trajectories tracked with the high-speed camera (at 3200 fps) (Figure 3.9d). It was found that most of the droplets bounced back with a high average horizontal velocity (~ 702.6 mm/s) from the treated hydrophobic surface. However, from the untreated hydrophilic Eri silk, the droplet bounced back with average horizontal velocity (~ 247.0 mm/s) that was much lower than the same from the hydrophobic surface and with a relatively faster downward fall (Figure 3.9d). It was also noticed that fewer droplets bounced back from the untreated Eri silk in the initial period than the treated Eri silk. While spraying, a continuous liquid film started forming on the

untreated surface from 4 s onwards due to which the droplets collided with the liquid film and splashed out as droplets of different sizes. However, hydrophobicity of treated Eri silk resulted in no liquid film formation during the initial period of spraying.

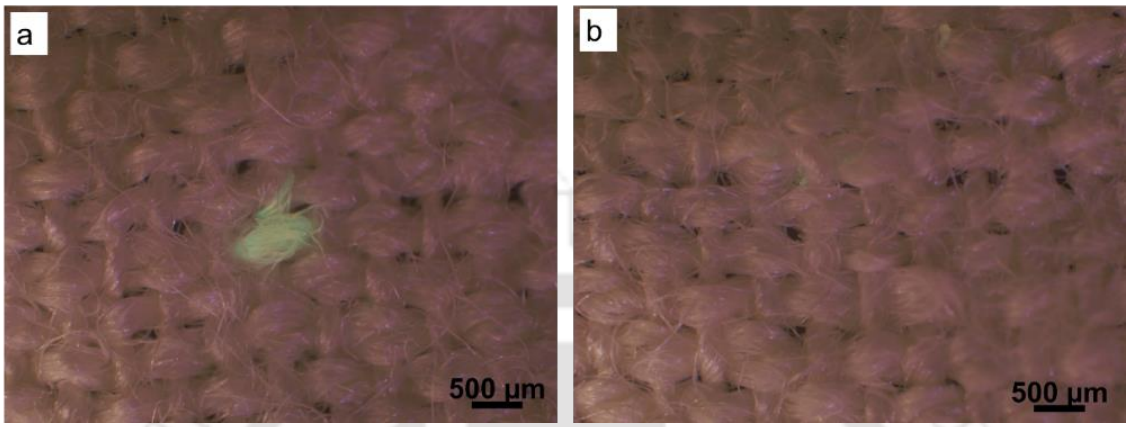

Figure 3.10. (a) Fluorescence images showing the front side of the fabric where a trace of dye was left behind after complete evaporation of the droplet, due to high impact of the falling droplet on treated Eri silk fabric, (b) The clean back side of the same fabric verifies that the droplet was not soaked by the fabric.

Optical images and fluorescence microscope images of the unmodified and treated Eri silk showed (Figure 3.9e) that the dye was absorbed completely by the threads of the untreated Eri silk, whereas only the front surface of the hydrophobic Eri silk demonstrated a minimum deposition of the dye from the evaporated liquid.

3.3.4. The breathability of the treated mask

To check the breathability of three-layered mask materials, we checked oxygen permeability through them. The sample fabric (as purchased Eri silk, treated hydrophobic Eri silk, and N95) was first wrapped on the open mouth of a cylindrical enclosure having a sealed rubber stopper at the side of the cylinder. In each experiment, three layers of the test fabric sample were used. A balloon filled with ~ 0.5 L of oxygen at room temperature (23 °C) and pressure (1 atm) was tightly tied to the open mouth of the cylinder having the fabric sample to avoid any leakage of oxygen.

When the tie was opened, the oxygen permeated through the fabric sample and gradually increased the oxygen concentration inside the cylinder. The gas was collected from the cylinder

through the sealed rubber stopper using a syringe (Figure 3.11d), and gas chromatography (GC) was used to estimate the concentration of the oxygen inside the cylinder. The gas was collected from the cylinder immediately after opening the balloon (dashed lines in Figure 3.11a-c) and after 2 min of opening the balloon (solid lines in Figure 3.11a-c). The GC curves, shown in Figure 3.11a-c, have values presented after subtraction of the background oxygen that was present before the opening of the balloon.

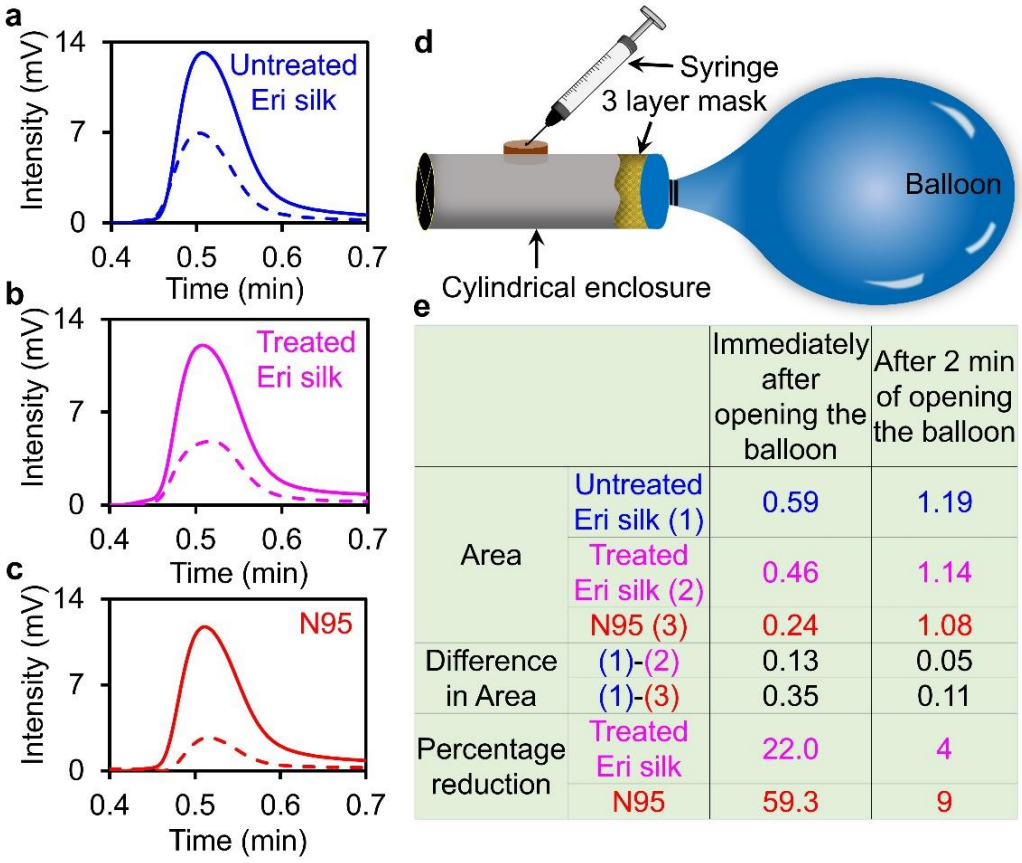

		Immediately after opening the balloon	After 2 min of opening the balloon
Area	Untreated Eri silk (1)	0.59	1.19
	Treated Eri silk (2)	0.46	1.14
	N95 (3)	0.24	1.08
Difference in Area	(1)-(2)	0.13	0.05
	(1)-(3)	0.35	0.11
Percentage reduction	Treated Eri silk	22.0	4
	N95	59.3	9

Figure 3.11. The breathability of N95, as-purchased and treated Eri silk masks. Graphs showing the gas chromatography (GC) peak of oxygen after passing through the three layers of mask materials: for a) As-purchased Eri silk, b) OTS-treated Eri silk, and c) N95 mask fabrics. Dashed and solid lines show the oxygen peaks immediately after the opening of the oxygen-containing balloon and after 2 min of opening, respectively. The time on the *x*-axis is the residence time for the detection of oxygen by the GC machine. d) Experimental setup showing how oxygen was collected from a cylindrical enclosure for gas chromatographic detection. e) Table shows the area under the curve for the plots in (a-c) depicting the permeability (breathability) of oxygen through the three-layered masks and percentage reduction of the breathability with respect to the as-purchased Eri silk mask fabric.

The results shown in tabular form Figure 3.11e revealed that immediate breathability (i.e., immediately following the opening of the oxygen source) of the Eri silk was maximum and that

was reduced by ~ 22 % after OTS treatment. However, compared to untreated Eri silk the breathability of N95 was much less (~ 59 %). For longer duration breathability (after 2 min of the opening of oxygen source), these reductions for treated Eri silk and N95 were ~4 % and ~9 %, respectively. Nevertheless, immediate breathability should be the primary concern while choosing an appropriate mask material. Here, the comparison was performed based on untreated, as-purchased Eri silk mask as among these samples, as Eri silk mask (both OTS-treated and as-purchased fabrics) have been the most comfortable and easy to breathe through it.

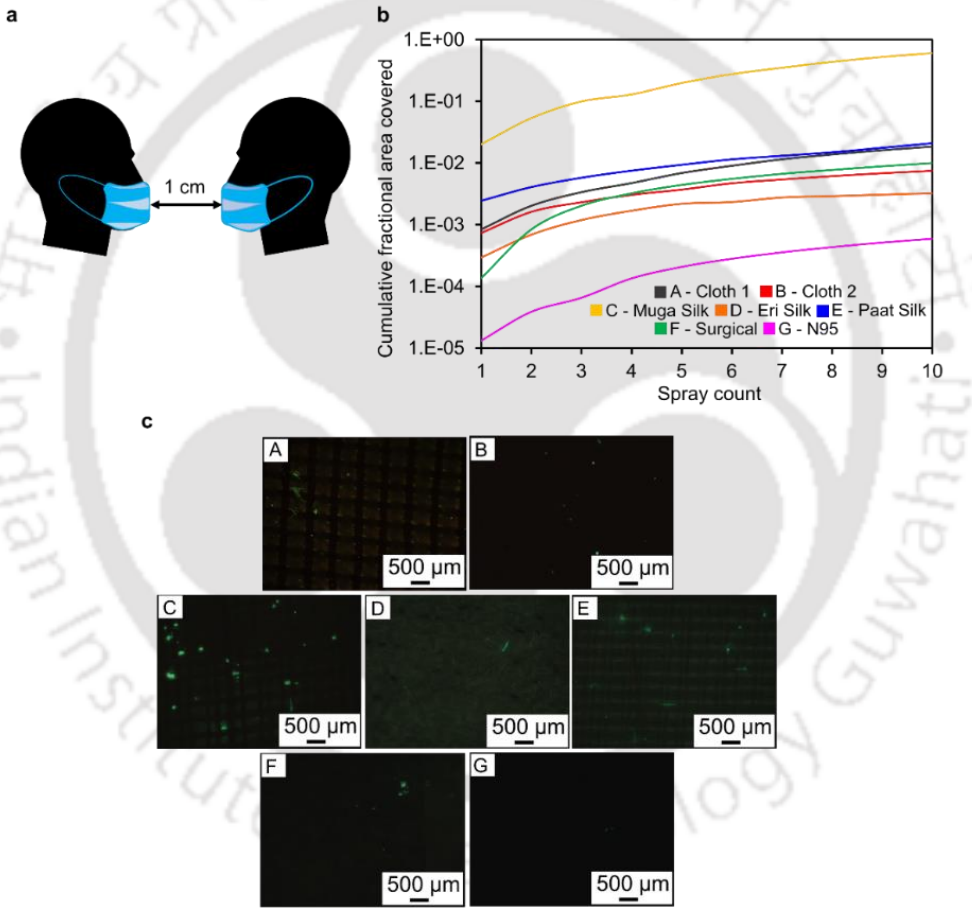

Figure 3.12. (a) Schematic showing the arrangement of placing two masks in proximity. (b) Cumulative fractional area covered on the same mask placed 1 cm apart from another mask of the same type for each spray count (1-10) while checking the penetration and soaking capacity of the mask. (c) Fluorescence microscopic images of the mask, which was placed 1 cm apart from another mask of the same type for the 10th spray while checking the penetration and soaking capacity of the mask. A: Cloth 1, B: Cloth 2, C: Muga Silk, D: Eri Silk, E: Paat Silk, F: Surgical Mask, G: N95.

Another important study on droplet penetration through the mask was performed to emulate the contamination of a nearby person while a masked infected patient is sneezing or

coughing. For this, we kept two masks of the same materials in close proximity (about 1 cm apart), and dyed aqueous glycerol (60% by volume) was sprayed through one of the masks (mask 1). After spraying, the other mask (mask 2) surface was observed under the fluorescence microscope to check the depositions (Figure 3.12). The results revealed that mask 1 when sprayed with liquid may have led to the transmission of the liquid to the nearby mask 2 predominantly by direct droplet penetration through mask 1 and maybe to some extent by diffusion from liquid-laden mask 1 to pristine mask 2. Due to the larger pore size of Muga silk (sample C), the droplets could pass through the pores and showed the highest deposition of 61% of the dye on mask 2, whereas, N95 (sample G) showed the minimum deposition of 0.06% on mask 2 possibly due to its small pore size.

3.4 Conclusion

In this work, we have investigated the performance of cloth, silk, surgical and N95 masks primarily in terms of their capability to absorb liquid droplets that were sprayed upon the fabrics. It was found that N95 and surgical masks were among the least liquid-absorbing masks with less fractional area coverage by the droplets on the outer layer of the mask. On the other hand, the hydrophilic cloth was found to have the highest capability to absorb liquid with the fractional area covered by the incoming droplets >35%. Although the N95 mask was the best, it had poor breathability, unlike a comfortable cloth mask. As a recent article[23] indicated that the SARS-CoV-2 virus is airborne, the liquid absorption capability of a mask is a topic of great concern. Masks having a high capability of absorption of liquid can be the source of plausible infection. The situation becomes more detrimental if the mask is poorly breathable as this may induce oxygen deficiency in the bloodstream of a patient due to lack of air passing through the mask. This would induce strong inhalation, which may help carry pathogens inward through the layers of the mask from the outer layers of the liquid-laden mask. Thus, it would be better to have a reasonably breathable mask having low liquid absorption capability. In this direction, we have modified a hydrophilic mask (Eri silk) to a robust hydrophobic breathable mask using a nanometer-thick

coating of OTS. The mask fabric exhibited low liquid absorption capability even at the high impact of (aqueous) liquid drops. The droplets hitting the outer layer of the modified Eri silk fabric repelled off, which prevented deposition of the droplet on its surface. Wearing a three-layered modified hydrophobic Eri silk mask might be sufficient to reduce the chance of being infected or spreading an infection to others. Along with the top hydrophobic layer prescribed in this work, one can also use multifunctional inner layers such as active antibacterial coating[57] and intermediate electrostatic layers[58] for better protection against airborne pathogens such as SARS-CoV-2.

References

[1] D. K. Chu, E. A. Akl, S. Duda, K. Solo, S. Yaacoub, H. J. Schünemann, A. El-harakeh, A. Bognanni, T. Lotfi, M. Loeb, A. Hajizadeh, A. Bak, A. Izcovich, C. A. Cuello-Garcia, C. Chen, D. J. Harris, E. Borowiack, F. Chamseddine, F. Schünemann, G. P. Morgano, G. E. U. Muti Schünemann, G. Chen, H. Zhao, I. Neumann, J. Chan, J. Khabsa, L. Hneiny, L. Harrison, M. Smith, N. Rizk, P. Giorgi Rossi, P. AbiHanna, R. El-khoury, R. Stalteri, T. Baldeh, T. Piggott, Y. Zhang, Z. Saad, A. Khamis, M. Reinap, *Lancet* **2020**, *395*, 1973–1987.

[2] J. T. Brooks, J. C. Butler, *JAMA* **2021**, *325*, 998–999.

[3] W. H. Organization, *Mask Use in the Context of COVID-19: Interim Guidance, 1 December 2020*, World Health Organization, Geneva PP - Geneva, **n.d.**

[4] W. R. Dugdale CM, *JAMA Intern. Med.* **2020**, *180*, 1612–1613.

[5] R. J. Roberge, E. Bayer, J. B. Powell, A. Coca, M. R. Roberge, S. M. Benson, *Ann. Occup. Hyg.* **2010**, *54*, 671–677.

[6] Y. Yue, J. Wang, W. He, Y. Guo, H. Gao, J. Liu, *ACS Nano* **2020**, *14*, 13161–13171.

[7] O. Aydin, B. Emon, S. Cheng, L. Hong, L. P. Chamorro, *Extrem. Mechnics Lett.* **2020**, *40*, 100924.

[8] Y. Wibisono, C. R. Fadila, S. Saiful, M. R. Bilad, *Polymers (Basel).* **2020**, *12*, 1–18.

[9] N. P. B. Tan, S. S. Paclijan, H. N. M. Ali, C. M. J. S. Hallazgo, C. J. F. Lopez, Y. C. Ebora, *ACS Appl. Nano Mater.* **2019**, *2*, 2475–2483.

[10] H. Shen, Z. Zhou, H. Wang, M. Zhang, M. Han, D. P. Durkin, D. Shuai, Y. Shen, *Environ. Sci. Technol. Lett.* **2021**, DOI 10.1021/acs.estlett.1c00337.

[11] J. Bayersdorfer, S. Giboney, R. Martin, A. Moore, R. Bartles, *Am. J. Infect. Control* **2020**, *48*, 1543–1545.

[12] M. H. Chua, W. Cheng, S. S. Goh, J. Kong, B. Li, J. Y. C. Lim, L. Mao, S. Wang, K. Xue, L. Yang, E. Ye, K. Zhang, W. C. D. Cheong, B. H. Tan, Z. Li, B. H. Tan, X. J. Loh,

Research **2020**, *2020*, 1–40.

[13] A. F. Parlin, S. M. Stratton, T. M. Culley, P. A. Guerra, *PLoS One* **2020**, *15*, e0239531.

[14] S. Rengasamy, B. Eimer, R. E. Shaffer, *Ann. Occup. Hyg.* **2010**, *54*, 789–798.

[15] M. P. Borah, S. Jose, B. B. Kalita, D. B. Shakyawar, P. Pandit, *J. Text. Inst.* **2020**, *111*, 701–708.

[16] D. Gogoi, A. J. Choudhury, J. Chutia, A. R. Pal, N. N. Dass, D. Devi, D. S. Patil, *Appl. Surf. Sci.* **2011**, *258*, 126–135.

[17] A. Konda, A. Prakash, G. A. Moss, M. Schmoldt, G. D. Grant, S. Guha, *ACS Nano* **2020**, *14*, 6339–6347.

[18] V. Arumuru, J. Pasa, S. S. Samantaray, V. S. Varma, *AIP Adv.* **2021**, *11*, 045205.

[19] V. Arumuru, J. Pasa, S. S. Samantaray, *Phys. Fluids* **2020**, *32*, 115129.

[20] S. Sharma, R. Pinto, A. Saha, S. Chaudhuri, S. Basu, *Sci. Adv.* **2021**, *7*, 1–12.

[21] E. P. Fischer, M. C. Fischer, D. Grass, I. Henrion, W. S. Warren, E. Westman, *Sci. Adv.* **2020**, *6*, 1–5.

[22] A. Balazy, M. Toivola, A. Adhikari, S. K. Sivasubramani, T. Reponen, S. A. Grinshpun, *Am. J. Infect. Control* **2006**, *34*, 51–57.

[23] T. Greenhalgh, J. L. Jimenez, K. A. Prather, Z. Tufekci, D. Fisman, R. Schooley, *Lancet* **2021**, *397*, 1603–1605.

[24] A. Tcharkhtchi, N. Abbasnezhad, M. Zarbini Seydani, N. Zirak, S. Farzaneh, M. Shirinbayan, *Bioact. Mater.* **2021**, *6*, 106–122.

[25] M. Akalin, I. Usta, D. Kocak, M. S. Ozen, in *Woodhead Publ. Ser. Text.* (Eds.: S.C. Anand, J.F. Kennedy, M. Miraftab, S.B.T.-M. and H.T. Rajendran), Woodhead Publishing, **2010**, pp. 93–97.

[26] L. Liao, W. Xiao, M. Zhao, X. Yu, H. Wang, Q. Wang, S. Chu, Y. Cui, *ACS Nano* **2020**, *14*, 6348–6356.

[27] G. S. Larsen, Y. Cheng, L. L. Daemen, T. N. Lamichhane, D. K. Hensley, K. Hong, H.

M. Meyer, S. J. Monaco, A. M. Levine, R. J. Lee, E. Betters, K. Sitzlar, J. Heineman, J. West, P. Lloyd, V. Kunc, L. Love, M. Theodore, M. P. Paranthaman, *ACS Appl. Polym. Mater.* **2021**, *3*, 1022–1031.

[28] L. K. Pandey, V. V. Singh, P. K. Sharma, D. Meher, U. Biswas, M. Sathe, K. Ganesan, V. B. Thakare, K. Agarwal, *Sci. Rep.* **2021**, *11*, 10187.

[29] S. Bhattacharjee, C. Raina, X. Wen, P. Bahl, U. Kumar, A. Ahmad, R. Joshi, *Carbon N. Y.* **2020**, *166*, 148–163.

[30] J. T. Huang, V. J. Huang, *J. Int. Med. Res.* **2007**, *35*, 213–223.

[31] P. K. Kang, D. O. Shah, *Langmuir* **1997**, *13*, 1820–1826.

[32] L. S. McCarty, G. M. Whitesides, *Angew. Chemie - Int. Ed.* **2008**, *47*, 2188–2207.

[33] Y. Li, X. Yin, Y. Si, J. Yu, B. Ding, *Chem. Eng. J.* **2020**, *398*, 125626.

[34] K. W. Lee, B. Y. H. Liu, *J. Air Pollut. Control Assoc.* **1980**, *30*, 377–381.

[35] S. Bhattacharjee, P. Bahl, A. A. Chughtai, C. R. MacIntyre, *BMJ Open Respir. Res.* **2020**, *7*, 1–10.

[36] W. C. Hinds, *Aerosol Technology: Properties, Behaviour, and Measurement of Airborne Particles.*, Wiley, **1982**.

[37] S. Bhattacharjee, P. Bahl, C. De Silva, C. Doolan, A. A. Chughtai, D. Heslop, C. R. Macintyre, *ACS Biomaterilas Sci. Eng.* **2021**, *7*, 2791–2802.

[38] S. Bhattacharjee, C. R. Macintyre, P. Bahl, U. Kumar, X. Wen, A. A. Chughtai, R. Joshi, *Adv. Mater. Interfaces* **2020**, *7*, 2000814.

[39] D. Devi, N. Sen Sarma, B. Talukdar, P. Chetri, N. N. Dass, *J. Text. Inst.* **2011**, *102*, 527–533.

[40] Y. Xue, F. Wang, M. Torculas, S. Lo, X. Hu, *ACS Biomaterilas Sci. Eng.* **2019**, *5*, 6361–6373.

[41] A. K. Saikia, H. Goowalla, *J. Arts Soc. Sci.* **2016**, *1*, 10–13.

[42] S. K. Lai, Y.-Y. Wang, D. Wirtz, J. Hanes, *Adv. Drug Deliv. Rev.* **2009**, *61*, 86–100.

[43] J. Li, H. Wan, Y. Ye, H. Zhou, J. Chen, *Appl. Surf. Sci.* **2012**, *261*, 470–472.

[44] L. Zhang, A. G. Zhou, B. R. Sun, K. S. Chen, H. Z. Yu, *Nat. Commun.* **2021**, *12*, 982.

[45] P. Gogoi, A. Chattopadhyay, P. S. G. Pattader, *J. Phys. Chem. B* **2020**, *124*, 11530–11539.

[46] C. M. K. Saner, K. L. Lusker, Z. M. LeJeune, W. K. Serem, J. C. Garno, *Beilstein J. Nanotechnol.* **2012**, *3*, 114–122.

[47] N. Bhandaru, R. Mukherjee, *Macromolecules* **2021**, *54*, 4517–4530.

[48] C. Wu, Q. Liu, J. Liu, R. Chen, K. Takahashi, L. Liu, R. Li, P. Liu, J. Wang, *New J. Chem.* **2017**, *41*, 12767–12776.

[49] M. H. Abumaree, L. Zhu, C. J. Bardeen, S. D. Al-Suwaidan, R. O. Al-Kaysi, *RSC Adv.* **2011**, *1*, 884–892.

[50] H. W. Kwak, J. E. Ju, M. Shin, C. Holland, K. H. Lee, *Biomacromolecules* **2017**, *18*, 2343–2349.

[51] R. G. Candido, in *Fundam. Nat. Fibres Text.* (Ed.: M.I.H. Mondal), Woodhead Publishing, **2021**, pp. 599–624.

[52] B. R. Wood, K. Kochan, D. E. Bedolla, N. Salazar-Quiroz, S. Grimley, D. Perez-Guaita, M. J. Baker, J. Vongsvivut, M. Tobin, K. Bambery, D. Christensen, S. Pasricha, A. K. Eden, A. Mclean, S. Roy, J. Roberts, J. Druce, D. A. Williamson, J. McAuley, M. Catton, D. Purcell, D. Godfrey, P. Heruad, *Angew. Chem. Int. Ed. Engl.* **2021**, DOI 10.1002/anie.202104453.

[53] V. Vuorinen, M. Aarnio, M. Alava, V. Alopaeus, N. Atanasova, M. Auvinen, N. Balasubramanian, H. Bordbar, P. Erästö, R. Grande, N. Hayward, A. Hellsten, S. Hostikka, J. Hokkanen, O. Kaario, A. Karvinen, I. Kivistö, M. Korhonen, R. Kosonen, J. Kuusela, S. Lestinen, E. Laurila, H. J. Nieminen, P. Peltonen, J. Pokki, A. Puisto, P. Råback, H. Salmenjoki, T. Sironen, M. Österberg, *Saf. Sci.* **2020**, *130*, 104866.

[54] S. Anand, Y. S. Mayya, *Sci. Rep.* **2020**, *10*, 1–9.

[55] U. U. Ghosh, S. Nair, A. Das, R. Mukherjee, S. Dasgupta, *Colloids Surfaces A* **2019**, *561*, 9–

17.

[56] D. Roy, K. Pandey, M. Banik, R. Mukherjee, S. Basu, *Proc. R. Soc. A* **2019**, *475*, 20190260.

[57] D. Kharaghani, M. Q. Khan, A. Shahrzad, Y. Inoue, T. Yamamoto, S. Rozet, Y. Tamada, I. S. Kim, *Nanomaterials* **2018**, *8*, 1–12.

[58] S. B. Martin, E. S. Moyer, *Appl. Occup. Environ. Hyg.* **2000**, *15*, 609–617.

Chapter 4

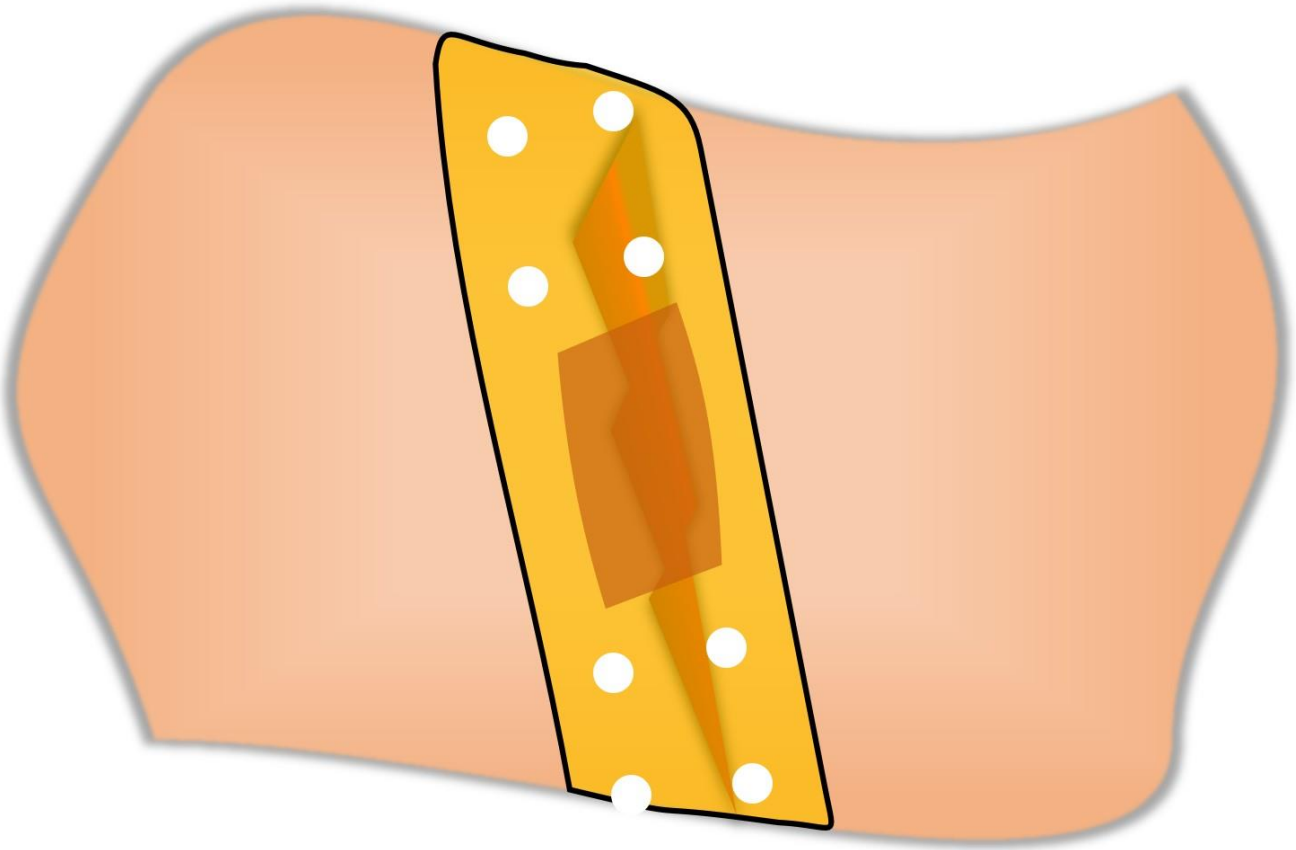

Chapter 4

Chemically Coated Robust Reusable Highly Hydrophobic Bandages

ABSTRACT

For faster wound healing, many wound dressing techniques are available to the human populace. These techniques may be in the physical form, such as gauge bandage, bandaid, crepe bandage, etc., which are usually tied over the wound. Alternatively, new techniques such as film, foam, or gel have also evolved that may act as a drug delivery system when placed above a wound. Even with various alternatives, we noticed that people still prefer the physical form of bandage. However, the major disadvantage is that these bandages are not reusable. Once it comes in contact with water, the dampened bandages get stuck to the wound, thus making it difficult to remove it. We have developed a procedure to modify the already available bandages and make them efficient in repelling the water from the bandage surface. Octadecyltrichlorosilane (OTS) treatment makes these bandages hydrophobic, which can be used repeatedly upto ten times even after exposure to water each time, as the contact angle of water decreases by only 17%.

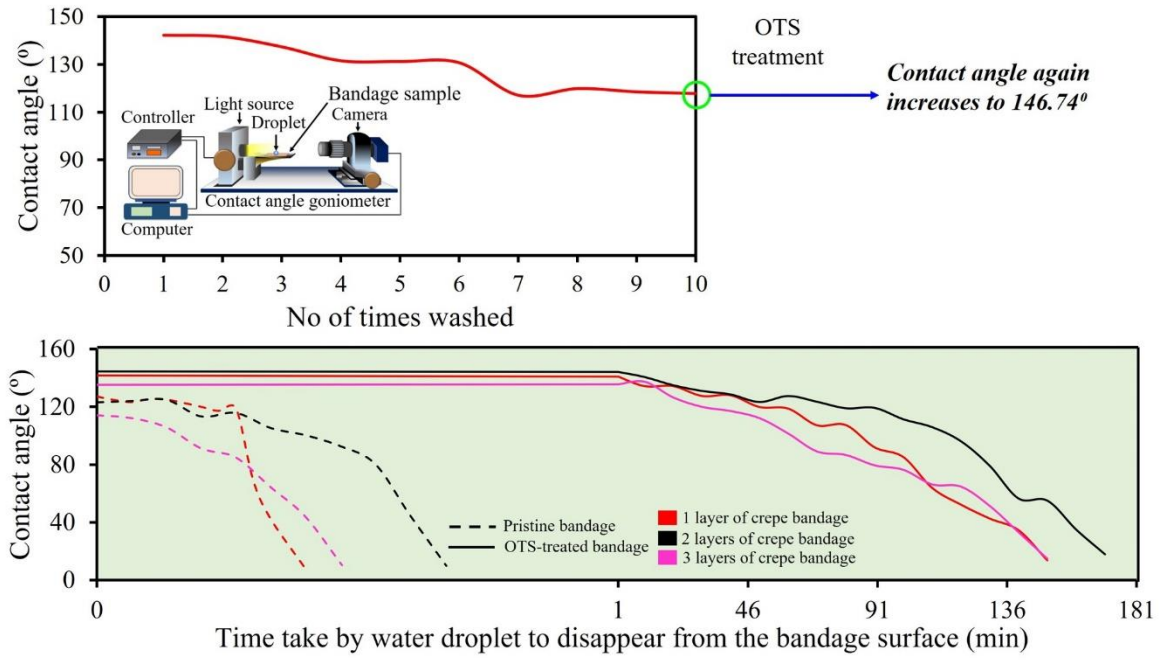

CHAPTER 4

4.1. Introduction

Wound dressing followed by proper bandaging plays a crucial role in the entire wound healing process. The earliest evidence of wound treatment dates back to 2500 B.C.E. (Before Common Era) when Mesopotamians used clay tablets to heal wounds.[1] In India, the concept of wound dressing came into existence around 700-600 B.C.E., when the Father of Surgery Sushruta mentioned in his medical treatise about Sodhan, i.e., keeping wounds clean and soft, followed by Ropan, i.e., healing of wounds using the listed 100 plants either individually or in different combinations.[2,3] Conventionally, wounds were covered by woven or non-woven cotton, rayon or polyester type of cotton, gauge, lint bandages, plasters, etc., to avoid any contamination. The major disadvantages of these bandages include being used only in clean, dry wounds and can even stick to the wound due to the excessive wound drainage liquid making it strenuous to remove the bandage later.[4] However, a bandage should keep the wound relatively moist, removing the excess exudate released and adjusting the exchanges of gases.[5]

On account of these drawbacks, by the 20th century, people gradually started shifting towards modern dressing techniques where apart from just protecting the wound, the main intention was to promote the functioning of the wound for speedy healing.[1,6,7] These includes synthetic polymers or biomaterials which act as passive, interactive, and bioactive bandage. Passive bandage includes non-occlusive gauge bandage, interactive bandage includes semi-occlusive or occlusive films[8,9], foams[10,11], hydrogels[11,12], hydrocolloid,[4,13] etc. and bioactive bandage includes biocompatible polymers from collagen[14,15], chitosan[16], hyaluronic acid[17] to name a few.

An asymmetric wettable bandage with an electrospuned polycaprolactone (PCL) hydrophobic outer layer prevents the incoming bacteria from accumulating and colonizing over the bandage. To expedite the wound healing process, the inner layer is made hydrophilic by electrospinning Pioglitazone filled gelatin nanofibers to the PCL layer.[18] The capable property of Pioglitazone to form new blood vessels helps in the speedy recovery of the wounds. Furthermore, fluorescent nanosheets of Magnesium hydroxide are incorporated into biocompatible

electrospuned PCL fibers to fabricate antimicrobial wound dressing bandages. These noninvasive inherent pH-dependent fluorescent properties aid in the easy detection of the acidifying microenvironment required for wound healing.[19] Researchers developed another noninvasive thermally responsive drug-loaded poly(N-isopropylacrylamide-co-acrylic acid) (P(NIPAM-co-AAc))[20] hydrogel functionalized spandex fabric for real-time monitoring of drug loading and release during the wound healing process.[21] The Fe_3O_4@C nanoparticles present inside the hydrogel acted as photonic crystals that release drugs to the wounds by mild heating to a temperature greater than 40 °C.

A simple and cost-effective method is developed where anti-bacterial cotton bandages are prepared by mineralizing ZnO nanoparticles over Poly(allylamine) coated pristine cotton bandage.[22] These nanoparticles are not only safe for human use[23] but also witnessed a reduction in bacterial growth by 63% for E.coli after five hours. Moreover, researchers developed robust antibacterial liquid bandages[24] that impair themselves in 7 days of usage.[25] Shellac[26] is a natural polymer resin that can act as a hydrophobic, self-adhesive liquid barrier when placed above wounds. Further, Copper and Zinc are added to the shellac to enhance the contact-killing properties of the bacteria. In addition, antimicrobial silk sponges fabricated by modifying the surface with layer-by-layer self-assembly[27] of cationic PolyA polymer solution and Sodium Alginate also demonstrated contact-active killing phenomena on exposure to different types of bacteria such as E. coli, P. aeruginosa and S. aureus.[28]

With numerous advancements in wound dressing technology, humankind also saw the inception of flexible waterproof micron thick electronic bandages[29] incorporated with composites of carbon nanotubes and silver nanoparticles. These act as motion-related sensors when placed over the skin for easy detection of the movement of joints and muscles. Moreover, they exhibit excellent stability against water and sweat (tested with Sodium Chloride solution of concentration 0.5 mol/L, similar to human sweat) for 100 h.[30] Moreover, these electronic bandages are considered smart with daily effortless remote detection of interior wound environment such as

irregular bleeding, change in pH, external pressure, etc. These also minimize the enormous workload faced by the health care workers.[31]

Superhydrophobic self-cleaning[32] mechanically durable cotton bandage inspired from lotus leaf, mussel, and sandcastle worm is prepared by coating iMglue on both sides of the bandage and additionally spraying hydrophobic SiO_2 nanoparticles on the outer side only. iMglue is an immiscible Mussel adhesive protein[33] with outstanding properties such as antithrombotic, anti-biofouling,[34] and biocompatible tissue closure properties. Moreover, this iMglue/SiO_2 coated bandage continued to display a water contact angle of greater than ~150° even after five abrasion cycles.[35]

There are more than 3000 different types of bandages available in the market, and each type is suitable for a specific type of wound care. The conventionally available dressings are generally hydrophilic in nature, as a result of which exposure to water makes it wet, and frequent changing is required for faster healing of the wounds. It is also commonly observed that people cover their bandages with plastic sheets while bathing or doing any work involving water exposure. Besides, nowadays, custom-made plastic bags are available in the market to cover the bandaged parts. In our work, we have demonstrated a process to modify the conventionally available bandages so as to repel the incoming water and keep the wounds dry for rapid healing. Treating these bandages with Octadecyltricholorosilane (OTS) contribute to the hydrophobic nature of the bandage. These treated bandages retain their hydrophobicity even after repeated washing and can be stored for a long duration of time to be used later.

4.2 Experimental Methods

4.2.1. Types of bandages

In this study, we have considered four different types of bandages (Table 4.1) that are commonly available in the market and also used by the common populace often to clean and cover wounds.

Table 4.1. Different type of bandages used in the current study

Sl. No.	Types of bandage	Nature of bandage
1	Bandaid	Hydrophilic/hydrophobic
2	Crepe bandage	Hydrophilic
3	12-ply gauge bandage	Hydrophilic
4	Cotton	Hydrophilic

4.2.2. Experimental setup

All the experiments were carried out with the help of a goniometer under normal diffusing conditions. The sample pieces of bandages were placed on the goniometer stage, as shown in Figure 4.1. A 5 μL water droplet was placed on top of the bandage surface. During the evaporation process, the change in contact angle of the water droplet was monitored as a function of time through the in-built camera present in the goniometer. The surrounding temperature was maintained at 23 ± 2 °C and relative humidity at ~ 58 ± 2%.

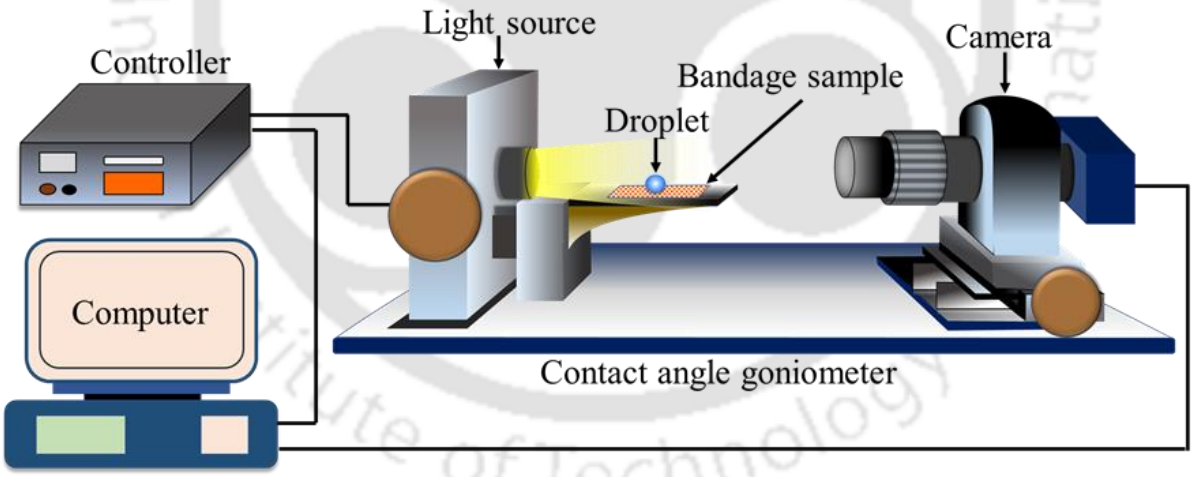

Figure 4.1. The experimental setup shows the bandage with a water droplet placed on it, on the goniometer stage.

4.2.3. Preparation of octadecyltrichlorosilane (OTS) solution

In 10 mL toluene 20 μL of octadecyltrichlorosilane (OTS) was mixed to prepare the OTS solution. After that, the solution was stirred for 10 min for uniform dispersion of OTS particles in toluene. The solution was then heated on a hot plate at 60 ºC for 30 min and finally cooled to room temperature before being used for further experiments.

4.2.4. Preparation of hydrophobic bandage

The procured bandages were washed with detergent to remove any dirt present on them and then washed with acetone for 1 min to remove any excess detergent accumulated on the bandage. These bandages were washed with DI water for 2 min to remove the excess acetone. Initially, they were dried with nitrogen gas to remove the excess water. Once the bandage pieces became moist, they were dried in a hot air oven at around 100 ^{o}C for 10 min to make them completely dry. After that, the fabric was immediately transferred into the OTS solution[36] prepared (several pieces of them) and kept for 30 min before being washed with toluene to remove the excess OTS present on the fiber. Then these pieces were dried with nitrogen and finally kept in a hot air oven at 80 ^{o}C for 10 min.

4.2.5. Contact angle measurement and quantitative analysis

The evaporation of the DI water droplet was recorded at a frame rate of 30 fps using a contact angle Goniometer (Holmarc Opto-Mechatronics, Model: HO-IAD-CAM-01B). The inbuilt software application "Holmarc Contact Angle Measurement" was used to estimate the contact angle of the water droplet with respect to time.

4.3 Results and Discussion

4.3.1. Hydrophilicity of bandages

At the very beginning, we studied how the water droplets interact on the surface of commercially available bandages. The commercially available adhesive bandaid is usually made of plastics/polymers[37] like PVC (Polyvinyl chloride), polyethylene, and polyurethane[38] with an adhesive acrylate[39] layer below it. Hence these bandaids can repel water to some extent. We have used a fabric woven bandaid for our experiment and saw that the contact angle made by the water droplet initially was 127.52°, as shown in Figure 4.2. Due to its hydrophobic nature, the water droplet penetrated minimum and remained on its surface for a time duration of around 2 h 40 min. We could also see a decrease in the contact angle of the water due to the natural evaporation process owing to the surrounding environmental conditions. On the other hand, cotton and 12-

ply gauge bandages showed hydrophilic properties as the water droplet is absorbed immediately. Lastly, we have done our experiments using crepe bandage in three ways (1-ply crepe bandage, 2-ply crepe bandage and 3-ply crepe bandage), as crepe bandage can be used to cover any targeted

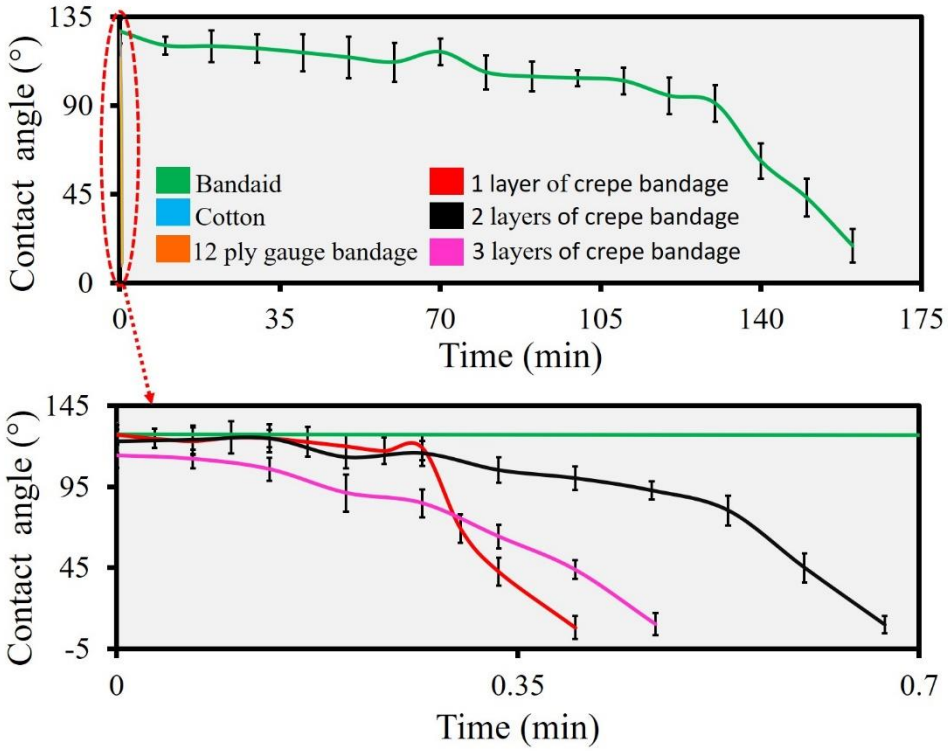

Figure 4.2. Graph showing the hydrophilic nature of different bandages used in the experiment. The graphs for cotton and 12 ply gauge bandages is not shown as the water gets immediately absorbed by them.

area in different layers. It was observed that the initial contact angle made by water is 127.1°, 122.95°, and 114.16° for 1-ply, 2-ply, and 3-ply crepe bandages, respectively. However, in all the cases, the water gets absorbed by the bandage within 40 seconds with a drastic decrease in the contact angle, as shown in Figure 4.2. We have also tried similar experiments after washing the bandages with DI water for 3 mins followed by drying and secondly washing them with household detergent for 3 min followed by drying. In both the cases, the bandages are first dried with nitrogen to remove the excess water until it becomes moist, accompanied by final drying on a hot plate at 60 °C for 30 min. We observed that the hydrophilic nature is retained even after the washing treatment, as shown in Figures 4.4 and 4.5. So, this clearly states that the commercially available conventional bandages are usually hydrophilic in nature.

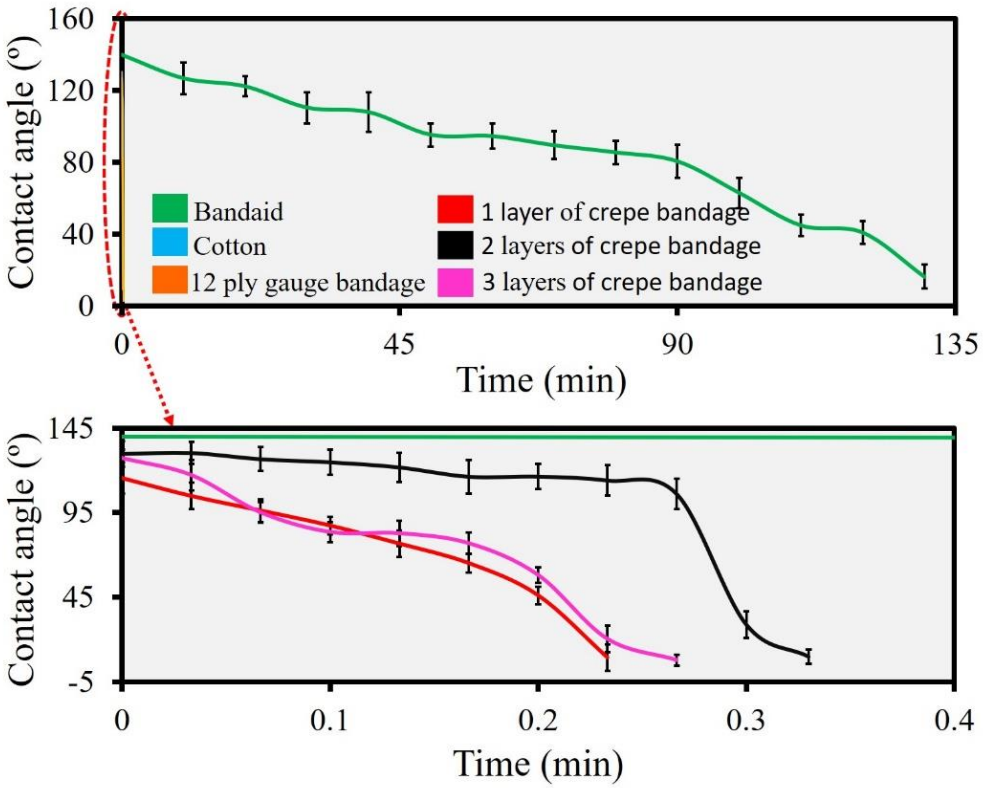

Figure 4.3. Graph showing the hydrophilic nature of different bandages after washing with water followed by drying. The graphs for cotton and 12 ply gauge bandages cannot be shown as the water gets immediately absorbed by them.

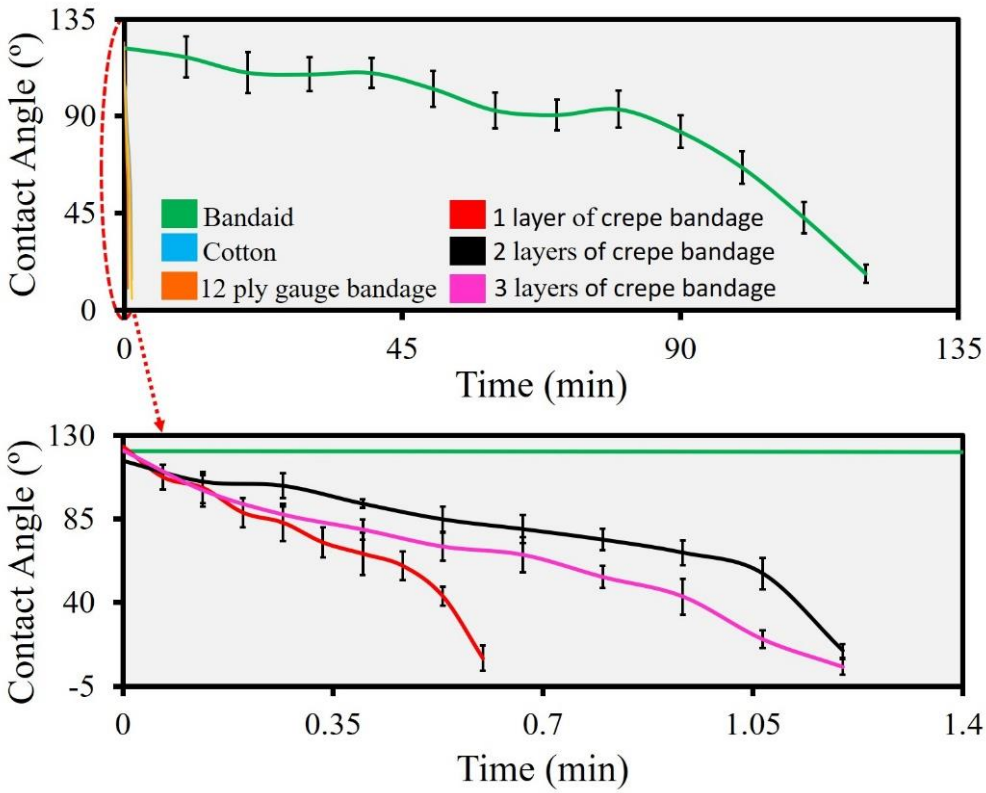

Figure 4.4. Graph showing the hydrophilic nature of different bandages after washing with detergent followed by drying. The graphs for cotton and 12 ply gauge bandages cannot be shown as the water gets immediately absorbed by them.

4.3.2. Functionality of modified OTS treated bandages

Here we examined how the water droplets interacted with the OTS-treated bandages. The water droplets made a contact angle > 130° for all types of OTS-treated bandages, as shown in Figure 4.5. Owing to their hydrophobicity, the water droplet rests on the surface, which gradually gets evaporated in ~3 h due to the natural convection process. It was very interesting to observe that the bandages retained their hydrophobic properties even after washing with DI water or with regular household detergent, as shown in Figures 4.6 and 4.7 (the washing and drying procedure is the same as mentioned in the section "hydrophilicity of bandages"). These OTS-treated bandages with excellent properties to repel the water droplets could be a great source to cover the wounds while performing any everyday work that requires direct contact with water.

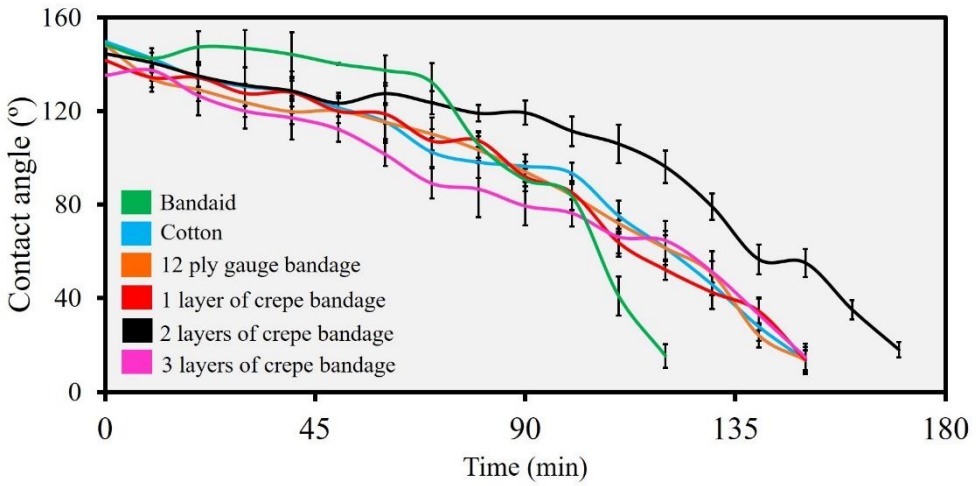

Figure 4.5. Graph showing the behavior of conventional bandages after OTS treatment.

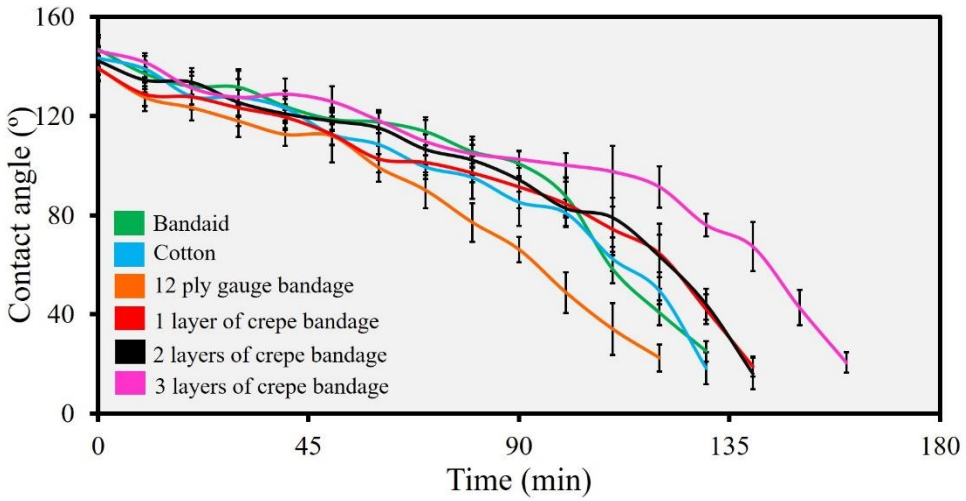

Figure 4.6. Graph showing the behavior of modified bandages (OTS-treated) after washing with water followed by drying.

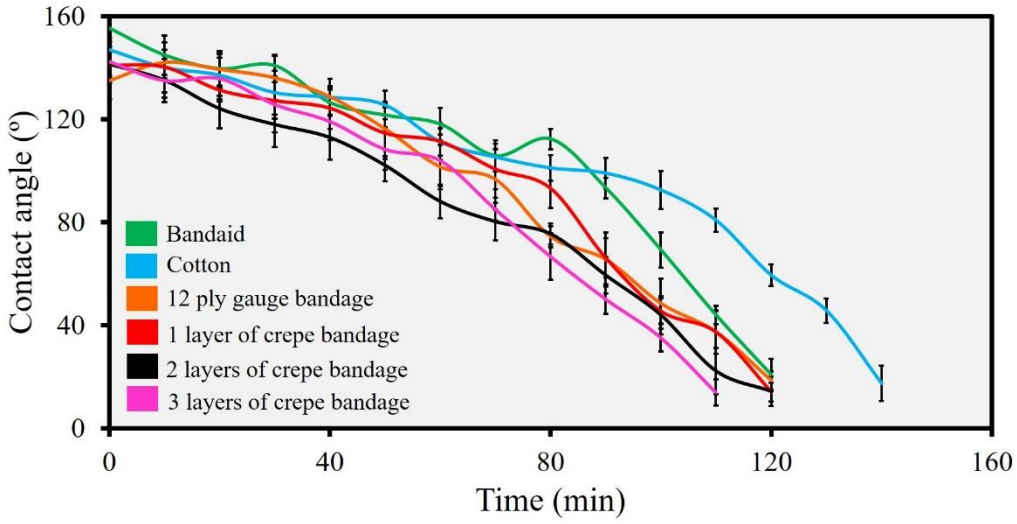

Figure 4.7. Graph showing the behavior of modified bandages (OTS-treated) after washing with detergent followed by drying.

4.3.3. The distinction between as-purchased bandaid and OTS-treated bandaid

As both the as-purchased and OTS-treated bandaids appeared hydrophobic in our earlier experiments, we checked for their feasibility in normal working conditions. 25 μL water droplet was placed on both types of bandaid, and the water was rubbed on the bandaid surface with a finger in a circular motion five times, followed by noting the contact angle made the water droplet each time. The contact angle decreases drastically for the as-purchased bandaid every time the surface is rubbed with water

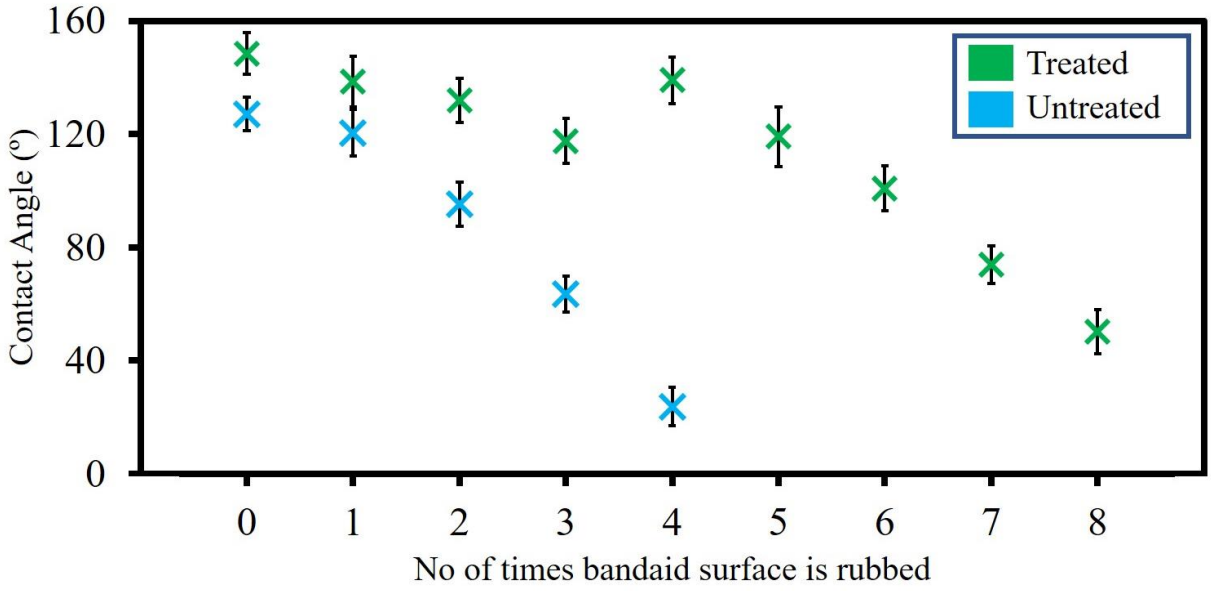

Figure 4.8. The behavior of both untreated and treated bandaid after rubbing the bandaid surface with a finger in a circular motion with water.

(Figure 4.8). Eventually, after the fourth rubbing, the bandaid becomes completely hydrophilic with a water contact angle of 23.77°, as shown in Figure 4.8. Whereas the OTS-treated bandaid remained hydrophobic upto its sixth rubbing, which had a contact angle of 100.82°. Although the bandaid retained its hydrophobicity after every rubbing, we observed a moderate decrease in the contact angle after each rubbing. However, after the sixth rubbing, the hydrophobic nature of the bandaid deteriorated gradually to form a slightly hydrophilic surface showing a water contact angle of 50.17° in the eighth rubbing.

4.3.4. Reusability of the OTS treated crepe bandage

Another set of experiments was performed where the treated crepe bandage was checked for the change in contact angle after thorough washing with water. The treated crepe bandage was first washed with water for 3 min, followed by drying with nitrogen gas until it became moist and then in the hot plate at 60 °C for 15 mins to make it completely dry. Finally, the contact angle of water was measured after every washing with the help of the goniometer. Although there was a slight reduction in the contact angle after every washing, the final decline of the contact angle was only 117.77°, i.e., it is reduced by 17% after the tenth washing showing the hydrophobicity retainment (Figure 4.9). Further, OTS treatment on these washed bandages (10th time washed bandage taken for OTS treatment) increased the contact angle of water again to 146.74^{0}.

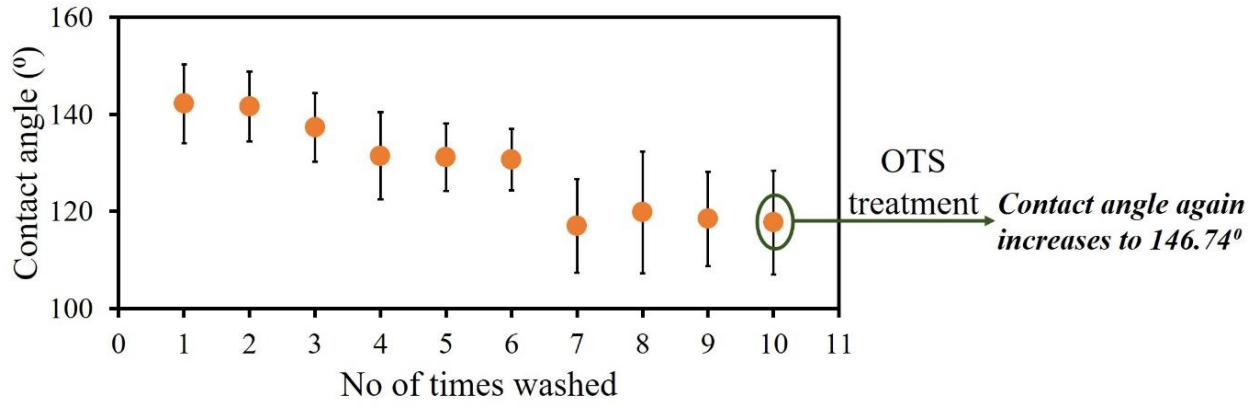

Figure 4.9. The graph shows the decreased contact angle of the treated crepe bandage after each washing.

Lastly, we performed OTS treatment on the OTS-treated crepe bandage once more and saw that the contact angle of water on the bandage increased to 155.66° from 141.67°. Moreover, the hydrophobicity is retained by the OTS-treated crepe bandage even after a period of one month, as we see the water contact angle decreases to only 133.10°.

4.4. Conclusion

Wound care and healing have been known to humans for centuries, and it has worked with immense satisfaction amongst the patients due to their relief from the recovering wounds. Nevertheless, it is always realized that the patients must go through a lot of toil to remove the bandage during repeated changing as it gets stuck to the wound and is frequently contaminated. At the same time, it is a hassle for medical personnel to change the bandage repeatedly. We have developed a procedure to modify the already available conventional non-occlusive bandages into a hydrophobic bandage that will neither get stuck to the wounds nor will get wet in moist conditions. These modified bandages have a water contact angle greater than 140°, making it highly hydrophobic. Moreover, these modified bandages can be used repeatedly upto 10 times in wet conditions with a decrease in contact angle by only 17%. The serous liquid produced by the wound in the normal healing process would remain intact on the wound bed rather than being absorbed by the bandage, which will make the healing process much faster.

References

[1] S. Dhivya, V. V. Padma, E. Santhini, *Biomed.* **2015**, *5*, 24–28.

[2] S. Bhattacharya, *Indian J. Plast. Surg.* **2012**, *45*, 177–179.

[3] A. D. Banerjee, H. Ezer, A. Nanda, *World Neurosurg.* **2011**, *75*, 320–323.

[4] J. S. Boateng, K. H. Matthews, H. N. E. Stevens, G. M. Eccleston, *J. Pharm. Sci.* **2008**, *97*, 2892–2923.

[5] J. Bueno, F. Demirci, K. H. C. Baser, in *Clin. Microbiol. Diagnosis, Treat. Prophyl. Infect.* (Eds.: K. Kon, M.B.T.-T.M. of S. Rai Soft Tissue, Bone and Joint Infections), Academic Press, **2017**, pp. 271–286.

[6] H. J. Degreef, *Dermatol. Clin.* **1998**, *16*, 365–375.

[7] A. E. Rivera, J. M. Spencer, *Clin. Dermatol.* **2007**, *25*, 39–48.

[8] V. Moshakis, M. J. Fordyce, J. D. Griffiths, J. A. McKinna, *Br. J. Clin. Pract.* **1984**, *38*, 149–152.

[9] J. B. Debra, O. Cheri, *Technol. Catal. Int. Corp.* **1998**, *2*, 1–185.

[10] D. A. Morgan, *Hosp. Pharm.* **2002**, *9*, 261–266.

[11] T. Thomson, *Foam Composite*, **2006**, 7048966.

[12] L. Martin, C. G. Wilson, F. Koosha, L. Tetley, A. I. Gray, S. Senel, I. F. Uchegbu, *J. Control. Release* **2002**, *80*, 87–100.

[13] S. Thomas, *J. Wound Care* **1992**, *1*, 27–30.

[14] J. A. Ramshaw, J. A. Werkmeister, V. Glattauer, *Biotechnol. Genet. Eng. Rev.* **1996**, *13*, 335–382.

[15] S. H. Liu, R. S. Yang, R. al-Shaikh, J. M. Lane, *Clin. Orthop. Relat. Res.* **1995**, 265–278.

[16] M. Ishihara, K. Nakanishi, K. Ono, M. Sato, M. Kikuchi, Y. Saito, H. Yura, T. Matsui, H. Hattori, M. Uenoyama, A. Kurita, *Biomaterials* **2002**, *23*, 833–840.

[17] C. J. Doillon, F. H. Silver, *Biomaterials* **1986**, *7*, 3–8.

[18] B. Yu, C. He, W. Wang, Y. Ren, J. Yang, S. Guo, Y. Zheng, X. Shi, *ACS Appl. Bio Mater.* **2020**, *3*, 5383–5394.

[19] A. Truskewycz, V. K. Truong, A. S. Ball, S. Houshyar, N. Nassar, H. Yin, B. J. Murdoch, I. Cole, *ACS Appl. Mater. Interfaces* **2021**, *13*, 27904–27919.

[20] Z. H. Farooqi, H. U. Khan, S. M. Shah, M. Siddiq, *Arab. J. Chem.* **2017**, *10*, 329–335.

[21] X. Gong, C. Hou, Q. Zhang, Y. Li, H. Wang, *ACS Appl. Mater. Interfaces* **2020**, *12*, 51225–51235.

[22] J. Manna, G. Begum, K. P. Kumar, S. Misra, R. K. Rana, *ACS Appl. Mater. Interfaces* **2013**, *5*, 4457–4463.

[23] P. K. Stoimenov, R. L. Klinger, G. L. Marchin, K. J. Klabunde, *Langmuir* **2002**, *18*, 6679–6686.

[24] E. Rezvani Ghomi, S. Khalili, S. Nouri Khorasani, R. Esmaeely Neisiany, S. Ramakrishna, *J. Appl. Polym. Sci.* **2019**, *136*, 1–12.

[25] C. A. P. Bastos, W. D. Thom, B. Reilly, I. L. Batalha, M. L. Burge Rogers, I. S. McCrone, N. Faria, J. J. Powell, *Sci. Rep.* **2020**, *10*, 1–8.

[26] S. Maiti, S. Rahman, *J. Macromol. Sci. Part C* **1986**, *26*, 441–481.

[27] G. Wu, H. Deng, T. Jiang, H. Tu, J. Chen, Y. Zhan, Y. Wang, X. Ma, *Colloids Surf. B. Biointerfaces* **2017**, *154*, 228—238.

[28] E. Wulandari, R. Namivandi-Zangeneh, P. R. Judzewitsch, R. Budhisatria, A. H. Soeriyadi, C. Boyer, E. H. H. Wong, *ACS Appl. Bio Mater.* **2021**, *4*, 692–700.

[29] H. Derakhshandeh, S. S. Kashaf, F. Aghabaglou, I. O. Ghanavati, A. Tamayol, *Trends Biotechnol.* **2018**, *36*, 1259–1274.

[30] J. Y. Jeon, T. J. Ha, *ACS Appl. Mater. Interfaces* **2016**, *8*, 2866–2871.

[31] M. F. Farooqui, A. Shamim, *Sci. Rep.* **2016**, *6*, 28949.

[32] Y. Lu, S. Sathasivam, J. Song, C. R. Crick, C. J. Carmalt, I. P. Parkin, *Science* **2015**, *347*, 1132–1135.

[33] S. M. Kang, I. You, W. K. Cho, H. K. Shon, T. G. Lee, I. S. Choi, J. M. Karp, H. Lee, *Angew. Chem. Int. Ed. Engl.* **2010**, *49*, 9401–9404.

[34] A. K. Epstein, T.-S. Wong, R. A. Belisle, E. M. Boggs, J. Aizenberg, *Proc. Natl. Acad. Sci. U. S. A.* **2012**, *109*, 13182–13187.

[35] K. Han, T. Y. Park, K. Yong, H. J. Cha, *ACS Appl. Mater. Interfaces* **2019**, *11*, 9777–9785.

[36] P. Gogoi, A. Chattopadhyay, P. S. G. Pattader, *J. Phys. Chem. B* **2020**, *124*, 11530–11539.

[37] Z. Li, X. Feng, S. Gao, Y. Jin, W. Zhao, H. Liu, X. Yang, S. Hu, K. Cheng, J. Zhang, *ACS Appl. Bio Mater.* **2019**, *2*, 613–618.

[38] S. Osmakski, "Compostable Band-Aids: Why It's Time to Make the Switch," can be found under https://www.greenmatters.com/family/2018/12/31/NrSyEsU/compostable-band-aids, **2018**.

[39] T. Widman, H. Oostman, F. Storrs, *Dermatitis* **2007**, *19*, 32–37.

Chapter 5

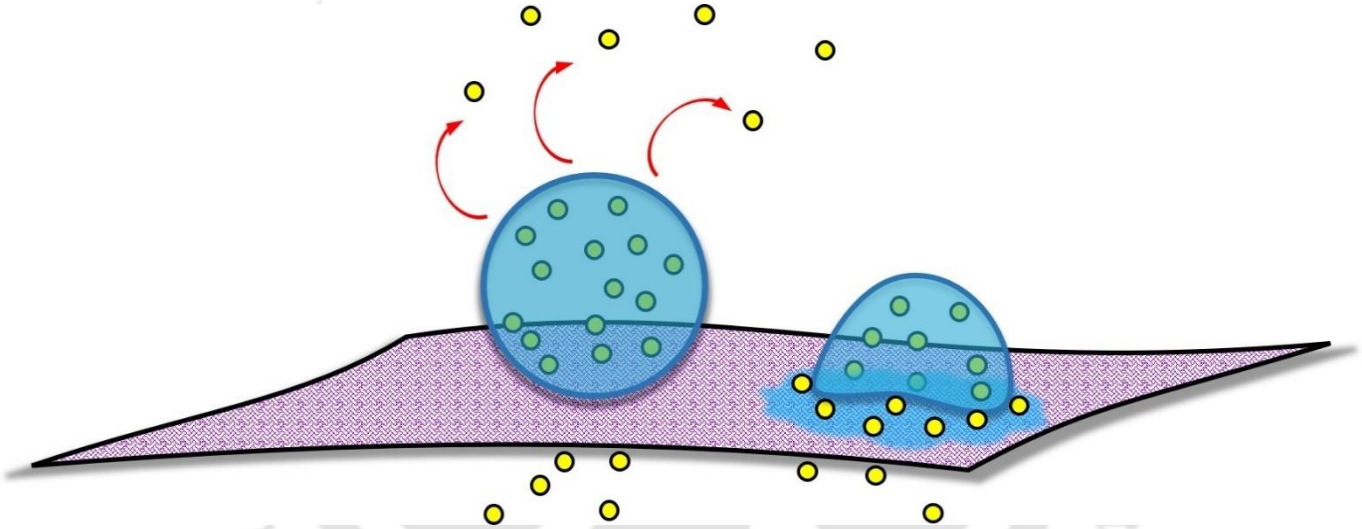

Chapter 5
Microparticle Penetration Through Vibrating Porous Flexible Substrate

ABSTRACT

The mechanical vibration is an interesting phenomenon which is a boon and bane simultaneously for various processes. During the vibration of a flexible porous substrate, the particles present on it will percolate through the substrate; some will be repelled off while the rest sits on the substrate. This flexible porous substrate can be considered as a mask which we wear to protect against pollutant particles or disease-causing microorganisms. When a droplet containing pollutants or coronavirus sits on the mask fabric, the path conveyed by these micro-nano particles present in the droplet depends on the nature of the fabric material and the vibration the fabric is experiencing during talking, breathing, or sneezing. We performed the experiments using both as-purchased Eri silk (hydrophilic), and OTS-treated Eri silk (hydrophobic) porous flexible substrate fixed tightly on a fabricated circular stage, placed above the mechanical vibrator. The mechanical vibrator oscillates based on the frequency and amplitude given to the function generator. The micro-nano particles on the fabric surface and those percolated and deposited on the glass substrate at the bottom of the circular stage were seen under the optical microscope and FESEM.

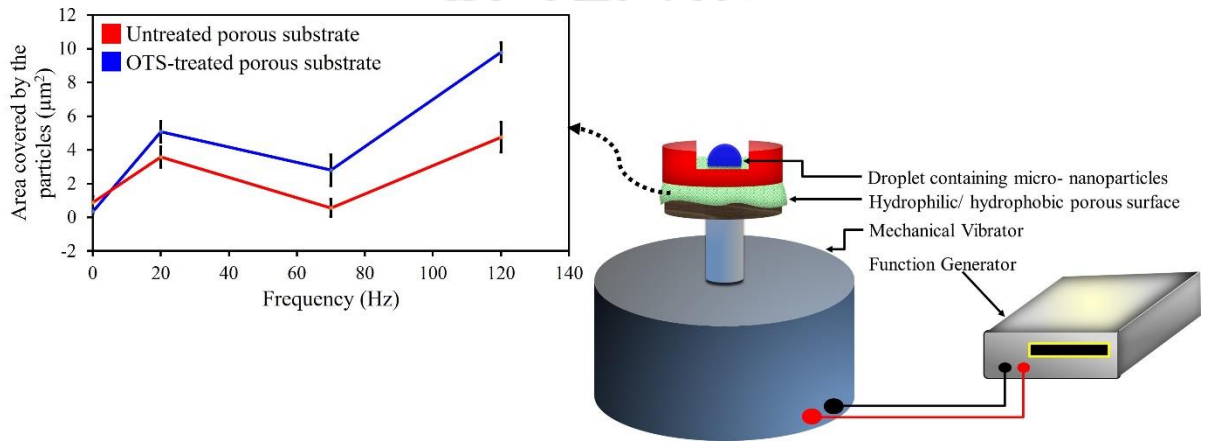

CHAPTER 5

5.1. Introduction

One interesting fact about various objects present in the universe is their constant movement leading to vibration.[1,2] Although some objects appear to be stationary to our naked eyes, they are vibrating, oscillating, and resonating at various frequencies around an equilibrium point in various mediums like air, water, soil, leaf, trees, etc. Paradoxically it would be interesting to say that though the whole body appears stationary, it experiences vibration[3,4], including our skin[5], at some point or the other due to external stimuli. Moreover, vibration transmitted through a solid medium (leaves, ground, water, etc.), also called substrate-borne vibration, is commonly used by animals and insects[6] both for communication and as a source of information[7] in their process of growth, existence, and survival.[8,9] Surprisingly, in our mother nature, vibration has always assisted different surface types for the droplet on them to acquire the correct wetting state.[10,11] For instance, the lotus leaf has unique antidew superhydrophobicity property for repelling the water droplets in the Wenzel[12,13] (or mixed) state due to the nucleation of liquid condensate that forms on the roughened surface with repeated vapor condensation.[14] Usually, the lotus leaves undergo a vibration velocity of 0.1 m/s due to the blowing wind for the water droplet to change from the Wenzel state to the Cassie transition state.[15–18]

Since the 19th-century, researchers have started gaining tremendous interest in droplet behavior under a vibrational environment. When a droplet undergoes vibrational excitation, either periodic or steady changes are witnessed at the three-phase contact line (CL) by altering the solid-liquid three-phase contact angle. Periodic wetting is considered to occur at a low frequency of 0.1 to 10 kHz.[19] These low-frequency vibrations produce sharp oscillations leading to the non-harmonic displacement of CL upon unpinning, followed by repetitive wetting and dewetting of the droplet on the substrate.[19,20] Whereas steady wetting often occurs at a high frequency of 1 MHz-1 GHz. As the oscillation is associated only with the viscous flow immediately adjacent to the sub-micron characteristic length scale of the CL region on the substrate, the droplet experiences steady wetting.[19,21] The substrate vibration also affects the

evaporation rate, with more evaporation occurring with horizontal vibration[22] than with vertical vibration. With horizontal vibration, the top of the liquid film experiences horizontal circulation of air, thus increasing the convective heat transfer[23]. In contrast, a vertical flow is induced towards and away from the liquid surface during vertical vibration, thus creating a stagnation point at the film interface.[24] Droplets also produce various types of modes based on horizontal and vertical vibration, which depends on the mass of the droplet, types of substrate, surface tension, frequency, etc.[25,26]

The vibration phenomenon, a powerful tool in research, has found many applications in various domains. Substrate vibration-assisted spray coating (SVASC)[27,28] is a novel spray-coating method developed by Zabihi and Eslamian, which is one such application used in manufacturing thin-film[29] solar cells. Here ultrasonic vibration is given to the PEDOT: PSS (Poly(3,4-ethylenedioxythiophene): Poly(styrene sulfonic acid) thin-film coated FTO (Fluorine-doped tin oxide) glass substrate for improving the spray coated perovskite film. At low-power ultrasonic vibration (LPUV), i.e., 5 W and 40 kHz having vertical substrate displacement of 8.7 μm, perovskite covers 64% of the substrate with 140 nm roughness.[30] On the contrary, perovskite covers only 35% of the substrate for a stationary substrate, having greater roughness of 308 nm. Moreover, it is to be noted that high-power ultrasonic vibration (HPUV), i.e., 50 W and 40 kHz having vertical substrate displacement of 57.7 μm, is not suitable for film formation as the film ruptures, decreasing the Area covered. Uniform size water/water (w/w) droplet generation is possible in a simple, easy-to-operate microfluidic device[31] between frequency 0-50 Hz, which finds wide applications in cell encapsulation, bioreactors, biocompatible storage, etc.[32] These Microfluidic devices generate w/w droplets using two chemically incompatible polymers or one polymer and one salt in water above the critical concentration in a particular temperature range. The polymers used here are poly(ethylene glycol) (PEG) and dextran (Dex). Both at low frequency of 0-5 Hz and high frequency > 40 Hz, non-uniform w/w droplets are generated, whereas between 10-35 Hz indicated the formation of uniform w/w droplets. Manipulating

droplet behavior on an inclined vibrating fiber has potential application in fog collection and dew harvesting.[32] A group of droplets moves towards the lower node (a point on the standing wave where the amplitude is minimum), maintaining a lower velocity on initiation of oscillation between two nodes. Once the droplet reaches the critical volume upon coalescing, it detaches from the fabric, thus collecting the liquid outside.[33]

Speaking generates mechanical and acoustic energy, which can assist in the production of charges in melt-blown[34] polypropylene (PP) masks incorporated with polyvinylidene fluoride-trifluoroethylene (P(VDF-TrFE)). These charge-laden melt-blown masks shows filtration efficiencies >99.9% and 90% for $PM_{2.5}$ and $PM_{0.3}$ respectively with excellent breathability (Differential Pressure < 17 Pa/ cm^2).[35] Multilayered triboelectric nanogenerator (TENG)[36,37] based face masks are also efficient in repelling the incoming viral particles by electrocution due to their innate ability to self-harvest charges during breathing, talking or other facial movements.[38,39]

Here in this work, we studied how a droplet containing pollutants or disease-causing microorganisms behaves on a porous flexible substrate while undergoing vibration due to talking, breathing, or sneezing. Due to the wetting characteristics of the fabric, the droplet will show different orientational behavior i.e. fluctuations in the droplet shape as well as footprint while undergoing oscillation at several frequencies and amplitudes. Hence, we performed the experiments using both as-purchased Eri silk (hydrophilic) and OTS-treated Eri silk which acted as the flexible porous substrate. On undergoing vibration, the micro-nano particles inside the droplet were repelled off, while some penetrated through the fabric, and the others remained on the fabric surface. Lastly, the micro-nano particles remaining on top of the porous flexible substrate and those penetrated through the substrate, were analyzed under the optical microscope and FESEM.

5.2. Experimental Methods

5.2.1. Materials

In this study, we have performed our experiments using cloth(fabric) samples that can be considered flexible porous substrates. Cloth samples commonly available in the market, such as Eri silk, were used in different forms, as mentioned in Table 5.1.

Table 5.1. Different types of porous substrates used in the current study

Sl. No.	Types of substrate	Nature of substrate
1	Pristine Eri silk	Hydrophilic
2	OTS-treated Eri silk	Hydrophobic

Different types of micro-nano particles were used to check the penetration through the flexible porous substrates, namely: Procured UV fluorescent particles (diameter: 10-20 μm) and lab synthesized silica particles (10-20 nm).

5.2.2. Experimental setup

All the experiments were carried out on a fabricated circular stage fixed to the mechanical vibrator that ran with the help of a function generator under normal diffusing conditions. Various frequency (Hz) and peak-to-peak voltage (Vpp) given to the function generator are mentioned in Table 5.2. A self-fabricated circular stage was placed above the stem of the mechanical vibrator. The sample pieces of Eri silk cloth were tightly fixed to the middle of the stage, as shown in Figure 5.1. A 4 μL droplet was placed on top of the porous substrate before giving a particular vibrational condition to the stage. The change in the droplet shape was observed with the help of the high-speed camera. The particles present in the droplet can percolate and settle on the glass substrate present at the bottom of the circular stage. These samples were characterized for the presence of UV fluorescent and silica particles using the FESEM. The temperature of the surrounding was maintained at 23 ± 2 °C and relative humidity at ~ 58 ± 2%.

Table 5.2. The experiments were performed in the following vibration range

Frequency (Hz)	Peak-to-peak voltage (Vpp)
0	0
20	10
70	10
120	10

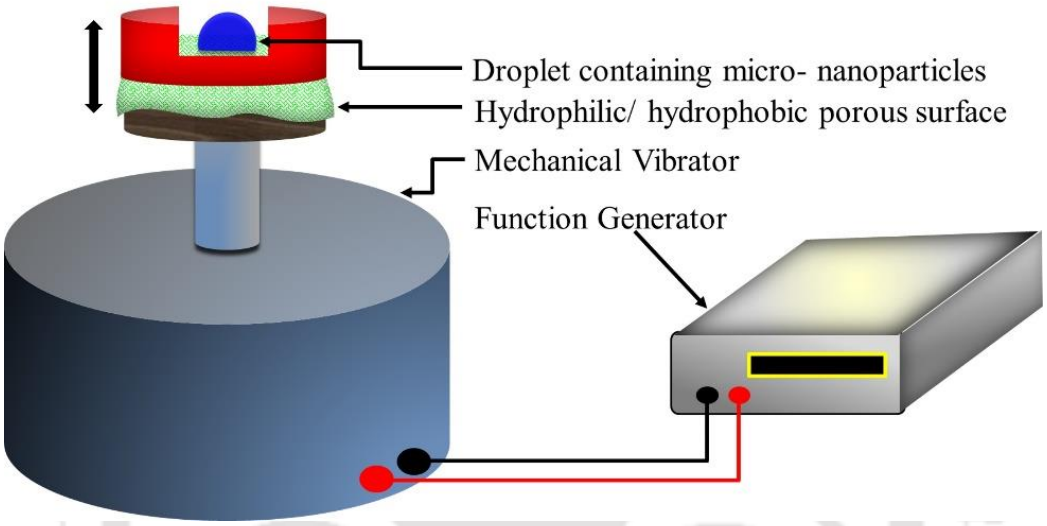

Figure 5.1. Experimental setup showing the placement of flexible porous surface to a function generator operated mechanical vibrator. The black arrow depicts the vibration direction of the stage.

5.2.3. Preparation of silica particles

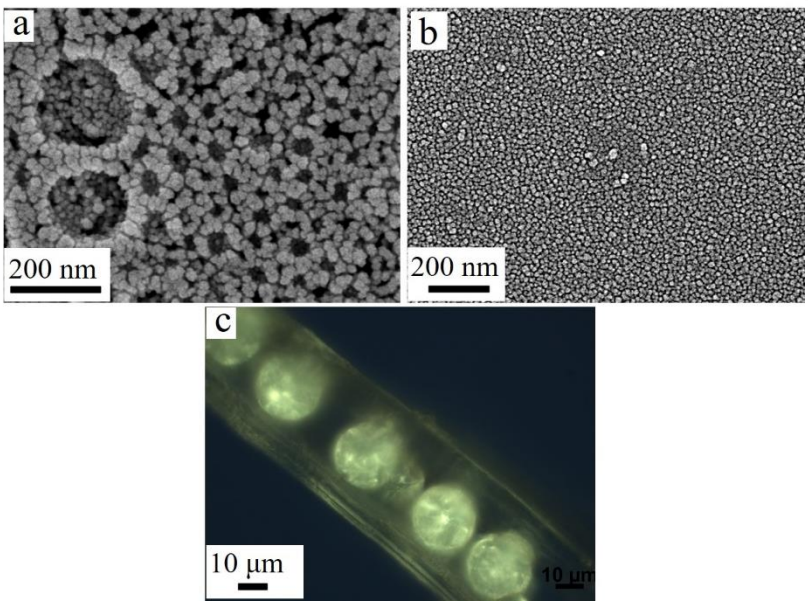

Figure 5.2. FESEM image of the lab synthesized silica particles at the (a) Periphery and (b) Centre of the deposition (c) Optical image of the as-purchased UV fluorescent particles.

6 mL methanol, 2 mL isopropanol and 50 µL tetraethyl orthosilicate (TEOS) were mixed together in a vial and sonicated for around 20 min. Further, 50 µL ammonia was further added to the preceding solution and sonicated for about 60 min. The stock solution thus prepared had silica particles, which was verified by the FESEM images (Figure 5.2). A drop of this stock solution was allowed to dry under normal condition on a clean glass slide. FESEM was performed on the deposited pattern formed on the glass slide. The particles size distribution was not uniform throughout the deposited pattern. As lots of silica particles are formed in this process, the silica particles get agglomerated to some extent which makes the particles appear bigger, rough, and non-spherical. Figure 5.2.a shows silica particles at the periphery of the deposited pattern whose size ranges from 10-30 nm due to agglomeration. However, at the center of the deposition most particles are not agglomerated and appear to have uniform size distribution as shown in Figure 5.2.b. As the stock solution contains lots of silica particles, it was diluted 100 times with DI water before it was used for the experiments.

In order to check the size of the lab synthesized silica particles, DLS was performed using the Delsa Nano instrument (Delsa Nano C; Make: M/s Beckman Coulter, Swtizerland). The stock solution was first diluted with DI water in the dilution ratio of 1:4 and then sonicated for 30 min in a sonicator before performing DLS. The DLS data in Figure 5.3 has real-time diameter on the y-axis and accumulation time on the x-axis. The accumulation time mentioned in the x-axis of the graph is the number of times the data is collected from the scattered light of the sample so that the noise contributed gets reduced during the summation/integration of the correlation function. For example, if we put this value as 70, then the software determines 70 autocorrelation functions (ACFs) and calculates 70 real-time diameters from each ACF, and finally calculates one averaged ACF from all the 70 ACFs to give the mean diameter. Moreover, this graph also makes it possible to confirm the stability of the sample, such as whether or not the particle size changes over time during the measurement. As lots of silica particles are formed and the particles have the tendency to agglomerate to form larger particles, this graph will not

only give the real-time diameter of the particles but also help us know the stability of the solution.

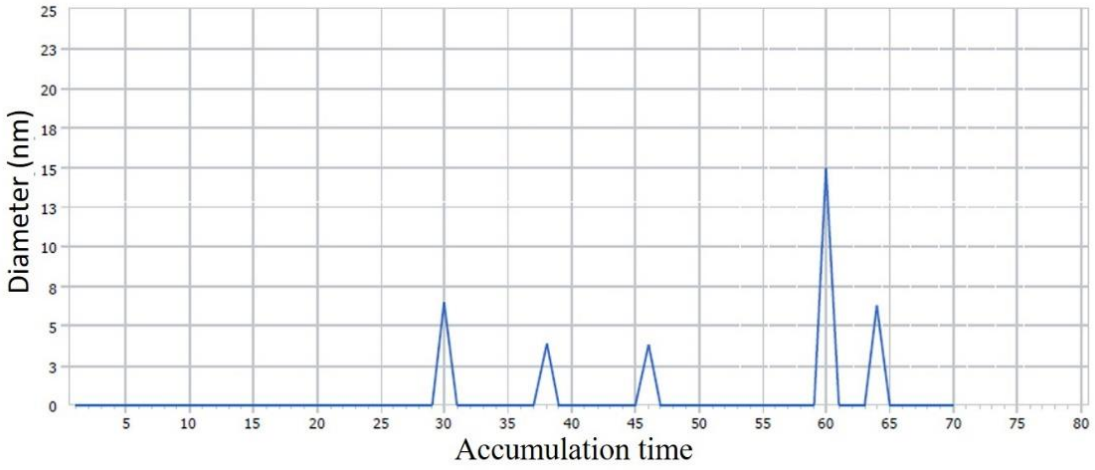

Figure 5.3. DLS graph showing the realtime diameter (nm) of lab synthesized silica particles at different accumulation time.

5.2.4. Preparation of octadecyltrichlorosilane (OTS) solution

20 μL of octadecyltrichlorosilane (OTS) was added to 10 mL toluene to prepare an OTS solution. After that, the solution was mixed properly for uniform dispersion of OTS particles in toluene by stirring for 10 min. Then the solution was heated on a hot plate at 60 ^{o}C for 30 min and gradually cooled to room temperature before being used for further experiments.

5.2.5. Preparation of hydrophobic Eri silk

The procured Eri silk cloth samples were first washed with a soap solution for 3 min to remove any dirt. Then these samples were washed with DI water and further washed with acetone for 1 min to remove any excess soap accumulated on the cloth.[40] Further, the samples were again washed with DI water to remove the acetone and then dried with nitrogen gas to remove the excess water until the cloth pieces became moist. Then, they were dried in a hot air oven at around 100 ^{o}C for 15 min to make them completely dry.

After that, the cloth was immediately transferred to the OTS solution prepared (several pieces of them) and kept for 30 min. Then these cloth samples were dipped into toluene to remove the excess OTS on the cloth. These pieces were then dried with nitrogen and finally kept in a hot air oven at 80 ^{o}C for 10 min.

5.2.6. Quantitative and quantitative analysis

The structural change experienced by the droplet during the substrate vibration was observed with the help of high-speed camera (Phantom VEO 640L, 1024X768 resolution, 1000 fps). The tracking measurements of the high-speed motion experienced by the setup were done with the inbuilt software present in the instrument. The micro-nano particles were seen under optical microscope (Carl Zeiss, Model A1MAT HAL 100) and FESEM (JSM 7610 F, JEOL, Japan), and the area coverage of the particles was calculated using the open-source software "ImageJ."

5.3 Results and Discussion

5.3.1. Generation of sine waves

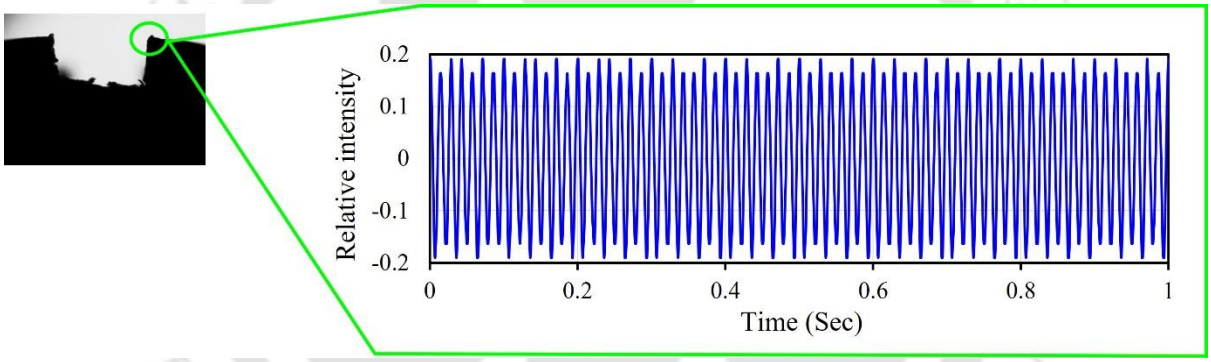

Figure 5.4. The sinusoidal waveform for 70 Hz and 10 Vpp. The high-speed video was taken at 1000 fps and 1024x768 resolution. Here 70 Hz means 70 vibrations were produced in 1 second.

The required frequency and Vpp in sinusoidal form, as mentioned in Table 5.2 was given to the function generator, thereby vibrating the circular stage, which was recorded with the help of the high-speed camera. A particular point on the circular stage was considered for tracking every frame obtained from the video. Hence, we could compose the frequency curve (at 70 Hz) with these tracking data, as shown in Figure 5.4.

5.3.2. Area covered by the penetrated particles on glass substrate

When the 4 μL droplet was placed above the flexible cloth fabric and the circular stage was made to undergo vibration, some particles penetrated through the porous substrate. These penetrated particles settle on the glass substrate placed at the bottom of the circular stage. The

FESEM images obtained from the micro-nano particle deposited glass slide were analyzed using ImageJ software to calculate the area covered by the particles. In the software the image was adjusted with the threshold function and then analysed, after that the area was calculated using the ROI Manager function. The fixed area that was considered for this analysis was 16.625 μm^2 and the data are calculated from three images from three different trials of the experiments. The values of the area obtained from all three images are used to calculate the error bar via the standard deviation method in Microsoft excel.

The area covered in the case of the treated porous substrate is more than that of the untreated porous substrate as shown in area vs frequency graph (Figure 5.5). The untreated porous substrate being hydrophilic absorbs the droplet and the particles immediately due to capillary motion. Most of the particles remain between the threads instead of being screened out of the porous substrate. Whereas the OTS-treated substrate being hydrophobic, tends to repel the droplet and the particles away from porous substrate.

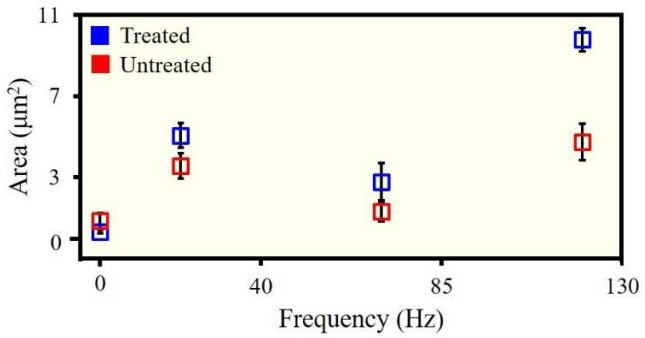

Figure 5.5. The graphs show the area (μm^2) covered by the lab synthesized silica particles (10-20 nm in diameter) on the glass substrate vs. frequency (Hz) for four different frequencies, namely, 0 Hz, 20 Hz, 70 Hz, and 120 Hz, all at 10 Vpp. The blue line represents OTS-treated Eri silk flexible porous fabric, and the red line indicates as-purchased Eri silk flexible porous fabric.

Moreover, it was observed that the nanoparticle penetration increases initially with increasing frequency for both untreated and OTS-treated porous substrates. An increase in micro-nano particle penetration means an increase in the area covered by them on the glass substrate, as shown in Figure 5.5. However, a sudden drop in area occurs at 70 Hz as the droplet reaches its resonance point, and then most particles are thrown away. After the resonance point, the droplet gains a steady oscillation, and with increasing frequency, the area covered by the

micro-nano particles starts rising again. The FESEM images of particle coverage on the glass substrate are shown in Figure 5.6. The high resolution FESEM images in Figure 5.7 clearly proves that untreated porous substrate absorbs most of the particles in between the threads of the fabric allowing only few particles to pass through. Whereas the OTS-treated substrate being hydrophobic, tends to repel the droplet and the particles away from porous substrate. However, some silica particles further get agglomerated due to the vibrational effect and finally due to their own weight pass through the porous substrate and settle on the glass substrate below it.

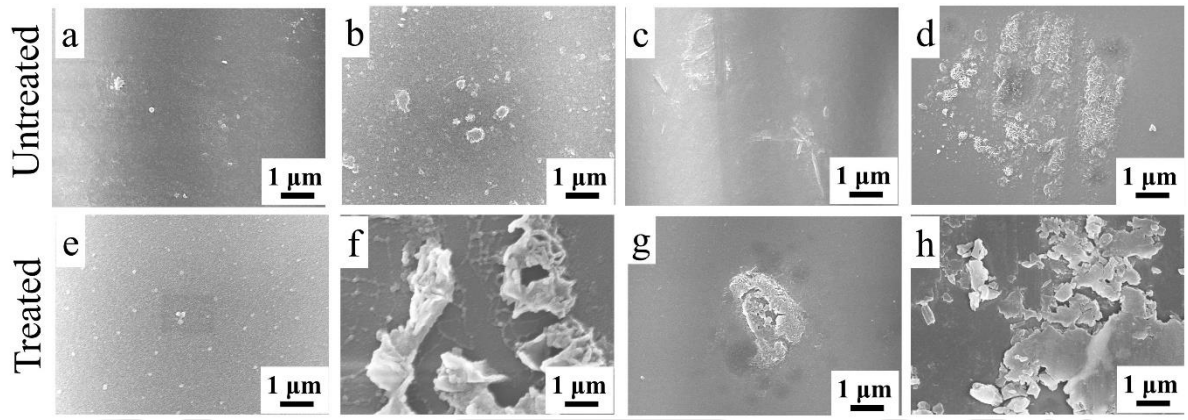

Figure 5.6. FESEM images of particles on glass substrates in case of lab synthesized silica particles (10-20 nm in diameter). The first row depicts the images for as-purchased Eri silk flexible porous fabric and the second row shows the images for OTS-treated Eri silk flexible porous fabric for frequencies: (a), (e) 0 Hz and 0 Vpp; (b), (f) 20 Hz and 10 Vpp; (c), (g) 70 Hz and 10 Vpp; (d), (h) 120 Hz and 10 Vpp.

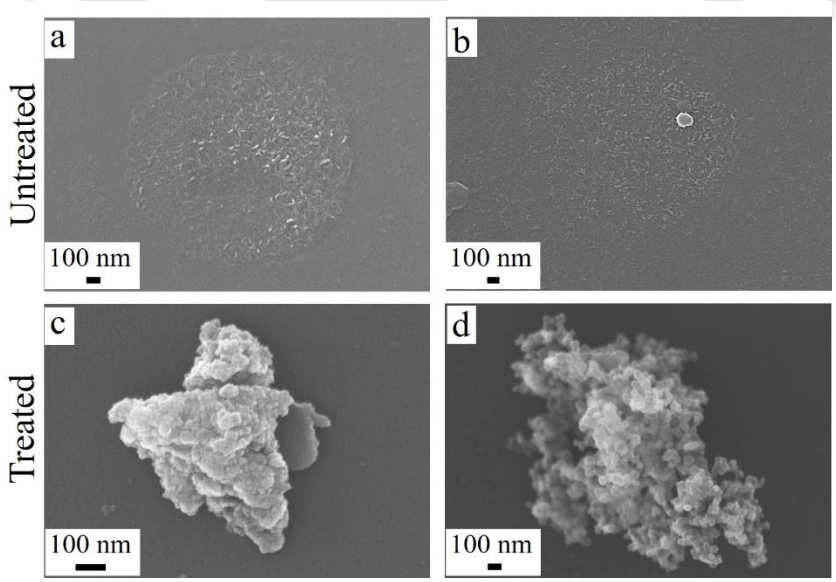

Figure 5.7. High resolution FESEM images of particles on glass substrate in case of lab synthesized silica particles (10-20 nm in diameter) (a), (b) depicts the images for as purchased Eri silk fabric and (c), (d) depicts the images for treated Eri silk fabric.

5.3.3. Area covered by particles on flexible porous substrate

The area covered by UV fluorescent particles (diameter: 10-20 μm) on flexible porous substrate was observed under the optical microscope, and for lab synthesized silica particles (10-20 nm) FESEM was done. The images obtained were analyzed using ImageJ to calculate the area covered by the particles above the substrate. The fixed area of the image used for the analysis was 12.21×10^5 μm^2 and the data are calculated from three images from three different trials of the experiments. The values of the area obtained from all three images are used to calculate the error bar via the standard deviation method in Microsoft excel. The area covered on the untreated fabric is less than that of the OTS-treated fabric because untreated fabric being hydrophilic in nature absorbs the droplet instantly, as shown in Figure 5.8. Hence, most particles move inside to the inner grooves of the thread due to capillary action. However, most particles remain on top of the fabric surface without vibration. Giving vibration to the flexible substrate commences movement of the particles along with the droplet, thus letting particles to move inside the fabric quickly and easily. However, at 70 Hz i.e., at the resonance point, the outward moving force on the particles is enough to prevent them from entering the grooves of the fabric. Moreover, 20 μm particles do not have enough energy to throw themselves away, so they settle on the fabric surface, thus increasing the area covered by the particles, as shown in Figure 5.9. Increasing the frequency above the resonance point decreases the amplitude of the droplet, which reduces the particles' penetration capacity, thus decreasing the area covered by the particles on the fabric.

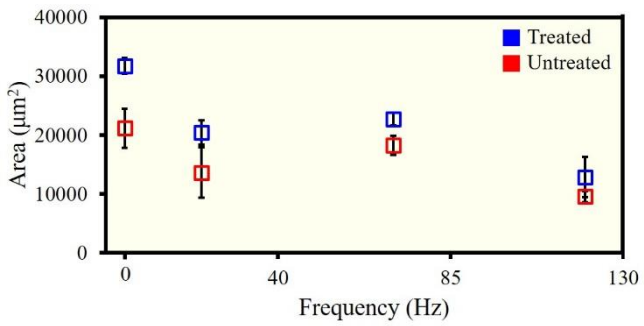

Figure 5.8. The graphs show the area (μm^2) covered by the UV fluorescent particles (10-20 μm in diameter) on the flexible porous substrate vs. frequency (Hz) for four different frequencies,

namely, 0 Hz, 20 Hz, 70 Hz, and 120 Hz, all at 10 Vpp. The blue line represents OTS-treated Eri silk flexible porous fabric, and the red line indicates as-purchased Eri silk flexible porous fabric.

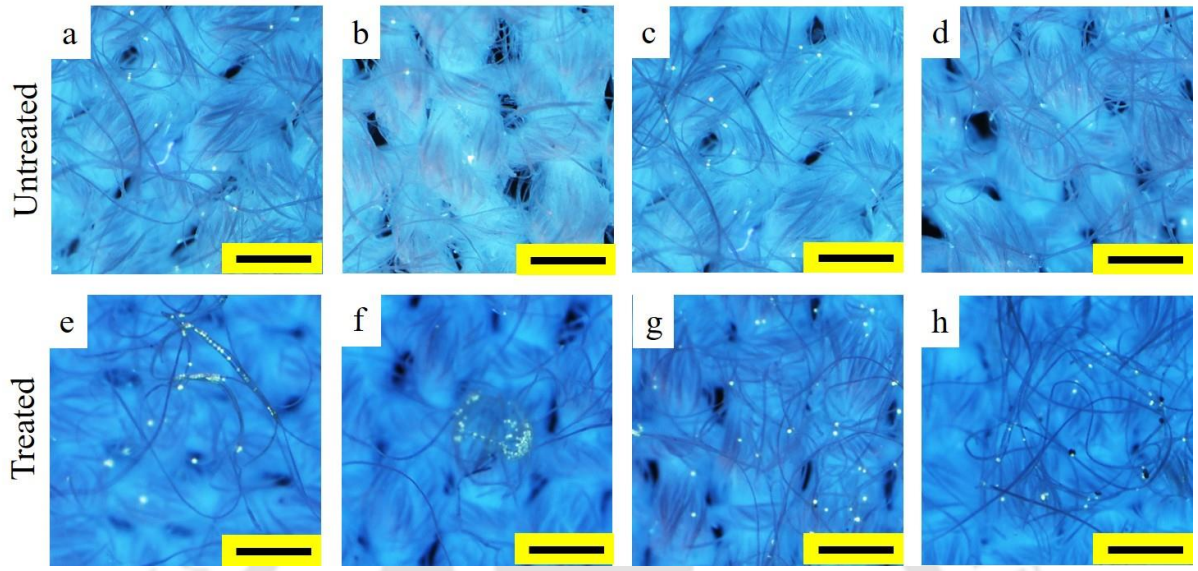

Figure 5.9. Optical images of particles on the flexible porous substrate in case of UV fluorescent particles (10-20 μm in diameter). The first row depicts the images for as-purchased Eri silk flexible porous fabric and the second row shows the images for OTS-treated Eri silk flexible porous fabric for frequencies: (a), (e) 0 Hz and 0 Vpp; (b), (f) 20 Hz and 10 Vpp; (c), (g) 70 Hz and 10 Vpp; (d), (h) 120 Hz and 10 Vpp. The scale bar for all the images is 500 μm.

5.4. Conclusion

In conclusion, we have prepared nanometer-sized silica particles with diameter in the range of 10-20 nm. We investigated how a droplet containing micro-nano particles (pollutants or disease-causing microorganisms) behaves due to vibration (which can be caused be talking, breathing, or sneezing) on different types of flexible porous substrates. We examined that most particles are absorbed by hydrophilic flexible substrate due to capillary action, which would be a potential threat to the person as these particles will slowly percolate inside. However, in the case of a hydrophobic flexible substrate, the particles, instead of percolating inside, either stay on the fabric surface or are repelled off. Thus, the surface properties of the flexible porous substrate play a crucial role in the percolation actions of various types of particles.

References

[1] T. Hunt, *Sci. Am.* **2018**.

[2] T. Hunt, J. W. Schooler, *Front. Hum. Neurosci.* **2019**, *13*, 1–16.

[3] A. J. Brisben, S. S. Hsiao, K. O. Johnson, *J. Neurophysiol.* **1999**, *81*, 1548–1558.

[4] T. Oroszi, M. J. G. van Heuvelen, C. Nyakas, E. A. van der Zee, *F1000Research* **2020**, *9*, F1000 Faculty Rev-619.

[5] J. M. W. Brownjohn, X. Zheng, in *Proc.SPIE*, **2001**.

[6] R. Tsubaki, N. Hosoda, H. Kitajima, T. Takanashi, *Zoolog. Sci.* **2014**, *31*, 789–794.

[7] P. S. M. Hill, *Naturwissenschaften* **2009**, *96*, 1355–1371.

[8] P. S. M. Hill, *Curr. Biol.* **2015**, *25*, R1046–R1047.

[9] P. S. M. Hill, *Am. Zool.* **2001**, *41*, 1135–1142.

[10] X. Dai, W. Zhang, J. Zhang, G. Xin, X. Wang, *Case Stud. Therm. Eng.* **2022**, *30*, 101732.

[11] N. T. Chamakos, G. Karapetsas, A. G. Papathanasiou, *Colloids Surfaces A Physicochem. Eng. Asp.* **2016**, *511*, 180–189.

[12] Y. Liu, C.-H. Choi, *Colloid Polym. Sci.* **2013**, *291*, DOI 10.1007/s00396-012-2751-6.

[13] R. N. Wenzel, *Ind. Eng. Chem.* **1936**, *28*, 988–994.

[14] J. B. Boreyko, C. H. Chen, *Phys. Rev. Lett.* **2009**, *103*, 174502.

[15] K. Balani, R. G. Batista, D. Lahiri, A. Agarwal, *Nanotechnology* **2009**, *20*, 305707.

[16] A. B. D. Cassie, S. Baxter, *Trans. Faraday Soc.* **1944**, *40*, 546–551.

[17] J. Genzer, K. Efimenko, *Biofouling* **2006**, *22*, 339–360.

[18] Y. T. Cheng, D. E. Rodak, *Appl. Phys. Lett.* **2005**, *86*, 144101.

[19] J. R. Friend, L. Y. Yeo, *Encycl. Surf. Colloid Sci.* **2013**, 1–11.

[20] L. M. Hocking, *J. Fluid Mech.* **1987**, *179*, 267–281.

[21] J. Friend, L. Y. Yeo, *Rev. Mod. Phys.* **2011**, *83*, 647–704.

[22] C. Li, Z. Shi, H. Xiao, X. Ye, *Phys. Fluids* **2020**, *32*, 062106.

[23] R. Borcia, I. D. Borcia, M. Bestehorn, *Langmuir* **2014**, *30*, 14113–14117.

[24] A. Rahimzadeh, M. Eslamian, *Int. Commun. Heat Mass Transf.* **2017**, *83*, 15–22.

[25] S. Chandrasekhar, *Proc. London Math. Soc.* **1959**, *s3-9*, 141–149.

[26] L. R. W., *Nature* **1898**, *58*, 121–122.

[27] F. Zabihi, M. Eslamian, in *2015 IEEE 42nd Photovolt. Spec. Conf.*, **2015**, pp. 1–3.

[28] F. Zabihi, M.-R. Ahmadian-Yazdi, M. Eslamian, *Nanoscale Res. Lett.* **2016**, *11*, 71.

[29] M. Eslamian, *Prog. Org. Coatings* **2017**, *113*, 60–73.

[30] M. Habibi, M. Eslamian, F. Soltani-Kordshuli, F. Zabihi, *J. Coatings Technol. Res.* **2016**, *13*, 211–225.

[31] G. M. Whitesides, **2006**, *442*, DOI 10.1038/nature05058.

[32] Y. Zou, J. Song, X. You, J. Yao, S. Xie, M. Jin, X. Wang, Z. Yan, G. Zhou, L. Shui, *ACS Appl. Mater. Interfaces* **2019**, *11*, 21227–21238.

[33] A. Bick, F. Boulogne, A. Sauret, H. A. Stone, *Appl. Phys. Lett.* **2015**, *107*, 181604.

[34] J. Drabek, M. Zatloukal, *Phys. Fluids* **2019**, *31*, 091301.

[35] D. Chen, L. Tang, Y. Wang, Y. Tan, Y. Fu, W. Cai, Z. Yu, S. Sun, J. Zheng, J. Cui, G. Wang, Y. Liu, H. Zhou, *ACS Appl. Mater. Interfaces* **2022**, *14*, 17774–17782.

[36] M. Karmacharya, S. Kumar, O. Gulenko, Y. K. Cho, *ACS Appl. Bio Mater.* **2021**, *4*, 3891–3908.

[37] G. Q. Gu, C. B. Han, C. X. Lu, C. He, T. Jiang, Z. L. Gao, C. J. Li, Z. L. Wang, *ACS Nano* **2017**, *11*, 6211–6217.

[38] B. Ghatak, S. Banerjee, S. B. Ali, R. Bandyopadhyay, N. Das, D. Mandal, B. Tudu, *Nano Energy* **2021**, *79*, 105387.

[39] G. Liu, J. Nie, C. Han, T. Jiang, Z. Yang, Y. Pang, L. Xu, T. Guo, T. Bu, C. Zhang, Z. L. Wang, *ACS Appl. Mater. Interfaces* **2018**, *10*, 7126–7133.

[40] P. Gogoi, S. K. Singh, A. Pandey, A. Chattopadhyay, P. S. Gooh Pattader, *ACS Appl. Bio Mater.* **2021**, *4*, 7921–7931.

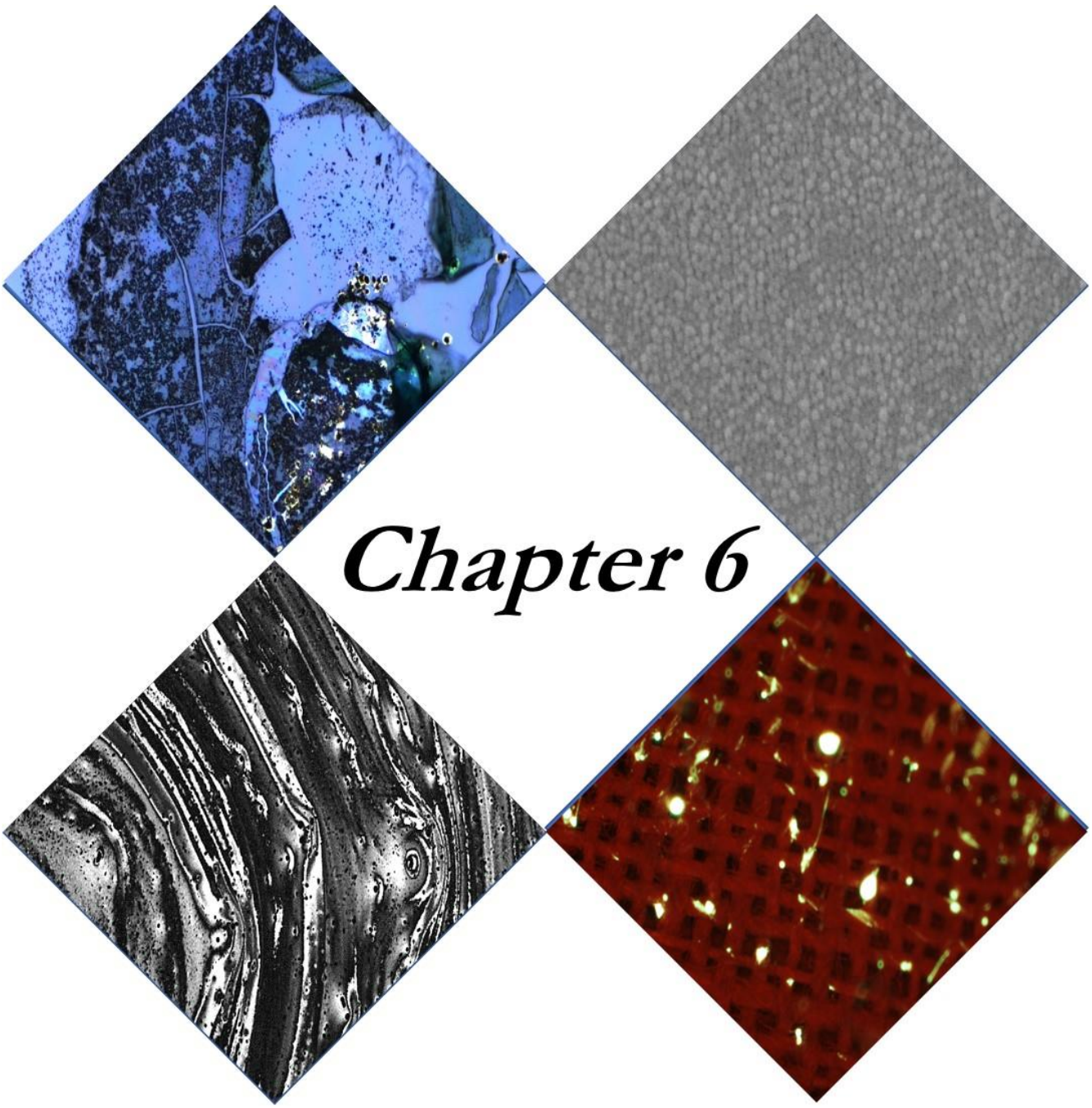

Chapter 6

Chapter 6
Conclusion and scope for future work

6.1 Conclusion

The thesis focuses on exploring the multi-dimensionality of different types of surfaces such as hydrophilic and hydrophobic substrates. Based on the various types of substrates, many different patterns can be obtained by the coffee stain effect phenomena. Moreover, the water-repelling nature of the hydrophobic substrate can be a boon in different types of industries such as electronics, biomedical, manufacturing etc. to name a few. The detailed conclusion of the individual technical chapters is elaborated below.

The conventional idea is that the evaporation of a sessile droplet containing colloidal particles leaves a ring-like stain on the surface due to the deposition of the particles near the periphery of the droplet footprint. However, in **Chapter 2** we explored how completely well-defined deposition patterns, such as disk-like, coffee ring, irregular patterns can be obtained due to the variation in the solute–solvent–substrate interactions, even though the droplet geometry and the deposition time scale are similar. To substantiate a deposition zone diagram with basically four zones was plotted which maps the deposition patterns based on the deposition time scale and a characteristic geometric length scale that accounts for the "space" available for the distribution of solute particles on the substrate. Novelty here was in identifying a specific zone where the solute-solvent-substrate interactions play a crucial role and other deposition zones where it is governed solely by the geometry of the droplets or by the solvent-substrate interaction. For instance, in Zone I due to the interactions among solute, solvent and the substrate different deposition patterns such as uniform disk-like and coffee ring is seen even though the droplet shape geometry and deposition time is same. Moreover, these experiments will give a better insight into the phenomenon occurring inside a microdroplet when it undergoes evaporation in a particular

appointed condition. It was also observed that contact line pinning due to the capillary flow of particles towards the periphery of the droplet is one of the most important criteria for coffee ring formation. Further, after performing experiments on slippery surfaces we could conclude that slippery surfaces inhibit the contact line pinning leading to aggregation of the particles forming disc-like deposition. Finally, by using lower boiling point solvents the surrounding environment of the droplet was regulated, which further regulated the Marangoni flow at the surface. This phenomenon changed the internal inertial flow field of the particles inside the droplet thus manipulating the deposition pattern. This study is expected to be useful for carrying out fundamental scientific research and in industrial applications that require specific patterns of particles from colloidal suspensions.

In **chapter 3**, our first finding says that the efficiency of a mask predominantly depends on the surface properties of the fabric used in making a mask. Due to the hydrophobic nature of N95 mask (contact angle of water ~127.4^{0}) the fractional area covered by the incoming droplets on the outer surface of the mask was only ~6%, whereas for a hydrophilic cloth mask (contact angle of water <90^{0}) the fractional coverage was more than 30%. Hence, we converted the locally available hydrophilic Eri silk fabric into hydrophobic Eri silk fabric by depositing a nanometer-thick coating of OTS (octadecyltrichlorosilane) without compromising the breathability of the mask. The modified hydrophobic Eri silk showed an excellent hydrophobic property with a contact angle of water of 143.7^{0} which could repel back the incoming droplets without wetting the fabric and also allowed the easy flow of air through the three-layered treated Eri silk mask (breathability reduced by only 22% wrt the pristine Eri silk when compared to 59% reduction by N95 mask wrt pristine Eri silk). This makes the modified silk mask a better alternative to the N95 mask and can be made easily available to the common masses.

Similarly, in **Chapter 4**, the as-purchased hydrophilic bandages (cotton, 12-ply gauze bandage, crepe bandage) were treated with OTS to obtain modified hydrophobic bandages. These

modified bandages showed a water contact angle greater than 130° making them superhydrophobic in nature. The water droplet remains seated on the bandage surface for more than 2 h before being completely evaporated which differed from the as-purchased bandages (water gets absorbed by the surface). Moreover, for the modified crepe bandage we saw a reduction in contact angle of water by only 17% after repeatedly washing upto 10 times. The commercially available bandaid appears to be hydrophobic in nature but the hydrophobic property deteriorated after three washing (i.e., when it comes in contact with water), but the OTS treated bandaid retained its hydrophobicity even upto eight washings. The serous liquid produced by the wound in the normal healing process would remain intact on the wound bed due to the hydrophobic environment created rather than being absorbed by the bandage, which would make the wound healing process much faster.

In **Chapter 5**, we examined how most of the micro-nano particles present inside the droplet percolated through the porous surface, while some are repelled off and some get absorbed by the fabric due to capillary action. For example, if a mask is stitched with this hydrophilic fabric most particles will be absorbed by the fabric which would be a potential threat to the person, as these particles will slowly percolate inside to the inner side of the mask causing diseases. However, in the hydrophobic fabric we see that although most particles are repelled off, some sit on the fabric surface while the others percolate through the fabric.

6.2 Future Scopes

Molecular modification of substrates is a versatile field that can be further investigated for numerous theoretical studies and experimental work. Some of the future scope are as follows:

1. To check the variations in coffee stain effect by parametrical modification of either the substrate or the solution, such as deposition of droplets on a thermally gradient surface or using colloidal solutions which are hotter or colder than the ambient room temperature, and also by mixing the colloidal solutions with surfactant. It would be very interesting to see the coffee ring

patterns for the above mentioned conditions as that would give ample insight to the researchers about selecting the appropriate conditions to attain the desired pattern.

2. By virtue of coffee stain effect and following the technique of 3D printing, fabrication of various micron-sized industrial, electronics and biomedical 3D structures can be made possible with layer by layer deposition. Comprehensible progress by this method would be a boon for the medicine industry as this would be a cost friendly initiative.

3. The phenomena of coffee ring effect can be used as an analytical technique for the detection of vector-borne and microbial diseases, as the length scales of the disease pathogens of vector-borne diseases like malaria, dengue and of microbial diseases like tuberculosis are of the order of hundreds of nanometers to a few micrometres. So effective isolation and concentration of these pathogens from body fluid would be easy and accurate. Further, this technique would also be a low-cost method, thus soothing the burden of the developing countries in the policy making to improve public health.

4. Low cost paper based fast and easy detection sensors that could check the turbidity of water. Water bodies near the industrial towns are heavily polluted thus causing a severe threat to the aquatic ecosystem due to bioaccumulation of harmful chemicals. A simple onsite molecularly modified paper-like sensor can be fabricated that will help in monitoring the water quality at all times.

APPENDIX-A

APPENDIX-A

A.1. Substrate cleaning protocol (Chapter 2)

The substrate used for carrying out the series of evaporation processes was smooth commercially available silicon wafers. The silicon wafer was cleaned, in order to make it dust-free as well as to get rid of organic contaminants, following a series of steps before the experiments were carried out. As all the steps should be done in a dust-free environment, which was usually done in a laminar flow chamber. The steps used for cleaning the silicon wafer, in brief, are sonication with sodium dodecyl sulfate (SDS) for 30 min followed by washing with deionized (DI) water. The substrates were then immersed in acetone for 30 min at 60 °C followed by immersion in ethanol at 60 °C for 30 min. After that, the samples were washed with DI water, followed by cleaning using a solution of DI water-ammonia-hydrogen peroxide in the ratio of 5:1:1 at 60 °C for 30 min and then thorough washing with DI water. Finally, the samples were immersed in Piranha solution (concentrated sulphuric acid: hydrogen peroxide, in the ratio of 4:1) for 30 min and then rinsed carefully with DI water for 3-4 min. The silicon wafers were stored under DI water immediately after cleaning so that the dust does not come in contact with silicon wafer. The cleaned substrates were then taken out of the DI water and dried under the clean stream of nitrogen just before the experiment.

APPENDIX-A

A.2. Additional images of the typical deposition from another set of experiments (Chapter 2)

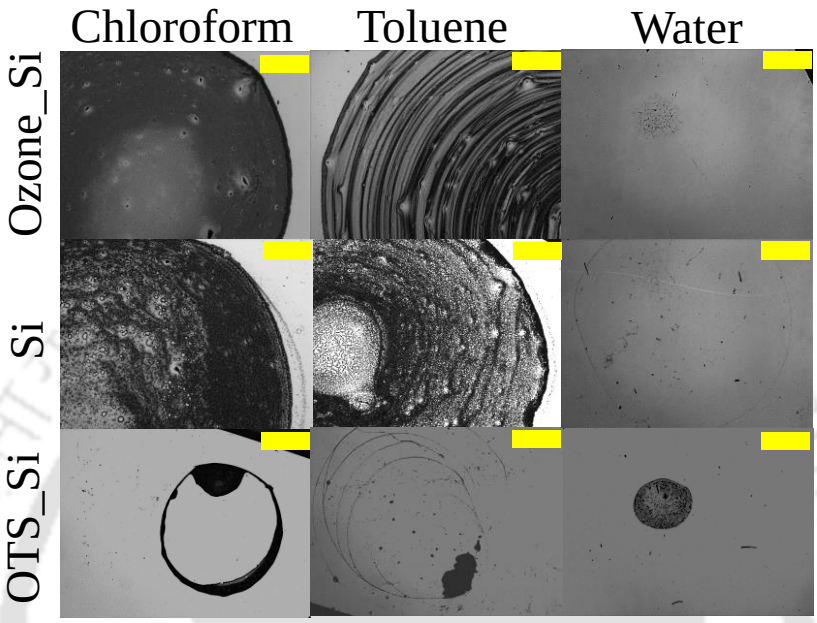

Figure A.2.1. Optical images of the deposited patterns of Nile red after complete evaporation. The dye concentration was 1 mg/mL for all the solutions. All scale bars represent 1mm.

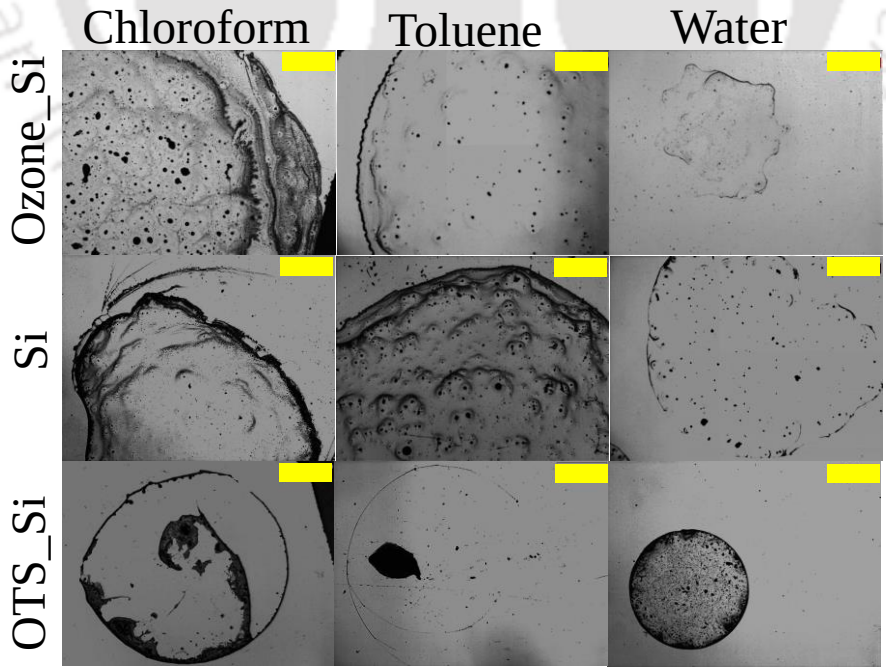

Figure A.2.2. Optical images of the deposited patterns of fluorescein after complete evaporation. The dye concentration was 1 mg/mL for all the solutions. All scale bars represent 1mm.

APPENDIX-A

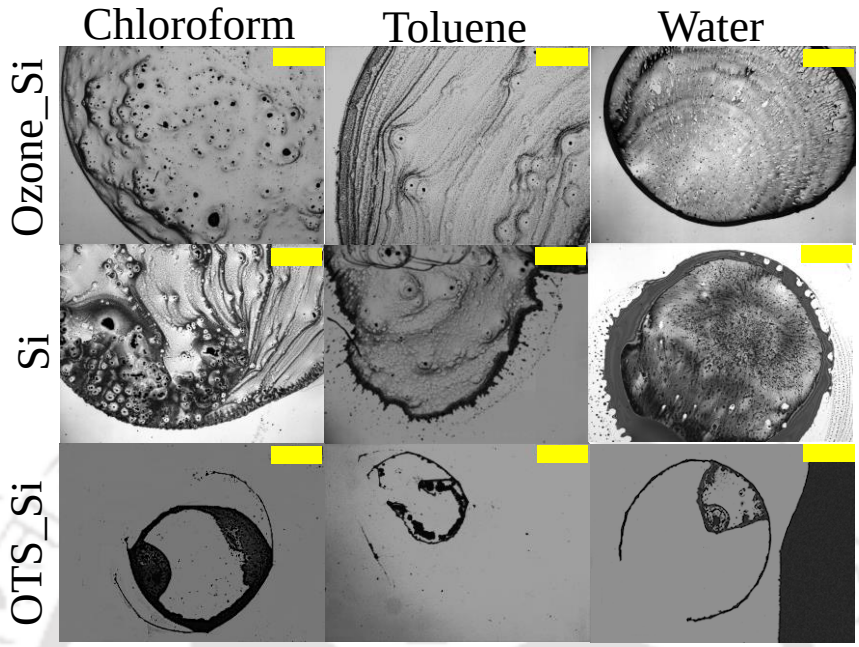

Figure A.2.3. Optical images of the deposited patterns of fluorescein Na salt after complete evaporation. The dye concentration was 1 mg/mL for all solutions. All scale bars represent 1 mm.

A.3. Graphs showing pore size distribution of different types of mask (Chapter 3)

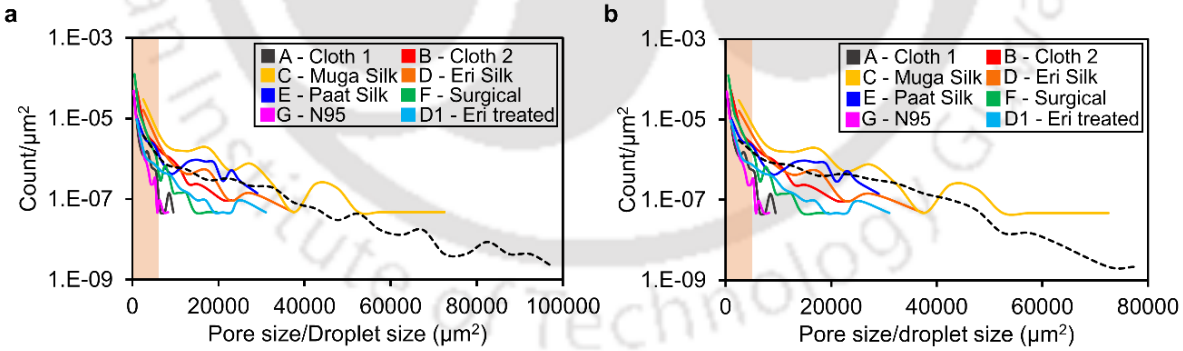

Figure A.3.1. Graphs showing the pore size distribution of all types of masks used herein. The Black dashed line is the droplet size distribution plot for the value of x : a, 5 cm b, 15 cm. The experimental set-up is shown and x is denoted in Figure 3.6a (Chapter 3).

APPENDIX-A

A.4. FESEM images of different types of bandages (Chapter 4)

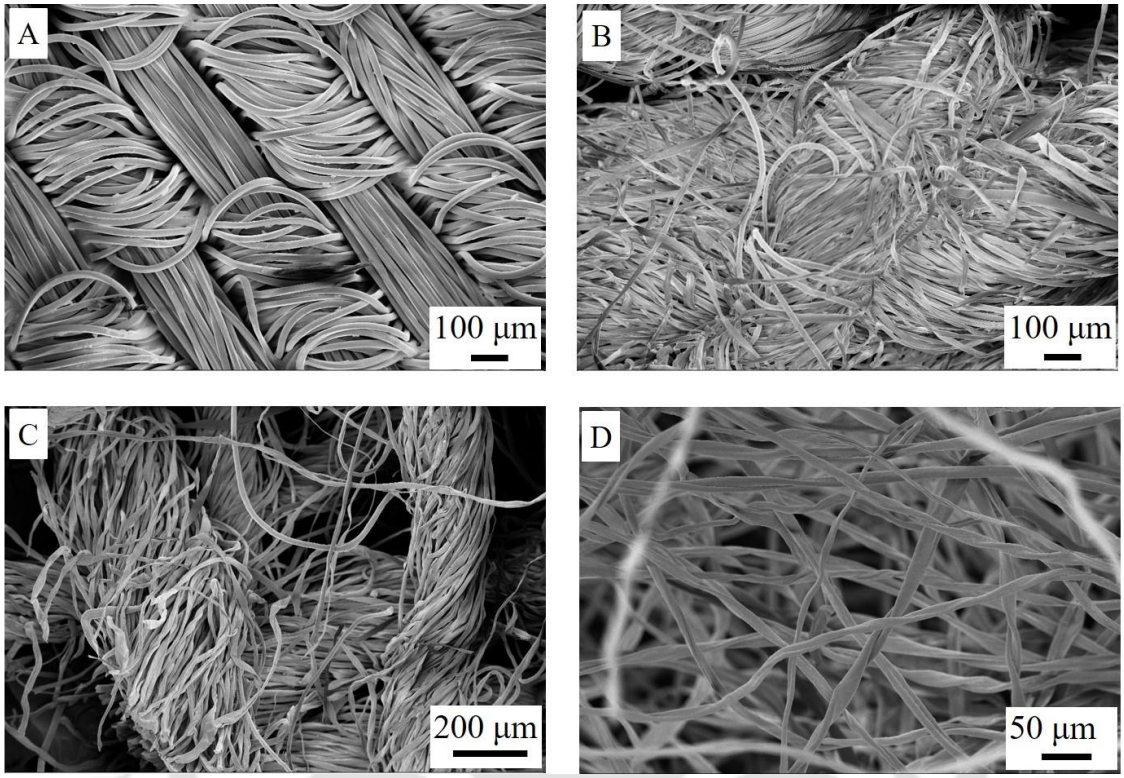

Figure A.4.1. FESEM images of different types of bandages: (A) Bandaid, (B) Crepe bandage, (C) 12-ply gauge bandage and (D) Cotton.

APPENDIX-B

APPENDIX-B

B.1. American Society for Testing and Materials

The American Society for Testing and Materials (ASTM) is a globally recognised non-profit international standards organization in which producers, users, consumers, and representatives of government and academia develop, deliver and publish voluntary consensus technical international standards for a wide variety of materials, products, systems, and services, for consideration and use worldwide.[1] Presently over 12,000 ASTM standards (test methods, specifications, classifications, guides and practices) are used worldwide to improve product quality, enhance health and safety, strengthen market access and trade, and build consumer confidence.[2] In 2001, the name ASTM was changed to "ASTM International."

B.2. Contact Angle Goniometer

A contact angle goniometer is an instrument used to qualitatively measure the contact angle of any droplet placed on a substrate.[3] This instrument helps in the indirect measurement of the wettability of the substrate, thus determining whether the surface has a hydrophilic or hydrophobic characteristic. The contact angle is the angle formed by the liquid at the phase boundary where the liquid, gas/air, and solid/substrate intersect.[4] The three forces of the interfacial tension at the phase boundary control the shape of the droplet, which is determined by the Young-Laplace equation,[5] given as

$$\gamma_{sg} = \gamma_{sl} + \gamma_{lg} cos\theta_y$$

APPENDIX-B

Where,

θ is the contact angle,

γ_{sg} is the surface free energy of the solid/substrate,

γ_{sl} is the interfacial tension between solid/substrate and liquid

γ_{lg} is the surface tension of the liquid

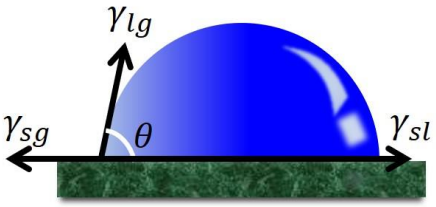

Figure B.2.1. The schematic shows a droplet on a solid substrate with the three interfacial tension forces at the phase boundary described by Young's equation.

B.3. Dynamic Light Scattering

DLS (also known as Photon Correlation Spectroscopy or Quasi-Elastic Light Scattering) is one of the most popular measurement techniques for particle size analysis down to 1 nm diameter. It is based on the principle of Brownian motion,[6] where particles dispersed in a liquid move randomly in all directions.[7] As the particles are constantly colliding with solvent molecules, these collisions cause a certain amount of energy to be transferred for inducing particle movement. The energy transferred is more or less constant which helps the smaller particles to move at higher speeds than larger particles. If all the parameters influencing particle movement are known and by measuring the speed of the particles, we can determine the hydrodynamic diameter using the Stokes-Einstein equation.[8,9] In the instrument, laser light[10] is used to illuminate the sample and the fluctuations of the scattered light by the particles are detected at a known scattering angle θ over time by a fast photon detector. The Stokes-Einstein equation is given as:

APPENDIX-B

$$D = \frac{k_B T}{6\pi\eta R_H}$$

Where,

k_B is Boltzmann constant [m²kg/Ks²]

T is temperature (K)

η is viscosity [Pa.s]

R_H is hydrodynamic radius [m]

D is translational diffusion coefficient [m²/s] i.e. "speed of the particles"

B.4. Ellipsometry

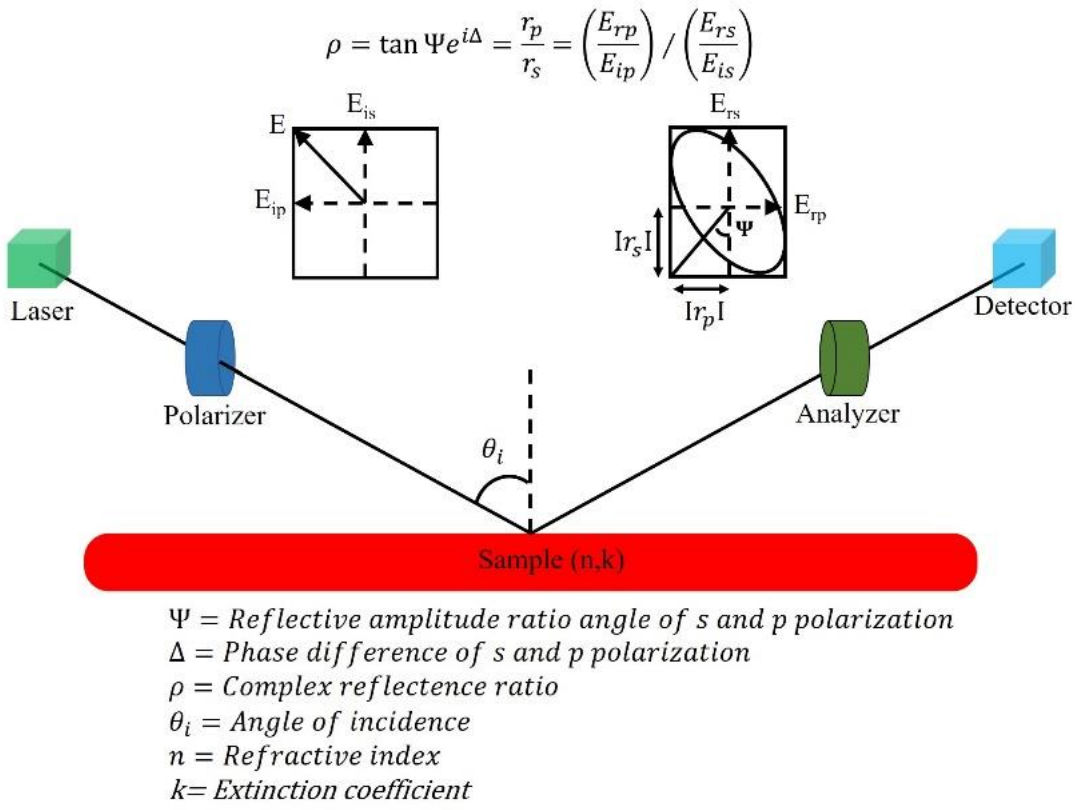

Figure B.4.1. Working principle of Ellipsometer

APPENDIX-B

Ellipsometry is a non-destructive, non-contact and non-invasive optical technique used to measure the dielectric properties (thickness, complex refractive index, dielectric function tensor) of a thin film.[11] It is called "ellipsometry" because in this process linearly polarized incident light is changed into elliptically polarized light. Ellipsometry measures the change in polarization of the incident light beam that interacts i.e., reflects, absorbs, scatters, or transmits from the sample material.[12] The polarization change is given as amplitude ratio, Ψ, and the phase difference, Δ.

B.5. Field Emission Scanning Electron Microscopy

FESEM is a microscope that helps to exhibit the microscopic features of any material by zig-zag scanning with the help of a focussed electron (negatively charged) beam.[13] The primary electrons liberated from the field emission source are accelerated in a high electrical field gradient while passing through different electromagnetic lenses and apertures placed in high vacuum conditions. These primary electrons get focused to produce a narrow scan electron beam that bombards the material to emit secondary electrons from each spot on the material.[14] The angle and velocity of these secondary electrons relate to the surface structure of the object. The detector collects the secondary electrons and produces an electronic signal that is amplified and transformed into a video scan image that can be seen on a monitor.

B.6. Fourier Transform Infrared Spectroscopy

Fourier Transform Infrared Spectroscopy measures the infrared region (longer wavelength and a lower frequency than visible light) of the electromagnetic radiation spectrum. When the object is submitted to infrared radiation (IR), it transmits the output light of an infrared spectrum. The IR spectrum is a graph whose horizontal axis represents frequency (wavelength), and the vertical axis represents infrared light absorbance by the substance. The bonds between different

elements can absorb the IR energy at various wavelengths measured to determine the molecular composition and structure of the material. Unknown materials, additives within a polymer, surface contamination on a material, etc. can also be identified by searching the spectrum against a database of reference spectra. The term Fourier-transform infrared spectroscopy originated from the fact that the mathematical process i.e., Fourier transform is required to convert the raw data into the actual spectrum.

B.7. Function generator

A function generator is a signal source capable of producing different types of output waveforms such as sine waves, triangular waves, square waves, and saw tooth as its output signal. The frequencies of such waveforms may be adjusted from a fraction of a hertz to several hundred kHz. Function generators are usually of two types: analog and digital. Analog function generators are cost-effective, simple to use and amplitude and frequencies are easily adjustable. Whereas the digital function generator has advantages such as high accuracy and stability.

B.8. High-speed camera

A High-speed camera[15] is similar to any other video camera that focuses visible light onto an image sensor, turning the image into an electronic and recordable medium. It can capture fast-moving images with exposures of less than 1/1,000 seconds or frame rates above 250 frames per second (fps). The fast-moving objects are recorded as photographic images onto a storage medium that can be played back in slow motion. Earlier high-speed cameras used film to record the high-speed events, but with technological advancement, recording is possible with electronic devices which use either a charge-coupled device (CCD) or a complementary metal-oxide-semiconductor (CMOS) active pixel sensor.[16]

APPENDIX-B

B.9. Octodecyltrichlorosilane

Octadecyltrichlorosilane[17] is an organosilicon chemical used mainly in industries such as electronics, clothing, etc., to form self-assembled monolayer thin films on different types of substrates like silicon dioxide,[18] glass,[19] flexible porous substrates,[20] etc. The structural chemical formula is $CH_3(CH_2)_{17}SiCl_3$, which has an amphiphilic part consisting of a long-chain alkyl group ($C_{18}H_{37}$–) and a polar head group ($SiCl_3$–).OTS is flammable, reacts with water readily, and is sensitive to air.

B.10. Optical microscopy

An Optical microscope, also called a light microscope, uses visible light to magnify an object which is too small to be seen with an unaided eye.[21,22] It has objective lenses that focus light and help to magnify the object. These lenses are aligned in a specific manner to bend light for efficient magnification of the image. The object is further magnified with an eyepiece to allow the user for easy detection with the naked eye.

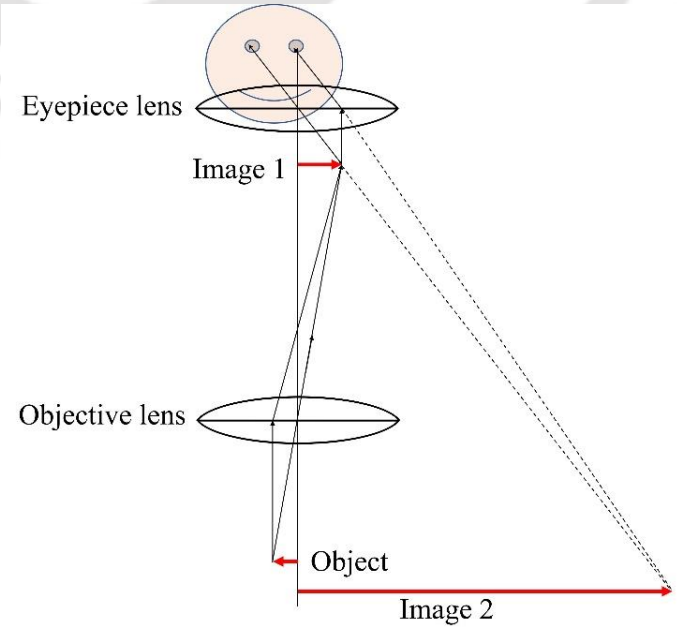

Figure B.10.1. Working principle of optical microscope

APPENDIX-B

References

[1] Institute of Medicine (US) Council on Health Care Technology, Goodman C, eds., *Medical Technology Assessment Directory: A Pilot Reference to Organizations, Assessments, and Information Resources*, National Academies Press, Washington D.C., **1988**.

[2] American Society for Testing Materials., *Proc. - Am. Soc. Test. Mater.* **1945**.

[3] M. Vuckovac, M. Latikka, K. Liu, T. Huhtamäki, R. H. A. Ras, *Soft Matter* **2019**, *15*, 7089–7096.

[4] P. G. de Gennes, *Rev. Mod. Phys.* **1985**, *57*, 827–863.

[5] T. Young, *Philos. Trans. R. Soc. London* **1805**, 65–87.

[6] B. Lavenda, *Sci. Am.* **1985**, *252*, 70–85.

[7] S. Falke, C. Betzel, *Dynamic Light Scattering (DLS)*, Springer International Publishing, **2019**.

[8] C. C. Miller, *Proc. R. Soc. A* **1924**, *106*, 724–749.

[9] S. Pan, Z. W. Wu, W. H. Wang, M. Z. Li, L. Xu, *Sci. Rep.* **2017**, *7*, 39938.

[10] R. Sandhu, N. Singh, J. Dhankhar, K. Gandhi, R. Sharma, in *Nanotechnological Biochem. Tech. Assess. Qual. Saf. Milk Milk Prod.*, **2018**, pp. 135–137.

[11] M. Mazumder, R. Ahmed, M. Hasan, S. J. Lee, M. S. Lee, *Int. J. Civ. Eng.* **2020**, *18*, 251–259.

[12] M. Neshat, N. P. Armitage, *J. Infrared, Millimeter, Terahertz Waves* **2013**, *34*, 682–708.

[13] Y. Kim, C. Park, *Carbon Lett.* **2001**, *2*.

[14] S. L. Erlandsen, C. Frethem, Y. Chen, *J. Histotechnol.* **2000**, *23*, 249–259.

[15] M. Vollmer, K.-P. Möllmann, *Phys. Educ.* **2011**, *46*, 191–202.

[16] A. Iluk, *J. Vibroengineering* **2012**, *14*, 22–26.

[17] J. Ou, Y. Wang, J. Wang, S. Liu, Z. Li, S. Yang, *J. Phys. Chem. C* **2011**, *115*, 10080–10086.

[18] Yang, Z. Wang, Mao, *Nanomaterials* **2020**, *10*, 210.

APPENDIX-B

[19] X. Guo-hua, K. Higashitani, *J. Zhejiang Univ. A* **2000**, *1*, 162–170.

[20] P. Gogoi, S. K. Singh, A. Pandey, A. Chattopadhyay, P. S. Gooh Pattader, *ACS Appl. Bio Mater.* **2021**, *4*, 7921–7931.

[21] X. Chen, B. Zheng, H. Liu, *Anal. Cell. Pathol. (Amst).* **2011**, *34*, 5–18.

[22] A. Diaspro, C. Usai, in *Wiley Encycl. Biomed. Eng.*, **2006**.